Technische Universität München

Lehrstuhl Für Nanoelektronik

Modeling of quantum cascade lasers by ensemble Monte-Carlo methods

Alpár István Mátyás

Vollständiger Abdruck der von der Fakultät für Elektrotechnik und Informationstechnik der Technischen Universität München zur Erlangung des akademischen Grades eines

Doktor-Ingenieurs

genehmigten Dissertation.

Vorsitzende:
Univ.-Prof. Dr.-Ing. Sandra Hirche
Prüfer der Dissertation:
1. Junior-Fellow Dr. Christian Jirauschek
2. Univ.-Prof. Dr.-Ing. Markus-Christian Amann

Die Dissertation wurde am 29.06.2011 bei der Technischen Universität München eingereicht und durch die Fakultät für Elektrotechnik und Informationstechnik am 17.10.2011 angenommen.

Contents

Zusammenfassung (German) 7

Abstract (English) 9

1 Introduction 11

2 Ensemble Monte-Carlo methods for heterostructures 17

- 2.1 Schrödinger solver 19
  - 2.1.1 Matching conditions for the effective mass equation 19
  - 2.1.2 Transfer matrix method 20
  - 2.1.3 Example: quasi bound states for a leaky quantum well 25
- 2.2 Non-parabolicity 27
  - 2.2.1 Non-parabolicity in growth direction 28
  - 2.2.2 In-plane non-parabolicity for non-radiative scattering 28
  - 2.2.3 In-plane non-parabolicity for optical transitions 30
- 2.3 Fermi's golden rule 31
  - 2.3.1 The envelope wavefunction 32
  - 2.3.2 Harmonic perturbation 32
  - 2.3.3 Static perturbation 33
  - 2.3.4 LO polar phonon scattering 34
  - 2.3.5 Impurity scattering 39
  - 2.3.6 Interface roughness scattering 40
  - 2.3.7 Alloy scattering 41
  - 2.3.8 Electron-electron scattering 44
- 2.4 Material gain 48
- 2.5 Monte-Carlo algorithm 51
  - 2.5.1 Choice of the scattering mechanism and final state 55
  - 2.5.2 Choice of the final angle after scattering 56
  - 2.5.3 Pauli's exclusion principle 56

2.6 Electron-electron scattering and space-charge effects in quantum cascade lasers 57
    2.6.1 Quantum cascade lasers 57
    2.6.2 Space charge effects 60
    2.6.3 Exchange effect 61
    2.6.4 Screening 63
2.7 Summary 66

3 Comparison of EMC and NEGF methods for cascade structures 69
3.1 Stark ladders 70
3.2 Quantum cascade laser emitting at 2.75 THz 73
3.3 Quantum cascade laser emitting at 3.4 THz 76
3.4 Summary 79

4 Temperature performance of THz QCLs 81
4.1 Design of THz QCLs 81
4.2 Temperature performance and frequency 83
4.3 Temperature performance and diagonality 84
4.4 Robustness with respect to interface roughness 88
4.5 Summary 88

5 Modeling of mid-infrared quantum cascade lasers 91
5.1 Short injector QCL operating at 8 μm 91
    5.1.1 Effects included in the simulation 92
    5.1.2 Role of the scattering mechanisms 92
    5.1.3 Carrier-light coupling 94
5.2 High wall-plug efficiency QCL operating at 5 μm 95
    5.2.1 Effects included in the simulation 96
    5.2.2 Wall-plug efficiency, output power, IV curves: comparison to experiment 98
    5.2.3 Kinetic carrier distribution 100
5.3 Summary 101

6 Quantum corrections in EMC 103
6.1 Sinusoidal time dependence of the potential 103
6.2 Time-constant potential 107
6.3 Scattering with photons 108
6.4 Broadening for LO-phonons 109
6.5 Effects of quantum corrections on the transport properties of the EMC method 110
6.6 Summary 112

Appendix **113**

Nomenclature **115**

List of Figures **123**

List of Tables **127**

Bibliography **129**

Publications **139**

Acknowledgement **140**

Zusammenfassung (German)

Das Hauptziel dieser Arbeit ist es, die Transporteigenschaften von Terahertz- (THz) und Mitt-Infrarot-Quantenkaskadenlasern (QCLs) theoretisch zu untersuchen, sowie selbstkonsistent neue Effekte für eine präzisere Beschreibung experimenteller QCLs zu modellieren und zu implementieren. Seit den 1980er Jahren werden Ensemble Monte-Carlo (EMC) Methoden zur Simulation verschiedener Halbleiter-Nanostrukturen eingesetzt, von Festkörpern über Potentialtöpfe zu Quantendrähten hin reichend. Insbesondere bei THz-QCLs können die relevanten physikalischen Effekte von quantenmechanischem Tunneln und Kohärenz bis hin zur Streuung aufgrund von Unreinheiten oder Gitterschwingungen reichen. All diese Effekte müssen untersucht und gemäß ihrer Relevanz für eine korrekte Modellierung in EMC berücksichtigt werden. Streuung kann in diesen Bauelementen von verschiedenen Mechanismen stammen, die einen Elektronenfluss von einem Anfangs- in einen Endzustand bewirken. Deswegen diskutieren wir die wichtigsten Streueffekte, angefangen von ihrer physikalischen Beschreibung, d.h. dem Störungs-Hamiltonian, bis hin zur Streurate. Der Monte-Carlo-Algorithmus wird auch kurz beschrieben, sodass die numerische Implementierung neuer Effekte später auf einem soliden Fundament vorgenommen werden kann. Obwohl EMC schon vor Beginn dieser Arbeit für Trägertransport-Simulationen sowohl in Nanostrukturen als auch in QCLs eingesetzt wurde, gibt es immer noch viel in Bezug auf Näherungen und die Miteinbeziehung vollständig quantenmechanischer Effekte zu tun. Unser Ansatz ist dreidimensional, d.h., wir implementieren auch selbstkonsistent den Impuls der Elektronen. Der theoretische Rahmen unserer Monte-Carlo-Methode ist die semiklassische Boltzmanngleichung, die statistisch gelöst wird, wobei die Streuraten in der Boltzmanngleichung durch Fermis goldene Regel einfließen.

Innerhalb dieser Arbeit wurde der EMC-Code um Legierungsstreuung als zusätzlichen Streuprozess erweitert, zudem wurde die energetische Verbreiterung der Quantenzustände implementiert. Weiterhin wurde eine Anpassung an das InGaAs-Materialsystem vorgenommen.

Um unsere Näherungen und unseren Ansatz für THz QCLs zu verifizieren, vergleichen wir zuerst EMC mit einem voll quantenmechanischen Simulationstool, welches unabhängig von Tillman Kubis aus der Gruppe um Professor Vogl entwickelt wurde. Wir sehen, dass EMC die voll quantenmechanischen Resultate im technisch relevanten, also im Lasing-Regime, gut reproduzieren kann. Zusätzlich identifizieren wir Grenzen von EMC, und zwar bei niedrigen Spannungen sowie für Kaskadenstrukturen, welche schwach gebundene Zustände enthalten. THz-QCLs operieren weder bei sehr niedrigen Spannun-

gen, wo die Quantenzustände energetisch angeglichen sind, noch werden schwach gebundene Zustände zum Lasern benötigt. Somit können wir bestätigen, dass EMC eine zuverlässige Methode für ihre Modellierung darstellt, und wir sparen dadurch große Mengen an Simulationszeit für ihre Untersuchung. Dies wird beim systematischen Design und der Simulation von 24 THz QCLs zur Bestimmung ihrer temperaturabhängigen Leistung in der Region von 1-5 THz deutlich. Es stellt sich heraus, dass für QCLs mit vertikalem Übergang die besten Ergebnisse bei ca. 3 THz erzielt werden. Die Gründe dafür sind zum einen die durch die parasitische Injektion limitierte Leistung bei niedrigeren Frequenzen, zum anderen die durch die Phononenemission limitierte Leistung bei hohen Frequenzen. Zusätzlich sehen wir, dass diagonale Lasingübergänge die temperaturabhängige Leistung nur oberhalb von 3.5 THz verbessern. Alle Ergebnisse bezüglich der temperaturabhängigen Leistung von THz QCLs erklären ihr experimentelles Verhalten sehr gut und können einen Einblick gewähren was ihre limitierenden Faktoren sind.

EMC wurde auch für die Simulation von mitt-infraroten QCLs erweitert, mit experimentellem Feedback von Simeon Katz (Gruppe um Prof. Amann). Die Relevanz von Streumechanismen wurde für einen QCL, der bei 8µm emittiert, untersucht. Wir konnten die Wichtigkeit der Streuung an Phononen, Grenzschichtrauheit und Unreinheiten nachweisen, wie in der Literatur erwähnt. Die Grenzschichtrauheit wurde für diese Bauelemente aus Lumineszenzmessungen berechnet, und die extrahierten Parameter wurden dann für die EMC Simulation verwendet. Zudem haben wir die zunehmende Bedeutung des Einflusses von Photonenstreuung für QCLs mit hohem Wirkungsgrad gezeigt. Diese weisen eine erhöhte „Wall-plug“-Effizienz auf, emittieren also in einigen Fällen mehr Licht als Wärme. Wir haben herausgefunden, dass die Emission und Absorption von Photonen nicht nur Sättigung des optischen Gewinns verursacht, sondern auch direkt einen Strom durch Photon-Elektron-Streuprozesse verursacht. Dieser Kanal ist dominant bei hohen „Wall-plug“-Effizienzen, deswegen sollte Elektronen-Photonen-Streuung für das Sättigungsverhalten der Gewinn-Spektren und die Berechnung der Ausgangsleistung, aber auch für die korrekten Strom-Spannungskurven berücksichtigt werden. Wir identifizieren zudem einen hochenergetischen Ausläufer der Verteilungsfunktionen in mitt-infraroten QCLs, der das Resultat nicht-strahlender Übergänge vom oberen zum unteren Laserniveau ist. Dies kann eine Quelle von Leckströmen in höhere Leitungsband-Minima sein. Diese Arbeit möchte die vielseitige Einsetzbarkeit von EMC für die Modellierung und Simulation von QCLs aufzeigen, was durch den Vergleich mit anderen Simulationstools sowie die Modellierung von experimentellen THz- und Mitt-infrarot-Strukturen erreicht wird.

Abstract (English)

The main objective of this thesis is to theoretically investigate the transport properties of terahertz (THz) and mid-infrared quantum cascade lasers (QCLs) as well as to self-consistently model and implement new effects for a more accurate description of experimental QCLs. Since the 1980s, ensemble Monte-Carlo (EMC) methods have been used for the simulation of various semiconductor nanostructures, ranging from bulk materials to quantum wells and wires. Especially for THz QCLs the relevant effects can range from quantum mechanical tunneling and coherence to scattering due to device imperfections or lattice vibrations. All of these effects need to be investigated and included based on their relevance in EMC for the correct modeling of the structures. Scattering in these devices can happen due to different mechanisms which produce an electron flow from an initial state to a final state. Therefore we review the most relevant scattering types starting from their physical description, i.e., perturbation Hamiltonian, and arrive at the actual rate. The Monte-Carlo algorithm is also briefly discussed so that the numerical implementation of new effects can be later faithfully implemented. Although EMC has been used for carrier transport simulations in nanodevices as well as QCLs before the beginning of this work, there is still much to be done in terms of approximations and inclusion of fully-quantum mechanical effects. Our approach is three dimensional, i.e., we also self-consistently implement the momentum of the electrons. The theoretical framework of our Monte-Carlo method is the semiclassical Boltzmann equation, which is statistically solved and the scattering rates enter the Boltzmann equation by Fermi's golden rule.

Within this work, the EMC approach has been extended by including alloy scattering among the scattering processes, additionally energetic broadening of the quantum states has been implemented. Furthermore, an adaptation to the InGaAs material system has been performed.

For the validation of our approximations and approach on THz QCLs, we first compare EMC to a fully quantum mechanical simulation tool developed independently by Tillmann Kubis from the Vogl group. We find that EMC can well reproduce fully quantum mechanical results in the technically relevant, i.e., lasing regime. Furthermore we identify limits of EMC, namely in the low bias range of the devices as well as for cascade structures that contain weakly bound states. THz QCLs are neither operating at very low biases where the states are aligned, nor use weakly bound states for lasing. Thus we can affirm that EMC is a valuable method for their modeling and we thereby save large amounts of simulation time for their investigation. This will be shown since we systematically design and simulate 24 THz QCLs for the investigation of their temperature performance in the 1-5 THz range. It turns out that for vertical transition QCLs the best performing devices are around 3 THz. This is due to parasitic injection limited performance on the lower frequency side as well as phonon emission limited performance on the high frequency side. Furthermore we find that diagonal lasing transitions help the temperature performance of QCLs only above about 3.5 THz. All the temperature results on THz QCLs explain their experimental behavior very well and can give an insight into their limiting factors.

EMC was also extended for the simulation of mid-infrared QCLs, with the experimental feedback of Simeon Katz from the Amann group. The relevance of scattering mechanisms was investigated for a QCL emitting at $8\,\mu m$. We have confirmed the importance of phonon, interface roughness and impurity scattering as widely recognized by literature. The interface roughness was calculated for these devices from luminescence measurements and we used the roughness parameters in EMC correspondingly. Furthermore, we have shown the increasing importance of the influence of photon scattering processes for high-efficiency QCLs. They have increased wall-plug efficiencies, i.e. emitting more light than heat in some cases. We have found that stimulated emission and absorption of photons does not only induce gain saturation in these devices, but also directly induces a current due to the photon-electron scattering process. This current channel is dominant at high wall-plug efficiencies, thus electron-photon scattering should be included for the saturation of the gain spectra, calculation of output power, however also for the correct current-voltage curves. We also identify a high energy tail of the distribution function in mid-infrared QCLs which is the result of non radiative transitions from the upper to the lower laser level. This can be a source of leakage channels into higher valleys. The results of this thesis aim to show the versatile nature of EMC for QCL modeling and simulation, by comparison to other simulation tools as well as the simulation of various experimental structures.

Chapter 1

Introduction

Lasers in everyday life are established optoelectronic devices. Applications include communication devices, optical recording, laser printing and supermarket scanners as well as fundamental science, spectroscopy and medicine. III-V semiconductor lasers, lead-salt laser diodes (PbS, PbTe, PbSe), vertical cavity surface emitting lasers (VCSELs), difference-frequency generation of coherent light with a nonlinear crystal (GaAs, GaSe, GaP, ZnTe, CdTe), free electron lasers and quantum cascade lasers (QCLs) are only some of the many approaches possible to produce coherent light.

Up to the invention of the quantum cascade laser in Bell Labs [1], semiconductor lasers in the mid-infrared were mainly built from diodes that emit light by the recombination of an electron-hole pair in a quantum well. For the design of such devices, band gap engineering is used with compound semiconductors, to assess different wavelengths. In spite of these techniques, the efficiency of the mid-infrared devices is still limited due to material and growth constraints. For the generation of mid-infrared light, the bandgap of the materials simply becomes highly temperature dependent and defects (such as traps in the bandgap) and processing also provide difficulties.

Quantum cascade lasers (QCLs) offer an advantage in the variety of wavelengths that can be designed by using the same material system. A quantum cascade laser is a periodic superlattice, where in each period ideally one photon is emitted by a lasing transition between quantized states in the conduction band, and the electron is injected into the next period. They are unipolar devices, i.e., they use only the conduction band for the generation of light through a cascaded approach. Instead of band-gap engineering, the design of conduction band states is performed by choice of the device layer thicknesses. This approach circumvents the so called “bandgap-slavery” [2] and offers the advantage of designing efficient coherent emitters from 4 to 12 μm in the mid-infrared (MIR) and from 60 to 200 μm in the far-infrared or terahertz regime. Since their first demonstration in 1994 [1], MIR QCLs have shown rapid development. The first room-temperature QCL was demonstrated in 1996 [3], the first continuous wave operation at room-temperature was reported in 2002 [4], the continuous wave output power exceeded 1.6 W in 2008 [5], and in 2010, QCLs emitting more light than heat were demonstrated [6, 7]. Today’s mid-infrared QCLs are efficient devices and suitable for a wide variety of applications, ranging from spectroscopy to free-space communications and the detection of small molecule gases (CO, CO_2, CH_4). Mid-infrared QCLs already operate at room temperature. The first THz QCL was demonstrated in 2002 [8], however, QCLs in the THz regime ($60\,\mu m$-$200\,\mu m$) are still limited to cryogenic temperatures. These structures can offer 100 miliwatt-level output powers at cryogenic temperatures. In the THz region the only practical coherent sources are THz QCLs and lasers that use frequency difference generation as well as free-electron lasers [9]. No major alternative for lasing is offered making the effort of THz QCL design and investigation worthwile. The thesis presents modeling of THz and MIR QCLs with the ensemble Monte-Carlo method, focusing on the theory needed for investigating and clarifying the microscopic processes, and presenting an analysis of various experimental designs.

For the theoretical modeling and analysis of quantum cascade lasers, various tools with different degrees of complexity have been developed, all of them having advantages and drawbacks. We mention these below and the interested reader can refer to our bibliography for further details and a deeper understanding of the methods. One of the simplest approaches for laser analysis are rate-equation based models [10]. They are a semiclassical approach and do not take into account the in-plane kinetic energy of carriers, i.e., they are one-dimensional models. The advantage of a rate-equation QCL solver lies in its numerical simplicity, since it can offer results within a few minutes, making it suitable for systematic QCL design and qualitative analysis. A rate-equation based model is also very useful for QCLs that have many energetic states in a miniband like, such as bound to continuum (BTC) QCLs. An ensemble Monte-Carlo (EMC) approach would need large simulation times for these devices, while a rate-equation based calculation can give fast results. EMC methods, for QCLs with a moderate number of states, have their advantage in keeping the numerical effort manageable and allowing for the exact and self-consistent inclusion of semiclassical scattering mechanisms. For example carrier-carrier interactions [11, 12, 13] can be included as a two-body process while a full kinetic energy distribution of the electrons is considered. The typical run-time for such a simulation is about one hour on an Intel Xeon E5420 server core, however it can go up to 1-2 days for structures that have many energetic states. Theoretical limitations of EMC are the neglected quantum mechanical effects like quantum correlation of electrons [14, 15] and the approximation of an infinitely small linewidth of the electronic states (by Fermi's golden rule), as well as scattering through intermediate states, i.e., non-diagonal scattering. The most general description of electron transport is a fully quantum mechanical simulation tool, based on the non-equilibrium Green's functions (NEGF) method, which includes all the effects lacking in EMC. The drawback of NEGF lies in its elevated numerical complexity and the neglect of carrier-carrier interactions as a two body process, which cannot be included due to its numerical complexity. For THz QCLs two main NEGF approaches were developed over the years. The first approach neglects the in-plane kinetic energy dependence of carriers and assumes a typical kinetic energy [16, 17, 18] and periodic boundary conditions. The second NEGF approach uses a full spatial implementation of the QCL structure and energetic states, however it can only simulate limited QCL period amounts (typically 1-2) due to its numerical complexity. This approach can use only a) quasi-periodic boundary conditions by assuming unbiased QCL periods as leads [19, 20], or b) open boundary conditions. We have also performed simulations with the second NEGF approach, and the typical run-time until convergence ranges from 1-2 days to several weeks on the LRZ Linux cluster even for relatively simple QCL structures. Furthermore, density matrix methods have been developed [21], which use a kinetic energy balance model to find a typical kinetic energy, for being able to neglect the in-plane distribution. Having said the above, one can conceive, that there is no perfect tool or approach for the simulation of QCLs. All methods have advantages and drawbacks and one has to find a compromise between accuracy and numerics, which together with the uncertainty in material and growth parameters makes the modeling of QCLs a challenging task.

The scopes of this thesis are

1. implementing different mechanisms for the electronic transport and closely comparing to experiment and to other theoretical methods like-NEGF [14],

2. comparative analysis of THz QCLs to asses the optimum parameters for temperature performance and understand the limitations [22],

3. adapting our method for the InGaAs material system and for mid-infrared QCLs by deriving the alloy scattering rate, non-parabolicity and using the recently included carrier-photon interaction in EMC [23].

The main results in this thesis are mentioned below.

- The theory needed for the semiclassical EMC simulation of quantum cascade lasers is reviewed and derivations are shown for the scattering rates, non-parabolicity and material gain.

- Based on comparisons between EMC and NEGF methods for THz QCLs and Stark ladders, we find good agreement of the two theories in the technically relevant regimes. This validates our semiclassical EMC approach for THz cascade devices. For the very low bias region and for the case of tunneling through continuum states, EMC can underestimate currents since coherent tunneling and level-broadening are neglected. However, these effects are not relevant in the lasing regime of QCLs.

- The relation between frequency and maximum operating temperature of vertical lasing-transition THz QCLs is demonstrated. We identify parasitic injection into the lower laser level and thermally excited scattering from the upper to the lower laser level as the main effects limiting the temperature performance of the devices. Furthermore, we analyze why structures that lase at about 3 THz are the best-performing ones.

- We investigate and understand the role of diagonal lasing transitions for state-of the art THz QCLs in the context of temperature performance. It is found that above about 3.5 THz diagonal transitions lead to an improvement, while below vertical transitions are the optimum for higher operating temperatures.

- The influence of different scattering mechanisms on the transport and optical properties of mid-infrared InGaAs-based QCLs is investigated. It is found that the dominant scattering mechanism is electron LO-phonon scattering in these devices. Furthermore, interface roughness and alloy scattering can moderately influence device currents, so they should be included in the transport calculations for these devices.
- We discuss the influence of the electron-photon interaction on the current and output power of highly efficient QCLs. The stimulated photon processes are found to contribute significantly to the device currents, showing that electron-photon scattering interactions are non-negligible in high wall-plug efficiency structures. Furthermore, a high-energy tail of the distribution function is identified at about the lasing transition energy, which can be a source of leakage to other valleys.
- Quantum corrections in the Monte-Carlo method are derived by including the broadening of the quantized states. We replace Fermi's golden rule by a generalization derived from the density matrix formalism and a possible implementation into EMC is discussed. We find a good modeling of currents in the coherent regime, i.e., at low biases. The numerical complexity of our EMC approach remains the same, even though this quantum correction is now included.

The thesis is organized as follows:

In Chapter 2, we present the basic theoretical framework for the semiclassical EMC method. The Boltzmann equation is presented, the Schrödinger-Poisson solver is discussed, the non-parabolicity is considered for our QCL systems, for both the growth and in-plane directions. Fermi's golden rule is derived and understood by the use of perturbation theory. All the scattering mechanisms like scattering with phonons, electrons, impurities, roughness and alloy disorder are derived from scratch as well as the spectral gain. Furthermore, the relevant steps in the Monte-Carlo algorithm are briefly discussed.

In Chapter 3 we compare EMC as a semiclassical and NEGF as a fully quantum mechanical approach for the calculation of device currents of Stark ladders and QCLs with THz transitions. First, we present our comparative analysis on Stark ladders as the most elementary cascade devices. Then we also compare the two methods for experimental QCL designs with different doping and frequency, and we show results for the spectral gain.

After we have justified the use of the EMC method for the simulation of THz QCLs by comparing to NEGF, we investigate the temperature performance of state of the art THz QCLs in Chapter 4. We start by presenting a new set of QCL designs, which has been done in collaboration with Mikhail Belkin's group. Next we unfold the effects that favor QCL temperature performance at around 3 THz for vertical lasing transitions. We also discuss the effects of lasing transition diagonality on the temperature performance and validate our results against interface roughness, which is a vaguely known parameter.

Chapter 5 is concerned with the simulation of InGaAs-based mid-infrared QCLs. We discuss the relevance of the various scattering mechanisms. Furthermore, we present the robustness of our EMC tool in reproducing the experimental measurements for various QCLs, and show the importance of stimulated photon processes for the electron transport. The high kinetic energy tail of the electron distribution function in these structures is discussed.

In the last chapter we derive an alternative to Fermi's golden rule for taking into account the lifetime broadening of the quantum states. We show its implementation for LO-phonons and photon scattering. The complete implementation in the EMC code, shows a correct modeling of the current in the coherent regime, i.e., low biases. The current in the incoherent regime remains is proven to be semiclassical.

Chapter 2

Ensemble Monte-Carlo methods for heterostructures

Self-consistent Monte-Carlo transport simulations are well established tools for the modeling and optimization of QCL devices [11]-[14],[24]-[32]. They are based on the solution of the semi-classical Boltzmann equation which is defined in its general form as

$$\frac{\mathrm{d}f(\mathbf{R},\mathbf{K},t)}{\mathrm{d}t} = \frac{\partial f(\mathbf{R},\mathbf{K},t)}{\partial t} + \dot{\mathbf{R}}\nabla_{\mathbf{R}} f(\mathbf{R},\mathbf{K},t) + \dot{\mathbf{K}}\nabla_{\mathbf{K}} f(\mathbf{R},\mathbf{K},t). \tag{2.0.1}$$

In the ensemble Monte-Carlo method, the above equation is solved for the distribution function by means of a statistical average over many electrons. Here t is the time variable, $\mathbf{R}$ is the position and $\mathbf{K}$ is the wavevector of the electron. An overdot denotes a derivative with respect to t. EMC provides a straightforward extraction of various physical observables, by solving the above equation. For example distribution functions, current, parasitic current channels, injection efficiencies, gain spectra, electron temperatures and output power [33] can be calculated by solving the above equation.

In Eq. (2.0.1), the last two terms represent the change of f with respect to position and wavevector. The derivative with respect to the spatial coordinate $\mathbf{R}$ can be neglected, since we consider a separable electron probability. This is defined by having wavefunctions in the z (or confined)-direction and distribution functions in the planar direction. In this way every electronic state m has a wavefunction ψ_m and a distribution function f_m, and f_m depends only on t and $\mathbf{K}$. The change of f with respect to the wavevector $\mathbf{K}$ is not 0; however, since we have a constant electric field in the confinement direction (z) and no electric and magnetic fields $\mathbf{E}$ and $\mathbf{B}$ in other directions, we use the equation

$$\hbar\dot{\mathbf{k}} = -e_0[\mathbf{E} + \mathbf{v}_e \times \mathbf{B}] \tag{2.0.2}$$

to find $\dot{\mathbf{k}} = 0$. Here, $\mathbf{v}_e$ is the electron velocity and e_0 the electron charge. Since the wavefunctions do not change in time, $\dot{k}_z = 0$ and the term proportional to $\dot{\mathbf{K}} = \begin{bmatrix} \dot{\mathbf{k}} & \dot{k}_z \end{bmatrix}$ in Eq. (2.0.1) can be neglected. If the above approximations are applied, we arrive at the equation [30]

$$\frac{\mathrm{d}f_{n\mathbf{k}}}{\mathrm{d}t} = \sum_{m\mathbf{k}'}\sum_{s} \left[W^{s}_{m\mathbf{k}'n\mathbf{k}} f_{m\mathbf{k}'} - W^{s}_{n\mathbf{k}m\mathbf{k}'} f_{n\mathbf{k}}\right]. \tag{2.0.3}$$

Here, $W^{s}_{n\mathbf{k}m\mathbf{k}'}$ is the scattering rate between the initial state n with wavevector $\mathbf{k}$ and final state m with wavevecor $\mathbf{k}'$, while the index s represents the scattering type. The scattering rates are calculated by Fermi's golden rule and enter the above equation. For solving the above equation, many steps are performed. First of all, a basis is defined using the wavefunctions calculated by the Schrödinger solver, second all the scattering rates are calculated in this basis, furthermore an algorithm is used for the solution of Eq. (2.0.3). The theory for performing these steps is found in this chapter and we now summarize its main sections.

First we discuss the calculation of the basis of electronic states. This is performed by solving the coupled Schrödinger and Poisson equations over five biased QCL periods, using periodic boundary conditions. The Poisson equation can be straightforwardly solved after finding the charge distribution from the wavefunctions and assuming charge neutrality with periodic boundary conditions. The implementation of the Schrödinger solver by means of transfer matrices and the shooting method will be discussed in detail.

For specific QCLs, the parabolic dispersion relation between kinetic energy and in-plane momentum offers a crude approximation only, since the dispersion of the high-energy electrons is non-parabolic. For a more accurate relation, we consider the non-parabolic case by taking the energy dependent effective mass approach. This will be presented in Section 2.2 for both the confined and in-plane direction.

Fermi's golden rule, which is the basic expression relating the scattering rate, perturbation potential and electron states is discussed in Section 2.3. The scattering mechanisms considered here are electron-phonon, electron-electron, electron-interface roughness, electron-impurity, electron-alloy disorder and electron-photon scattering. Examples will be given for their derivation, with the exception of photon scattering, which will be discussed in Section 6.3.

The optical properties of QCLs are quantified by the material gain which is derived in Section 2.4, based on a Lorentzian level-broadening [12].

In Section 2.5, we discuss the main steps of the Monte-Carlo algorithm, the random choice of scattering, initial and final states as well as the Pauli exclusion principle.

Since the implementation and improvement of today's EMC code was performed over several years, our results contain different effects and approximations. These are summarized in the last section in a table, which lists the approximations and effects used for the results in the different chapters of this thesis.

2.1 Schrödinger solver

All our theoretical investigations are based on the electronic wavefunctions in the calculated heterostructure. For calculating the wavefunctions, we need to solve the Schrödinger and Poisson (SP) equations iteratively. The Poisson equation accounts for space charge effects and just leads to a modified potential profile of QCLs, since they are doped structures. Basically the doping and the electrons in the structure produce a potential $V_p(z)$, which needs to be added to the conduction band profile to account for the band bending. The Poisson equation is defined as [27]

$$-\frac{\partial}{\partial z}\frac{\varepsilon(z)\partial V_P(z)}{\partial z} = e_0 \left[N(z) - \sum_n n_{2D,n}\psi_n(z)^2 \right],$$

where $\varepsilon(z)$ is the dielectric constant in the active region, e_0 is the electron charge, $N(z)$ is the donor concentration in the structure, $n_{2D,n}$ is the sheet doping density and ψ_n is the wavefunction of the nth state. The Poisson equation is solved on the same discretized grid where the wavefunctions are defined and models the space-charge effects in our QCLs.

The iteration of the SP solver starts with the solution of the Schrödinger equation, then an occupation is assumed by either solving the Boltzmann equation or by assuming a thermal electron distribution. The former is the exact approach, however the latter is the numerically efficient approach, typically used for the design of experimental structures. After the level occupations are known, we calculate the charge distributions and solve the Poisson equation to get the new potential. In the following we restrict ourselves to the discussion of the Schrödinger solver.

2.1.1 Matching conditions for the effective mass equation

In a biased periodic multi-quantum well structure, the Schrödinger equation needs to be solved. The obtained eigenstates form the basis for the carrier transport calculations with EMC. In our program the transfer matrix method is used, which is applied to a discretized potential profile grid. Step potentials approximate the biased conduction band profile as shown in Fig. 2.1.1. This is practical to use, since the band bending can be well approximated. Also the interface of a barrier/well does not require additional points, and a uniform grid can be implemented.

The solution of the Schrödinger equation is known for the constant potential-region between two grid points. However, we need to match all the solutions between the steps that approximate the potential profile. This is done by first extending the Schrödinger equation to the effective mass equation

$$-\frac{\hbar^2}{2}\frac{\partial}{\partial z}\frac{1}{m_z^*(z)}\frac{\partial}{\partial z}\psi(z) + V(z)\psi(z) = E_z\psi(z) \tag{2.1.1}$$

to account for the change of the effective mass m_z^* and keep the Hamilton operator Hermitian. In the case of a heterojunction from two kinds of materials, the effective mass has only two values corresponding to

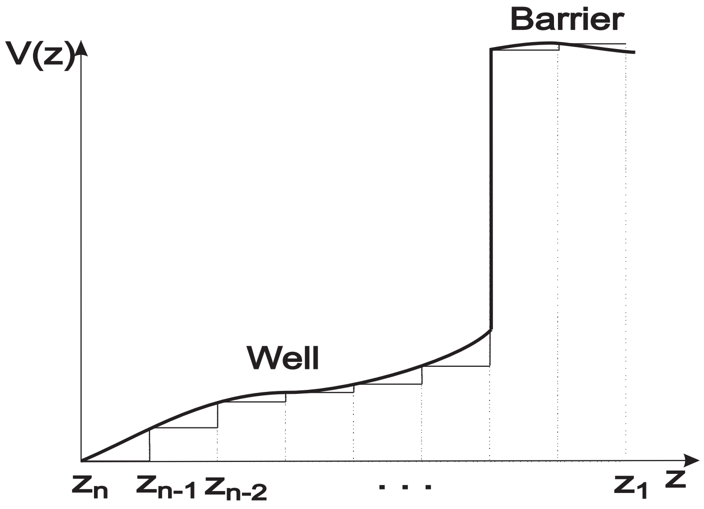

Figure 2.1.1: Approximation of potential profile by step-functions.

the well and barrier materials. The wavefunction of the electron must be continuous through the material interfaces at z_j, $\psi^-(z_j) = \psi^+(z_j) = \psi(z_j)$. The matching condition for the derivative of the wavefunction is calculated by integrating Eq. (2.1.1) over the infinitely small interval $[z_j - \iota, z_j + \iota]$ as

$$-\frac{\hbar^2}{2}\left(\frac{1}{m_z^*(z)}\frac{\partial}{\partial z}\psi(z)\right)\Big|_{z_j-\iota}^{z_j+\iota} = \int\limits_{z_j-\iota}^{z_j+\iota}(E - V(z))\psi(z)\mathrm{d}z = 0. \tag{2.1.2}$$

The rhs. term of Eq. (2.1.2) is 0 in the limit of $\iota \to 0$, because the potential and the wave function are all finite variables, thus an integration over an infinitely small interval gives 0. Taking the same limit for the lhs. of Eq. (2.1.2), we get the matching conditions

$$\begin{aligned} \psi^-(z_j) &= \psi^+(z_j), \\ \frac{1}{m_-^*(z_j)}\partial_z\psi^-(z_j) &= \frac{1}{m_+^*(z_j)}\partial_z\psi^+(z_j). \end{aligned} \tag{2.1.3}$$

The values of $m_-^*(z_j)$ and $m_+^*(z_j)$ are the effective mass of the electron in the left and right step-function. The above conditions can be used for matching two step-potentials in a single material as well as across a barrier/well interface.

2.1.2 Transfer matrix method

The transfer matrix method (TMM) uses the effective mass equation (2.1.1) to find the wavefunctions and energy levels for an arbitrary potential profile. One of the advantages of the TMM lies in the precise consideration of the boundary between well and barrier. In Fig. 2.1.1 we see the approximation of a potential-profile by step functions. The solution of the effective mass equation (2.1.1) for the flat part of

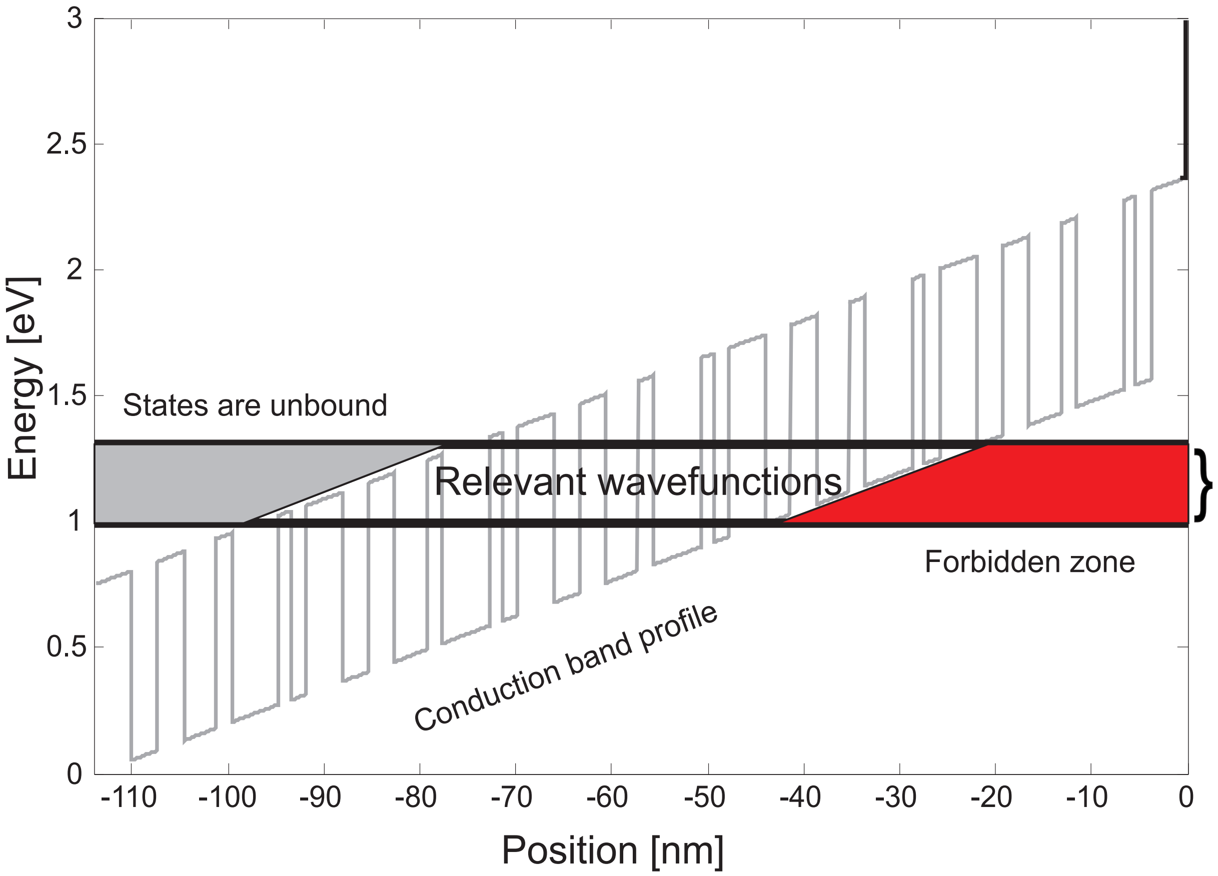

Figure 2.1.2: Conduction band profile, classification of states

the jth step function can be written as

$$\psi(z) = \tilde{C}_{j-1} e^{-ik_{z_{j-1}}(z-z_{j-1})} + \tilde{D}_{j-1} e^{ik_{z_{j-1}}(z-z_{j-1})},\ z_{j-1} < z < z_j, \tag{2.1.4}$$

where we set $V(z) = V_{j-1}$ and $m_z^*(z) = m_{z_{j-1}}^*$ in Eq. (2.1.1), and $k_{z_{j-1}}$ is given by the parabolic dispersion relation

$$k_{z_{j-1}} = \frac{\sqrt{2m_{z_{j-1}}^*(E_z - V_{j-1})}}{\hbar}. \tag{2.1.5}$$

In our Schrödinger solver, the transfer matrix method is applied over five stacks of QCL periods biased with a predefined electric field as shown in Fig. 2.1.2. At the right boundary, the wavefunctions are considered to be 0, since an infinitely large potential is assumed. In the forbidden zone the wavefunctions should be 0 since they are below the conduction band. An energy interval defined equal to the voltage drop of one QCL period is sketched by the curly bracket. In this region the TMM is applied, with the so-called shooting method. The solver scans through the energy interval and calculates the transfer matrix at each energy point. At the left boundary of the simulated QCL periods, we look for the minima of the wavefunction coefficients $\left|\tilde{C}_N\right|$ and $\left|\tilde{D}_N\right|$ with the interval-division method, since states should decay in the unbound region. The solutions of the effective mass equation (2.1.1) will be the states with the highest lifetime, i.e. the most bound states. These states are marked by the "Relevant wavefunctions" area in Fig. 2.1.2 and are the so-called quasi-bound states. In the gray-shaded area above the conduction band profile the wavefunctions are highly unbound. The highly unbound, or continuum states lack a correct inclusion in EMC, as will be discussed in Section 3.1, however they seem not relevant for the carrier transport in QCLs.

The lifetime of the energy levels that are calculated by the shooting method and the above boundary conditions is now mathematically discussed. For the intervals where $k_{z_{j-1}}$ in Eq. (2.1.5) becomes imaginary, we define $k_{z_{j-1}} = i\kappa_{z_{j-1}}$ and write Eq. (2.1.4) in terms of exponentials

$$\psi(z) = C_{k-1} e^{\kappa_{z_{j-1}}(z-z_{j-1})} + D_{j-1} e^{-\kappa_{z_{j-1}}(z-z_{j-1})},\ z_{j-1} < z < z_j. \tag{2.1.6}$$

For real k_z, the wavefunctions above the conduction band or in the wells are written in terms of sine/cosine functions

$$\psi(z) = C_{j-1} \cos\left[k_{z_{j-1}}(z - z_{j-1})\right] - D_{j-1} \sin\left[k_{z_{j-1}}(z - z_{j-1})\right],\ z_{j-1} < z < z_j, \tag{2.1.7}$$

by redefining the constants C_{j-1} and D_{j-1}. Both Eqs. (2.1.6) and (2.1.7) contain only real variables, thus they can be straightforwardly implemented in our numerical solver. We have four transfer matrices for calculating the wavefunctions. These mainly depend on the two grid-points, i.e., whether the energy E_z is above or underneath the conduction band profile. The four cases are:

1. Both grid points $(j-1)$ and j give an imaginary wavevector according to Eq. (2.1.5). In this case the wavefunctions are matched based on Eq. (2.1.3), by using Eq. (2.1.6). The transfer matrix can be written as

$$\begin{bmatrix} C_j \\ D_j \end{bmatrix} = \frac{1}{2} \begin{bmatrix} 1 & 1 \\ 1 & -1 \end{bmatrix} \begin{bmatrix} e^{\kappa_{z_{j-1}}\Delta_z} & e^{-\kappa_{z_{j-1}}\Delta_z} \\ \frac{\kappa_{z_{j-1}} m^*_{z_j}}{k_{z_j} m^*_{z_{j-1}}} e^{\kappa_{z_{j-1}}\Delta_z} & -\frac{\kappa_{z_{j-1}} m^*_{z_j}}{k_{z_j} m^*_{z_{j-1}}} e^{-\kappa_{z_{j-1}}\Delta_z} \end{bmatrix} \begin{bmatrix} C_{j-1} \\ D_{j-1} \end{bmatrix}. \tag{2.1.8}$$

2. The wavevector is imaginary at $(j-1)$ and real at j, which corresponds to exponential and sinusoidal wavefunctions at $(j-1)$ and j respectively. In this case the transfer matrix

$$\begin{bmatrix} C_j \\ D_j \end{bmatrix} = \begin{bmatrix} e^{\kappa_{z_{j-1}}\Delta_z} & e^{-\kappa_{z_{j-1}}\Delta_z} \\ \frac{\kappa_{z_{j-1}} m^*_{z_j}}{k_{z_j} m^*_{z_{j-1}}} e^{k_{z_{j-1}}\Delta_z} & -\frac{\kappa_{z_{j-1}} m^*_{z_j}}{k_{z_j} m^*_{z_{j-1}}} e^{-\kappa_{z_{j-1}}\Delta_z} \end{bmatrix} \begin{bmatrix} C_{j-1} \\ D_{j-1} \end{bmatrix}, \tag{2.1.9}$$

is found by matching Eq. (2.1.7) with Eq. (2.1.6) at the jth grid point

3. The wavevector is real for the $(j-1)$th and imaginary for the jth grid point. In this case the

transfer matrix is calculated as

$$\begin{bmatrix} C_j \\ D_j \end{bmatrix} = \frac{1}{2} \begin{bmatrix} 1 & 1 \\ 1 & -1 \end{bmatrix} \begin{bmatrix} \cos\left(k_{z_{j-1}}\Delta_z\right) & -\sin\left(k_{z_{j-1}}\Delta_z\right) \\ \frac{k_{z_{j-1}} m^*_{z_j}}{\kappa_{z_j} m^*_{z_{j-1}}} \sin\left(k_{z_{j-1}}\Delta_z\right) & \frac{k_{z_{j-1}} m^*_{z_j}}{\kappa_{z_j} m^*_{z_{j-1}}} \cos\left(k_{z_{j-1}}\Delta_z\right) \end{bmatrix} \begin{bmatrix} C_{j-1} \\ D_{j-1} \end{bmatrix}. \tag{2.1.10}$$

4. The wavenumber is real for the $(j-1)$th and jth grid points. The transfer matrix in this case is

$$\begin{bmatrix} C_j \\ D_j \end{bmatrix} = \begin{bmatrix} \cos\left(k_{z_{j-1}}\Delta_z\right) & -\sin\left(k_{z_{j-1}}\Delta_z\right) \\ \frac{k_{z_{j-1}} m^*_{z_j}}{k_{z_j} m^*_{z_{j-1}}} \sin\left(k_{z_{j-1}}\Delta_z\right) & \frac{k_{z_{j-1}} m^*_{z_j}}{k_{z_j} m^*_{z_{j-1}}} \cos\left(k_{z_{j-1}}\Delta_z\right) \end{bmatrix} \begin{bmatrix} C_{j-1} \\ D_{j-1} \end{bmatrix}. \tag{2.1.11}$$

Here $k_{z_{j-1}}$, $m^*_{z_{j-1}}$ and k_{z_j}, $m^*_{z_j}$ are the wavevector and effective mass at the points z_{j-1} and z_j and $\Delta_z = z_j - z_{j-1}$ is the discretization step of the grid points. For the complete wavefunction at the given energy E_z, the C_j and D_j coefficients must be stored. The above four cases cover all the type of matching conditions: decaying wavefunction at energies below the conduction band, wavefunction that enters the barrier from the well, wavefunction that exits the barrier and enters the well, wavefunction that is in the well and behaves sinusoidal. The boundary conditions are defined on an integer grid $\{1, N\}$, where each point represents 1 Å. At the right boundary, as shown in Fig. 2.1.2, we have a very large confinement potential, thus the initial condition for the right propagating wave is $C_1 = 0$ and for the left propagating wave $D_1 = 1$. We note that the individual wavefunctions are normalized at the end. Based on the transfer matrices from Eqs. (2.1.8), (2.1.9), (2.1.10) and (2.1.11) the wavefunction can be found for a given energy E_z. However, only a finite set of states can be considered for calculations, due to numerical reasons. Thus we need to find the set of wavefunctions that contributes most to the transport of electrons. This is done based on the lifetime of the states. After predefining a number of states n_s, the first n_s states with the highest lifetime are considered, in the energy interval marked in Fig. 2.1.2 by the curly bracket.

The lifetimes based on the transfer matrix theory are now derived, starting from the time-dependent Schrödinger equation

$$i\hbar\partial_t\psi = (E^r_m - 0.5i\Gamma^{sp}_m)\psi \approx (E^r_m - 0.5i\Gamma^{sp}_m)(E_z - E^r_m + 0.5i\Gamma^{sp}_m)\partial_{E_Z}\psi(E^r_m). \tag{2.1.12}$$

Here, the solution of the time-independent Schrödinger equation is assumed to be $H\psi = E^{ti}_m\psi = (E^r_m - 0.5i\Gamma^{sp}_m)\psi$, and it is substituted into the time-dependent Schrödinger equation. The values E^r_m and Γ^{sp}_m are the real and imaginary parts of the eigenenergy E_z, which is allowed to be complex for the general case of quasi-bound states. We want to minimize the change of ψ with respect to time, so that stationary wavefunctions can be used. This is performed by minimizing the Taylor expansion around the real-solution E^r_m of the above equation, i.e., find $E_z = E^r_m$. The full solution for the state m contains the imaginary coefficient Γ^{sp}_m, which corresponds to the lifetime of the state m before it escapes from the quantum wells. Here ψ is defined by Eq. (2.1.4) for $z = z_{j-1} = z_N$. A minimization function h can be defined from the rhs. of Eq. (2.1.12) as

$$h(E_z) = |\partial_{E_z}\psi(E^r_m)|^2 \left[(E_z - E^r_m)^2 + 0.25\,(\Gamma^{sp}_m)^2\right] \tag{2.1.13}$$

and the minimization problem

$$E^r_m \in \min_{E_z}\,[h(E_z)] \tag{2.1.14}$$

must be solved. The wavefunctions with the highest lifetimes (lowest Γ^{sp}_m) fulfill the condition $\partial_t\psi \approx 0$ best if we minimize h. Substituting Eq. (2.1.4) for ψ in Eq. (2.1.13) and assuming that the wave only propagates from the right to the left, the term proportional to $\tilde{C}_N$ can be dropped and

$$h(E_z) = \left|\partial_{E_z}\tilde{D}_N(E_z)\right|^2 \left[(E_z - E^r_m)^2 + 0.25\,(\Gamma^{sp}_m)^2\right]. \tag{2.1.15}$$

The boundary conditions assume sinusoidal functions at the lhs. of the device thus we can use the transformation

$$\tilde{D}_N = \frac{C_N + iD_N}{2} \tag{2.1.16}$$

to find

$$C_N(E_z)^2 + D_N(E_z)^2 \sim h(E_z) = \left\{[\partial_{E_z}C_N(E^r_m)]^2 + [\partial_{E_z}D_N(E^r_m)]^2\right\}\left[(E_z - E^r_m)^2 + 0.25\,(\Gamma^{sp}_m)^2\right]. \tag{2.1.17}$$

The above equation proves that the wavefunction coefficients behave as a second-order function with a minimum around $0.25\,(\Gamma^{sp}_m)^2$. Thus the numerical calculation of the minimization problem, i.e., Eq. (2.1.14), is performed directly by minimizing the coefficients $C_N(E_z)^2 + D_N(E_z)^2$. For this case, the energetic solutions for the local minima give the energy of the states approximately. To find the lifetime of the electron corresponding to the state E^r_m before leaking out, we calculate the tunneling rate

$$\frac{\Gamma^{sp}_m}{\hbar} = \sqrt{\frac{8h(E^r_m)}{\partial^2_{E_z}h(E^r_m)}}. \tag{2.1.18}$$

To summarize, the Schrödinger solver performs the following steps for the shooting method:

1. Scans through the energy interval given by the bias drop over one QCL period.

2. Calculates for every energy E_z the wavefunction, using the transfer matrix Eqs. (2.1.8), (2.1.9), (2.1.10) and (2.1.11).

3. Uses the minimization condition of Eq. (2.1.14) and directly minimizes the coefficients $C_N(E_z)^2 + D_N(E_z)^2$ to find the wavefunctions.

4. Sorts the wavefunctions after relevance, using the highest lifetimes based on Eq. (2.1.18).

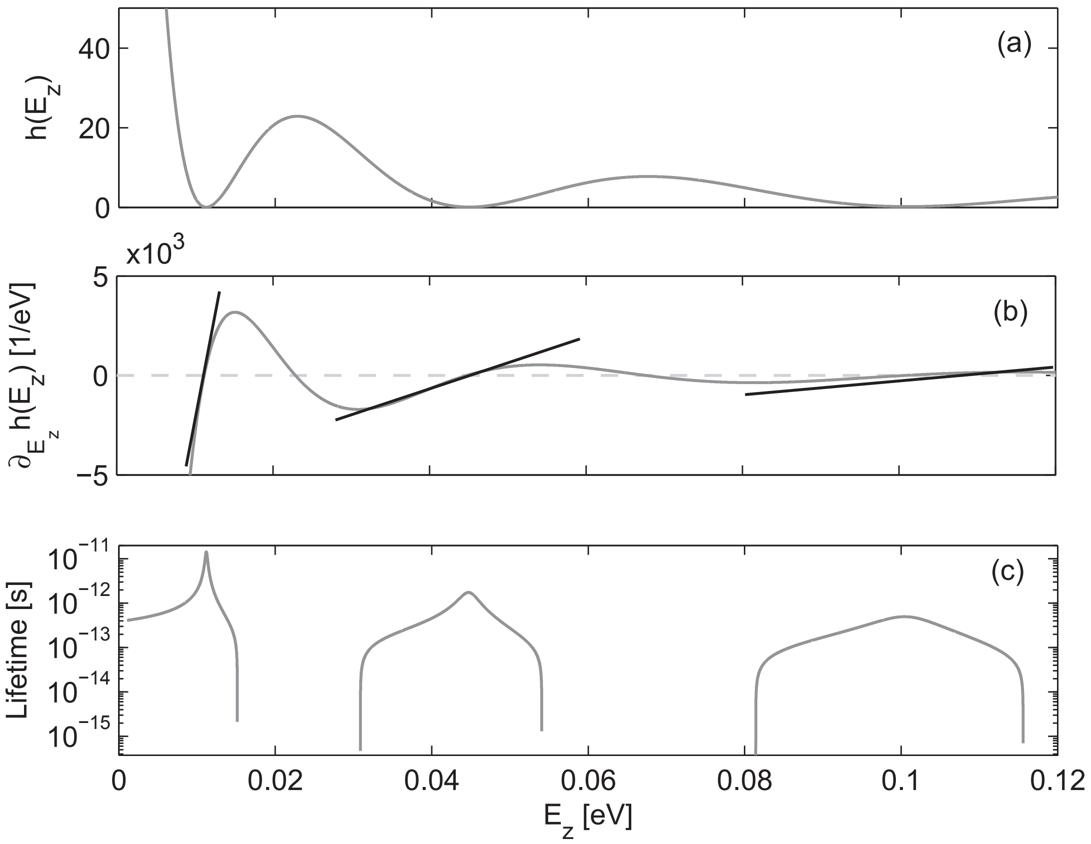

Figure 2.1.3: (a) h, (b) $\partial_{E_z} h$ and (c) lifetime as a function of the energy E_z for the case of a quantum well with 30 Å barrier.

2.1.3 Example: quasi bound states for a leaky quantum well

In this section we give an example for solving the Schrödinger equation based on the transfer matrix method. We want to find the quasi bound states for the potential

$$V(z) = \begin{cases} \infty, & z = 0 \\ 0, & 0 < z < z_1 \\ V_0 > 0, & z_1 \leq z \leq z_2 \\ 0, & z > z_2 \end{cases} . \tag{2.1.19}$$

The transfer matrices for the well, the barrier and the leakage region are defined by Eqs. (2.1.8), (2.1.9), (2.1.10) and (2.1.11). For the boundary conditions we assume $C_0 = 0$ and $D_0 = 1$, since there is no outgoing wave at $z = 0$, due to the infinite potential barrier. After multiplying the transfer matrices and applying the boundary conditions, we get

$$\begin{bmatrix} C_2 \\ D_2 \end{bmatrix} = \begin{bmatrix} \sin(k_{z_w} z_1) \cosh\left[k_{z_b}(z_2 - z_1)\right] + \cos(k_{z_w} z_1) \sinh\left[k_{z_b}(z_2 - z_1)\right] \dfrac{k_{z_w}}{k_{z_b}} \\ -\cos(k_{z_w} z_1) \cosh\left[k_{z_b}(z_2 - z_1)\right] - \sin(k_{z_w} z_1) \sinh\left[k_{z_b}(z_2 - z_1)\right] \frac{k_{z_b}}{k_{z_w}} \end{bmatrix} \tag{2.1.20}$$

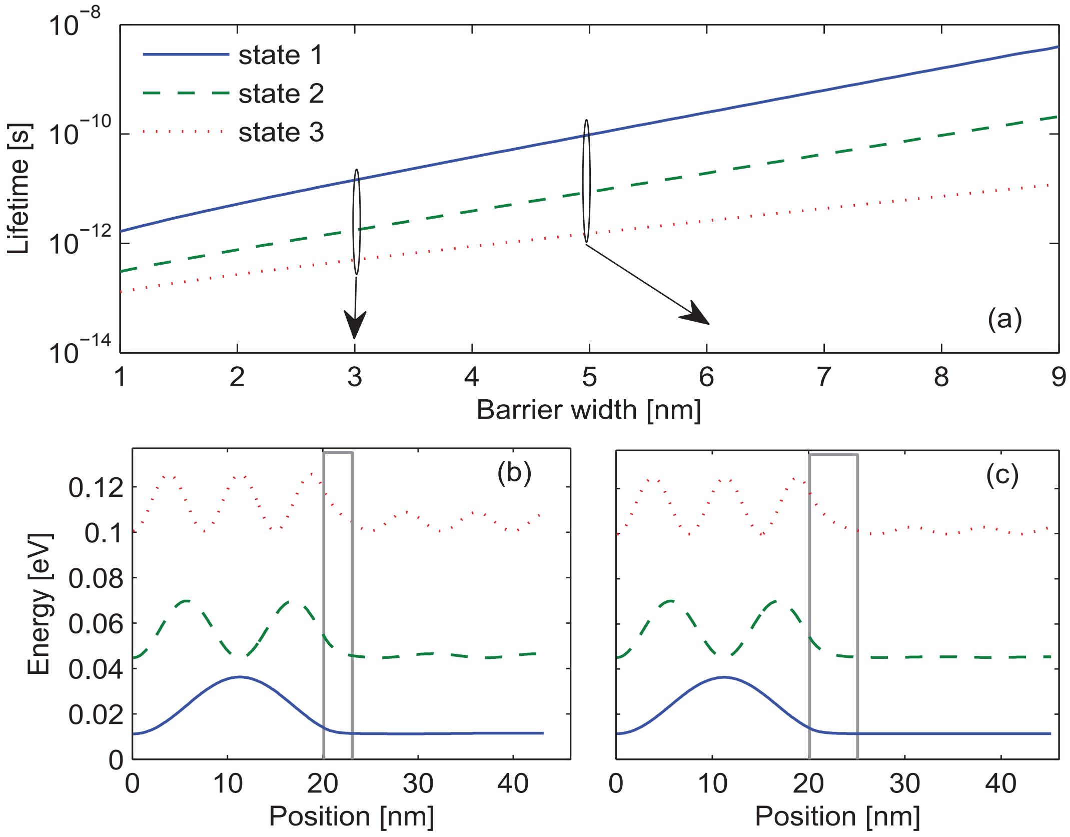

Figure 2.1.4: Lifetime as a function of barrier width and example states.

where

$$h(E_z) = |C_2|^2 + |D_2|^2 \tag{2.1.21}$$

and k_{z_b} and k_{z_w} are a function of the energy E_z as given by Eq. (2.1.5).

We now take the example of a GaAs/Al$_{0.15}$Ga$_{0.85}$As quantum well with uniform effective mass of $m_z^* = 0.067$, barrier width of 3 nm, well width of 20 nm and a conduction band offset $V_0 = 135$ meV. In Fig. 2.1.3 (a) $h(E_z)$ is shown. According to Eq. (2.1.14), the minima of this function give the energy levels of the quantum well as solutions of the Schrödinger equation. The derivative of $h(E_z)$ is shown in Fig. 2.1.3 (b), which has its zeros at the extrema of h. Our Schrödinger solver takes the zeros with positive slopes, marked by the straight lines in Fig. 2.1.3 (b) at these extrema, to find the minima of h corresponding to the energy levels. To classify the states with respect to their lifetime, the reciprocal of Eq. (2.1.18) is shown in Fig. 2.1.3 (c) on a log-scale. The maximum values of the three peaks represent the lifetime of the three energy states. We can see that the higher the energy, the lower the lifetime of the states, which is not necessarily true for the case of multi-quantum well structures. There the wavefunction localization also plays a role since states can be limited by only a few or several barriers, thus having decreased or increased lifetimes correspondingly. For the case of our quantum well a lower lifetime means that tunneling out of the well to the region $z > z_1$ occurs faster.

In Fig. 2.1.4 (a) we show the lifetime of the states as a function of barrier thickness. The linear increase on the logarithmic scale of Fig. 2.1.4 (a) corresponds to an exponential dependence of lifetime on barrier width. For small barrier thicknesses the picosecond order of lifetime is comparable to scattering times of electrons with phonons, roughness, electrons or impurities, thus tunneling can be as important as those effects. However, for a QCL structure, the leakage regions are avoided to suppress tunneling of electrons into the continuum. The low energy states in QCLs have lifetimes on the order of 100 picoseconds at least. The evolution of tunneling rates also highly depends on the QCL structure. In Fig. 2.1.4 (b) and (c) we show the solutions of the Schrödinger equation as found by the transfer matrix method. The leakage of the lowest state into the region $z > 23\,\mathrm{nm}$ (leakage region) is negligible. State 2 has already a slight change in the leakage region, while state 3 is highly delocalized. Comparing Fig. 2.1.4 (b) with Fig. 2.1.4 (c) we see a stronger localization of the states as the barrier thickness is increased from 3 nm to 5 nm.

2.2 Non-parabolicity

The parabolic dispersion relation between electron kinetic energy and wavenumber given by Eq. (2.1.5) usually breaks down for states lying high above the conduction band of the heterostructure. This is the case for mid-infrared QCLs, where lasing transitions are on the order of 100 meV, while the bandgap is small due to the high indium content. In this case, the correct energy-momentum relations are given by $\mathbf{k} \cdot \mathbf{p}$ methods, or an attempt to correct the parabolic dispersions by higher order terms can be performed. The non-parabolic corrections have to be implemented for the low-bandgap materials such as InGaAs. Our theory is inspired from the early work performed by Ekenberg [34] for implementing non-parabolicity by the energy dependent effective mass approach. In the following we will discuss non-parabolicity for the confined direction, for radiative and for non-radiative scattering rates. The derivations use the definition of kinetic energy expanded to second order [34]

$$\begin{aligned} E(\mathbf{K}) = {} & \frac{\hbar^2}{2m^*}\left(k_x^2 + k_y^2 + k_z^2\right) - \left(\frac{\hbar^2}{2m^*}\right)^2 \alpha \left(k_x^4 + k_y^4 + k_z^4\right) \\ & - \left(\frac{\hbar^2}{2m^*}\right)^2 (2\alpha + \beta)\left(k_x^2 k_y^2 + k_x^2 k_z^2 + k_y^2 k_z^2\right). \end{aligned} \tag{2.2.1}$$

Here α is the non-parabolicity parameter defined as $(E_g + \Delta_{so}/3)^{-1}$, where E_g and Δ_{so} are the energy gap and the difference between light hole and splitoff-hole energies respectively. The parameter β comes from a 14-band k.p model, and was determined in GaAs to be approximately equal to α, while in InGaAs the relation $2\alpha + \beta \equiv 1.7\alpha$ was found experimentally [35].

2.2.1 Non-parabolicity in growth direction

In the growth direction the states are confined, and the effective mass equation (2.1.1) should be solved for finding the energy levels. The implementation of non-parabolicity assumes the effective mass $m^*(z)$ to be energy dependent. We start our derivation from Eq. (2.2.1). By neglecting the momentum in the direction (k_x,k_y), we obtain for the kinetic energy

$$E_z^{kin} = -\left(\frac{\hbar^2}{2m_z^*}\right)^2 \alpha k_z^4 + \frac{\hbar^2}{2m_z^*} k_z^2. \tag{2.2.2}$$

Solving for k_z^2, we get the new dispersion relation

$$k_{z_{1,2}}^2 = \frac{m_z^*}{\alpha\hbar^2}\left(1 \pm \sqrt{1 - 4\alpha E_z^{kin}(k_z)}\right). \tag{2.2.3}$$

Since for $k_z = 0$ we expect $E_z^{kin}(k_z) = 0$, the first solution is dropped and the above equation can be written as

$$m_z^*\left(E_z^{kin}\right) = m_z^* \frac{1 - \sqrt{1 - 4\alpha E_z^{kin}}}{2\alpha E_z^{kin}}, \tag{2.2.4}$$

where $m_z^*\left(E_z^{kin}\right)$ is the energy dependent effective mass. We note that Eq. (2.2.1) is for the kinetic energy E_z^{kin} of the system. Thus, the kinetic energy in the confined direction is defined as the potential profile subtracted from the energy of the state $E_z^{kin} = E_n - V(z)$. Performing a second order Taylor expansion of the square root in Eq. (2.2.4) around 0 kinetic energy, we get

$$m_z^*\left(E_z^{kin}\right) \approx m_z^*\left(1 + \alpha E_z^{kin}\right). \tag{2.2.5}$$

The above equation is the conventional non-parabolic expression which assumes a linear dependence of the effective mass on energy [36, 37].

In the Schrödinger solver we implement non-parabolicity for two cases, preserving a continuous transition of the effective mass at $E_z^{kin} = 0$. For $E_z^{kin} < 0$ (for example in barriers) we use Eq. (2.2.4) for the energy dependent effective mass to avoid $m_z \leq 0$ in Eq. (2.2.5). For $E_z^{kin} \geq 0$ (wells or continuum) Eq. (2.2.5) is used for non-parabolicity. For the THz structures that are mainly based on GaAs/Al$_{0.15}$Ga$_{0.85}$As, the non-parabolic corrections are negligible for the relevant levels, and have only a slight influence on higher energy states. For InGaAs mid-infrared QCLs, however, the inclusion of non-parabolicity for transport calculations is mandatory for consistent modeling [38].

2.2.2 In-plane non-parabolicity for non-radiative scattering

Additional non-parabolicity for the in-plane dynamics needs to be included for low wavelength mid-infrared QCLs due to the high energetic spacing of the laser levels and the low bandgap of the material system. We correct the scattering rates by assigning a different effective mass to each energy level and using parabolic dispersion relations within these levels. The scattering rates are multiplied by the effective mass of the final level, instead of a uniform effective mass, as we will see in Sections 2.3.4, 2.3.5, 2.3.6, 2.3.7 and 2.3.8. We now derive the in-plane effective mass $m_{||}$ corrected by non-parabolicity, starting from the same equation as in the previous section. The term proportional to k_x^4 and k_y^4 is neglected in Eq. (2.2.1) and we get

$$E(\mathbf{K}) = -\left(\frac{\hbar^2}{2m^*}\right)^2 \alpha k_z^4 + \frac{\hbar^2}{2m^*}k_z^2 + \frac{\hbar^2 \left|\mathbf{k}\right|^2}{2m^*} - (2\alpha+\beta)\frac{\hbar^2 \left|\mathbf{k}\right|^2}{2m^*}\frac{\hbar^2 k_z^2}{2m^*}. \tag{2.2.6}$$

Here the first two terms were defined in the previous section as E_z^{kin}. In the last term, $\hbar^2 k_z^2/2/m^*$ can be also approximated by E_z^{kin} and we get

$$E(\mathbf{K}) \approx E_z^{kin} + \frac{\hbar^2 \left|\mathbf{k}\right|^2}{2m_{||}}\left[1 - (2\alpha+\beta)E_z^{kin}\right]. \tag{2.2.7}$$

The kinetic energy E_z^{kin} is defined in the z (confined) direction as $E_z^{kin} = E_n - V(z)$, where $V(z)$ is the potential profile of the structure and E_n is the energy level of the nth state. We multiply both the numerator and denominator of Eq. (2.2.7) by $1 + (2\alpha+\beta)\left[E_n - V(z)\right]$ and we get

$$E_n^{||}(\mathbf{k}) = E(\mathbf{K}) - E_z^{kin} = \frac{\hbar^2 \left|\mathbf{k}\right|^2}{2m_{||,n}(z)}\left\{1 - (2\alpha+\beta)^2\left[E_n - V(z)\right]^2\right\} \approx \frac{\hbar^2 \left|\mathbf{k}\right|^2}{2m_{||,n}(z)}, \tag{2.2.8}$$

where

$$m_{||,n}(z) = m_{||}\left[1 + (2\alpha+\beta)\left(E_n - V(z)\right)\right] \tag{2.2.9}$$

is the in-plane effective mass and $E_n^{||}(\mathbf{k})$ is the in-plane kinetic energy. In Eq. (2.2.8), the term $(2\alpha+\beta)^2\left[E_n - V(z)\right]^2$ was neglected, since $(2\alpha+\beta)\left(E_n - V(z)\right)$ is already small as required by the non-parabolic approximation. According to Eq. (2.2.9) the in-plane non-parabolicity for each state also depends on z. For simplicity, we avoid the z-dependence in EMC and we calculate instead the 'average' effective mass for each state

$$m_{||,n} = m_{||}\int \left\{1 + (2\alpha+\beta)\left[E_n - V(z)\right]\right\}\left|\psi_n(z)\right|^2 \mathrm{d}z. \tag{2.2.10}$$

In this way, the conventional parabolic dispersions can be used in each level, with the non-parabolic corrected parallel effective mass $m_{||,n}$. Energy conservation has to be re-evaluated, in the case presented above. In the Monte-Carlo solver the energy of an electron is written as

$$E_n(\mathbf{k}) = E_n + E_n^{||}(\mathbf{k}). \tag{2.2.11}$$

Energy conservation between an initial state n and final state m for elastic scattering is written as

$$E_n - E_m + \frac{\hbar^2 \left|\mathbf{k}\right|^2}{2m_{||,n}} - \frac{\hbar^2 \left|\mathbf{k}'\right|^2}{2m_{||,m}} \left(\pm\hbar\omega\right) = 0. \tag{2.2.12}$$

For the case of stimulated (photon and phonon) processes, the energy $\hbar\omega$ should be added/subtracted additionally in the above expression to account for emission/absorption respectively. We use Eq. (2.2.12) to determine the final in-plane wavevector

$$\left|\mathbf{k}'\right|^2 = \frac{2m_{||,m}}{\hbar^2}\left(E_n - E_m\right) + \left|\mathbf{k}\right|^2 \frac{m_{||,m}}{m_{||,n}}. \tag{2.2.13}$$

The above relation is used for determining the final wavevector in case of non-parabolic scattering in the EMC method. Additionally the non-radiative scattering rates are multiplied by the in-plane parabolic effective mass of the final state $m_{||,m}$ instead of the conventional in-plane effective mass. For the derivation of the scattering rates and further details of including non-parabolicity see Section 2.3.

2.2.3 In-plane non-parabolicity for optical transitions

Electrons interacting with the optical field do not change their momentum and Eq. (2.2.1) can be used in a more exact manner for deriving non-parabolicity. The kinetic energy for the initial state n, can be written as

$$\begin{aligned} E_n^{||}(\mathbf{k}) = E(\mathbf{K}) - E_n + V(z) &= \frac{\hbar^2\left|\mathbf{k}\right|^2}{2m^*} - \left(\frac{\hbar^2}{2m^*}\right)^2 \alpha\left(k_x^4 + k_y^4\right) \\ - \left(\frac{\hbar^2}{2m^*}\right)^2 (2\alpha+\beta)k_x^2k_y^2 &- \frac{\hbar^2\left|\mathbf{k}\right|^2}{2m^*}(2\alpha+\beta)\left(E_n - V(z)\right). \end{aligned} \tag{2.2.14}$$

For the final state m, we have the same in-plane momentum, thus

$$\begin{aligned} E_m^{||}(\mathbf{k}') = E(\mathbf{K}') - E_m + V(z) &= \frac{\hbar^2\left|\mathbf{k}\right|^2}{2m^*} - \left(\frac{\hbar^2}{2m^*}\right)^2 \alpha\left(k_x^4 + k_y^4\right) \\ - \left(\frac{\hbar^2}{2m^*}\right)^2 (2\alpha+\beta)k_x^2k_y^2 &- \frac{\hbar^2\left|\mathbf{k}\right|^2}{2m^*}(2\alpha+\beta)\left(E_m - V(z)\right). \end{aligned} \tag{2.2.15}$$

The first three terms and the terms proportional to $V(z)$ cancel out on the rhs. of Eqs. (2.2.14) and (2.2.15) when we invoke the energy conservation

$$E_m - E_n + E_m^{||}(\mathbf{k}') - E_n^{||}(\mathbf{k}) \pm \hbar\omega = 0 \tag{2.2.16}$$

which simplifies to

$$\left(E_m - E_n\right)\left[1 - \frac{\hbar^2\left|\mathbf{k}\right|^2}{2m^*}(2\alpha+\beta)\right] \pm \hbar\omega = 0. \tag{2.2.17}$$

For the implementation of lasing, only the difference of the kinetic energies in Eqs. (2.2.14) and (2.2.15) are used and we can keep Eq. (2.2.8) for the dispersion relation, with a spatially averaged effective mass. The advantage of using the energy conservation of Eq. (2.2.17) for lasing, instead of Eq. (2.2.12) is that we preserve **k**, which can overcome spurious absorptions in the gain spectra. For further details refer to Section 6.3.

We observe that the spatial-dependence in the growth direction cancels out. However the transitions are changed by the non-parabolic factor in Eq. (2.2.17). We recall that E_n and E_m are the initial and final states, calculated from the Schrödinger-Poisson solver and they are corrected by the perpendicular non-parabolicity. Eq. (2.2.17) is a direct result of momentum and energy conservation.

2.3 Fermi's golden rule

The theory needed for calculating the scattering rates, i.e., Fermi's golden rule, as well as the scattering rates themselves are derived in this section. We define a stationary system with its basis states, given by the solution of the Schrödinger equation. Fermi's golden rule assumes a small perturbation on this system, given by the Hamiltonian, or perturbation potential $H_{int}(t)$. We are interested in the effect of a small perturbation on the dynamics of the system, described by the basis states. It turns out that there will be a rate of electron flow between these basis states, which is given by the golden rule. We will take two special cases for the perturbation potential $H_{int}(t)$ which assume a static and a harmonic behavior. Both of these will be considered, based on time-dependent perturbation theory. The evolution equation for the state-coefficient in the interaction picture is given by

$$\dot{a}_m(t) = -\frac{i}{\hbar}\sum_j a_j(t) e^{i\frac{E_m(\mathbf{k}')}{\hbar}t - i\frac{E_j(\mathbf{k})}{\hbar}t} < m|H_{int}(t)|j > . \tag{2.3.1}$$

Here $a_m(t)$ is the coefficient of the mth basis function, E_m and E_n are the corresponding energy levels for states m and n. Further details for finding the above equation can be found in the Appendix. We assume that we are in the initial state n with 1 probability, i.e., $a_n^{(0)} = 1$, $a_{j\neq n}^{(0)} = 0$ and the final state of the quantum system is $|m>$. In this case it is possible to integrate Eq. (2.3.1) to get the first order perturbation of the coefficient

$$a_m^{(1)}(t) = -\frac{i}{\hbar}\int_0^t \left(< m|H_{int}(\tau)|n > e^{i\frac{E_m(\mathbf{k}')-E_n(\mathbf{k})}{\hbar}\tau}\right) \mathrm{d}\tau. \tag{2.3.2}$$

The first order perturbation will give Fermi's golden rule, depending on the perturbation type (harmonic-sine or static-step function).

2.3.1 The envelope wavefunction

For our theoretical modeling of the crystal structure of semiconductors we use an envelope function given as

$$\Psi_n(x,y,z) =< x,y,z||n >= \frac{1}{\sqrt{L_x L_y}}\psi_n(z)e^{-ik_x x - ik_y y}, \tag{2.3.3}$$

where $\psi_n(z)$ is the solution of the Schrödinger equation for the state n in growth direction. ψ_n is calculated by the numerical solution of the Schrödinger equation as discussed in Section 2.1. The above function describes electrons as plane-waves in transverse direction, with the size of the device cross section in x and y directions L_x and L_y and the area of the cross section $A = L_x L_y$. The electron behavior in the confinement direction is given by the function ψ_n while in the planar directions it can have different crystal momenta as given by $\mathbf{p} = \hbar\mathbf{k}$. Scattering mechanisms for static and harmonic perturbations will be calculated in the basis of the above envelope functions, thus we treat them in three dimensions.

2.3.2 Harmonic perturbation

If we know that the system changes harmonically in time $H_{int}(t) = 2\hat{V}\cos(\omega t)$, the perturbation matrix element has the form

$$< m|H_{int}(\tau)|n >= 2\cos(\omega\tau) < m|\hat{V}|n >= 2V(E_m(\mathbf{k}'), E_n(\mathbf{k}))\cos(\omega\tau). \tag{2.3.4}$$

Here V represents the amplitude of the perturbation as a function of the initial and final state energies $E_m(\mathbf{k}')$ and $E_n(\mathbf{k})$, where $E_n(\mathbf{k}) = E_n + \hbar^2 k^2/2m_{||,n}$. The indices n and m represent the initial and final state. It is assumed that the system is in its initial state n, and we want to find the probability that the system will be in the mth state after some time τ. This is done by taking the absolute square of the mth coefficient of the system $\left|a_m^{(1)}(t)\right|^2$. Substituting Eq. (2.3.4) into Eq. (2.3.2) we get the first order approximation for the mth coefficient

$$\begin{aligned} a_m^{(1)}(t) &= -\frac{iV(E_m(\mathbf{k}'), E_n(\mathbf{k}))}{\hbar}\int\limits_0^t \left(e^{i(\omega+\omega_{mn})\tau} + e^{-i(\omega-\omega_{mn})\tau}\right) \mathrm{d}\tau = \\ &= -\frac{V(E_m(\mathbf{k}'), E_n(\mathbf{k}))}{\hbar}\left(\frac{e^{i(\omega+\omega_{mn})t}-1}{\omega+\omega_{mn}} - \frac{e^{-i(\omega-\omega_{mn})t}-1}{\omega-\omega_{mn}}\right), \end{aligned} \tag{2.3.5}$$

where

$$\omega_{mn} = \frac{E_m(\mathbf{k}') - E_n(\mathbf{k})}{\hbar}. \tag{2.3.6}$$

We now calculate the absolute-square of $a_m^{(1)}(t)$, giving the probability for the final state

$$\left|a_m^{(1)}(t)\right|^2 = \frac{|V(E_m(\mathbf{k}'), E_n(\mathbf{k}))|^2}{\hbar^2} \left[t^2 \mathrm{sinc}^2\left(\frac{\omega + \omega_{mn}}{2}t\right) + \right.$$

$$\left. + t^2 \mathrm{sinc}^2\left(\frac{\omega - \omega_{mn}}{2}t\right) + 2t^2\cos(\omega t)\mathrm{sinc}\left(\frac{\omega + \omega_{mn}}{2}t\right)\mathrm{sinc}\left(\frac{\omega - \omega_{mn}}{2}t\right)\right], \qquad (2.3.7)$$

with $\mathrm{sinc}(x) = \sin(x)/x$. In the above equation, $\mathrm{sinc}(at)$ and $\mathrm{sinc}^2(at)$ functions can be approximated by $\delta(a)$ functions since:

1. For large t, the $\mathrm{sinc}(at)$ and $\mathrm{sinc}^2(at)$ function approach 0 everywhere except around $a = 0$.
2. The integrals $c_1 \cdot \int_{-\infty}^{\infty} \mathrm{sinc}(at)\mathrm{d}a$ and $c_2 \cdot \int_{-\infty}^{\infty} \mathrm{sinc}^2(at)\mathrm{d}a$ give 1, where c_1 and c_2 are normalization constants.

We assume that the frequency terms in Eq. (2.3.7) fulfill the conditions $(\omega + \omega_{mn})t \gg 1$ and $(\omega - \omega_{mn})t \gg 1$ after a large amount of time and we can approximate the $\mathrm{sinc}^2(at)$ and $\mathrm{sinc}^2(at)$ terms of Eq. (2.3.7) as

$$\mathrm{sinc}^2\left(\frac{\omega \pm \omega_{mn}}{2}t\right) \approx \frac{2\pi\hbar}{t}\delta(E_m(\mathbf{k}') - E_n(\mathbf{k}) \pm \hbar\omega) \qquad (2.3.8)$$

and

$$\mathrm{sinc}\left(\frac{\omega \pm \omega_{mn}}{2}t\right) \approx \frac{2\pi\hbar}{t}\delta(E_m(\mathbf{k}') - E_n(\mathbf{k}) \pm \hbar\omega). \qquad (2.3.9)$$

Fermi's golden rule, giving the transition rate, is found by using the approximations in Eqs. (2.3.8) and (2.3.9) and by neglecting the last term (interference term) of Eq. (2.3.7), yielding the transition rate

$$W_{n\mathbf{k}m\mathbf{k}'} = \frac{\partial}{\partial t}\left|a_m^{(1)}(t)\right|^2 \approx \frac{2\pi}{\hbar}|V(E_m(\mathbf{k}'), E_n(\mathbf{k}))|^2\delta(E_m(\mathbf{k}') - E_n(\mathbf{k}) \pm \hbar\omega). \qquad (2.3.10)$$

In Eq. (2.3.10), the $+\hbar\omega$ represents the emission and $-\hbar\omega$ represents the absorption of energy.

2.3.3 Static perturbation

Static perturbation of the system assumes a constant behavior in time. We define the perturbing Hamiltonian of Eq. (2.3.2) as the step function

$$< m|H_{int}(\tau)|n >= \begin{cases} V(E_m(\mathbf{k}'), E_n(\mathbf{k})) & \tau \geq 0 \\ 0 & \tau < 0 \end{cases}. \qquad (2.3.11)$$

With the above, we use Eq. (2.3.2) to find the time varying coefficient in the interaction picture. The absolute square of the variable $a_m^{(1)}(t)$ gives the probability in time, that the electron is in the mth state

$$\left|a_m^{(1)}(t)\right|^2 = \frac{|V(E_m(\mathbf{k}'), E_n(\mathbf{k}))|^2}{\hbar^2}\frac{2 - 2\cos(\omega_{mn}t)}{\omega_{mn}^2} = \frac{|V(E_m(\mathbf{k}'), E_n(\mathbf{k}))|^2}{\hbar^2}t^2\mathrm{sinc}^2\left(\frac{\omega_{mn}}{2}t\right). \qquad (2.3.12)$$

For large t the $\text{sinc}^2(at)$ function tends to a $\delta(a)$ function, because:

1. For large t, the $\text{sinc}^2(at)$ function approaches 0 everywhere, except around $a = 0$.
2. The integral $c \cdot \int\limits_{-\infty}^{\infty} \text{sinc}^2(at)\text{d}a$ gives 1, where c is a constant.

By using the same arguments for the replacement of sinc-functions by δ-functions as in Section 2.3.2, we have

$$\int\limits_{-\infty}^{\infty} \frac{\sin^2\left(\frac{\omega_{mn}}{2}t\right)}{\frac{\omega_{mn}^2}{4}} \text{d}\left(E_m(\mathbf{k}') - E_n(\mathbf{k})\right) = 2\pi\hbar t \Rightarrow \text{sinc}^2\left(\frac{\omega_{mn}}{2}t\right) \approx \frac{2\pi\hbar}{t}\delta(E_m(\mathbf{k}') - E_n(\mathbf{k})). \tag{2.3.13}$$

Using the approximation from Eq. (2.3.13) in Eq. (2.3.12), Fermi's golden rule in case of static perturbations is given by

$$W_{n\mathbf{k}m\mathbf{k}'} = \frac{2\pi}{\hbar}|V(E_m(\mathbf{k}'), E_n(\mathbf{k}))|^2\delta(E_m(\mathbf{k}') - E_n(\mathbf{k})). \tag{2.3.14}$$

2.3.4 LO polar phonon scattering

Longitudinal optical phonons are lattice vibrations produced by oscillating charges or atoms with different proton numbers in polar (alloy) semiconductors. The strong oscillation of the dipole moments in the unit cell of a crystal produce an electric field that scatters the carriers. The source of the vibrations is the finite temperature of the lattice. We start by writing the oscillation of a two-body system, representing the atoms that produce a single phonon. The equation of motion is derived from Newton's law for an ion-pair displacement $\mathbf{u}$, by performing a first order Taylor expansion of the force $\mathbf{F}$ as

$$m_{nucl}\frac{\partial^2\mathbf{u}}{\partial t^2} = \frac{\partial\mathbf{F}(0)}{\partial\mathbf{u}}\mathbf{u} + \mathbf{F}(0). \tag{2.3.15}$$

Here $m_{nucl} = (m_1^{-1} + m_2^{-1})^{-1}$ is the reduced mass of the oscillating ions with mass m_1 and m_2. From the Lorentz force equation

$$\mathbf{F} = q_0\left[\mathbf{E}_{latt} + \mathbf{v} \times \mathbf{B}\right] \tag{2.3.16}$$

we can write $\mathbf{F}(0)$ in Eq. (2.3.15), where the charge q_0 is written in terms of an effective charge, e_{eff} times the electron charge as $q_0 = e_{eff}e_0$ and we define $\sqrt{\frac{1}{m_{nucl}}\frac{\partial\mathbf{F}(0)}{\partial\mathbf{u}}}$ as the imaginary unit, multiplied by the transverse optical vibration frequency of the lattice $i\omega_{TO}$. We can write Eq. (2.3.15) by using these notations as

$$\frac{\partial^2\mathbf{u}}{\partial t^2} = -\omega_{TO}^2\mathbf{u} + \frac{e_{eff}e_0}{m_{nucl}}\mathbf{E}_{latt}, \tag{2.3.17}$$

where $\mathbf{E}_{latt}$ is the electric field produced by the longitudinal lattice vibrations. The electric displacement current $\mathbf{D}$ is the sum of the polarization and the electric field $\mathbf{E}_{latt}$

$$\mathbf{D} = \varepsilon_{r,\infty}\mathbf{E}_{latt} + \mathbf{P}_{ion}, \tag{2.3.18}$$

where $\varepsilon_{r,\infty}$ is the high frequency dielectric constant. The polarization is given by the oscillating dipoles $\mathbf{P}_{ion} = e_{eff}e_0 n_{cells}\mathbf{u}$ described by Eq. (2.3.17), where n_{cells} denotes the number of ion pairs per unit volume. Since phonons are lattice vibrations we can assume that the lattice displacement vector takes the general form of

$$\mathbf{u} = \mathbf{U_0}\cos(\mathbf{QR} + \omega_{\mathbf{Q}}t), \tag{2.3.19}$$

where $\mathbf{Q}$ is the three dimensional wavevector of the phonon, $\mathbf{R}$ is its spatial position and $\omega_{\mathbf{Q}}$ its frequency. It is assumed that the electric field, polarization and displacement current follow the oscillations of the displacement vector. Hence, the derivative of the field and polarization can be defined as

$$\nabla\mathbf{E}_{latt} = \mathbf{E}^0_{latt}\mathbf{Q}\sin(\mathbf{QR} + \omega_{\mathbf{Q}}t) \tag{2.3.20}$$

and

$$\nabla\mathbf{P}_{ion} = \mathbf{P}^0_{ion}\mathbf{Q}\sin(\mathbf{QR} + \omega_{\mathbf{Q}}t), \tag{2.3.21}$$

which by using Eq. (2.3.18) implies that

$$\nabla\mathbf{D} = \mathbf{D}_0\mathbf{Q}\sin(\mathbf{QR} + \omega_{\mathbf{Q}}t). \tag{2.3.22}$$

Writing Eq. (2.3.18) by using Eqs. (2.3.20), (2.3.21) and (2.3.22) we get in terms of amplitudes

$$(\mathbf{D}_0 - \varepsilon_{r,\infty}\mathbf{E}^0_{latt} + \mathbf{P}^0_{ion})\mathbf{Q} = 0. \tag{2.3.23}$$

The above equation can be 0 in two cases:

1. Transverse vibrations $\mathbf{Q}\perp\mathbf{u}_T$, which imply $\nabla\mathbf{E}_{latt} = 0$ from Eq. (2.3.20) and $\mathbf{E}_{latt} = \mathbf{E}_T = 0$ in the transverse direction.

2. Longitudinal vibrations $\mathbf{Q} \parallel \mathbf{u}_L$, requiring that

$$\mathbf{E}_{latt} = \mathbf{E}_L = -\frac{\mathbf{P}_{ion}}{\varepsilon_{r,\infty}} = -\frac{e_{eff}e_0 n_{cells}}{\varepsilon_{r,\infty}}\mathbf{u}_L, \tag{2.3.24}$$

since the displacement current $\mathbf{D}$ is 0. The 0 displacement current follows from $\nabla\mathbf{D} = 0$, $\mathbf{D}||\mathbf{Q} \Rightarrow \mathbf{D}_0 = 0 \Rightarrow \mathbf{D} = 0$.

In the above cases, the displacement vector $\mathbf{u}$ and the electric field $\mathbf{E}_{latt}$was decomposed into a longitudinal and a transverse part $\mathbf{u} = \mathbf{u}_L + \mathbf{u}_T$ and $\mathbf{E}_{latt} = \mathbf{E}_T + \mathbf{E}_L$. Using the argumentation (1) and (2) we can write from Eq. (2.3.17) two equations of motion

$$\frac{\partial^2 \mathbf{u}_T}{\partial t^2} = -\omega_{TO}^2 \mathbf{u}_T \tag{2.3.25}$$

for transverse optical (TO) phonons and

$$\frac{\partial^2 \mathbf{u}_L}{\partial t^2} = -\left(\omega_{TO}^2 + \frac{e_{eff}^2 e_0^2 n_{cells}}{m_{nucl}\varepsilon_{r,\infty}}\right)\mathbf{u}_L \tag{2.3.26}$$

for longitudinal optical phonons (LO-phonons). The displacement current in the general case can be written as the sum of the electric field and the polarization

$$\mathbf{D} = \varepsilon(\omega_{\mathbf{Q}})\mathbf{E}_{latt} = \varepsilon_{r,\infty}\mathbf{E}_{latt} + \mathbf{P}_{ion}. \tag{2.3.27}$$

For TO phonons we know that $\mathbf{E}_{latt} = \mathbf{E}_T = 0$ and $\mathbf{P}_{ion} = \mathbf{D} = 0$. We note that the above expression should give 0 for LO-phonons as well. The only way for this is $\varepsilon(\omega_{LO}) = 0$ since the electric field $\mathbf{E}_{latt} \neq 0$. The frequency dependent dielectric constant is then obtained from Eqs. (2.3.26), (2.3.17) and (2.3.27)

$$\varepsilon(\omega) = \varepsilon_{r,\infty} + \frac{(e_0 e_{eff})^2}{m_{nucl}\left(\omega_{TO}^2 - \omega^2\right)} n_{cells}. \tag{2.3.28}$$

We can write the squared effective charge e_{eff}^2 as a function of the dielectric constants at very small and very high frequencies as

$$e_{eff}^2 = m_{nucl}\frac{\varepsilon(0) - \varepsilon(\infty)}{n_{cells} e_0^2}\omega_{TO}^2, \tag{2.3.29}$$

by using Eq. (2.3.28). Here $\varepsilon(0) = \varepsilon_{r,0}$ is the static dielectric constant of the system. Solving for $\varepsilon(\omega) = 0$ and using Eq. (2.3.29), we get for the LO-phonon frequency

$$\omega_{LO} = \omega_{TO}\sqrt{\frac{\varepsilon_{r,0}}{\varepsilon_{r,\infty}}}. \tag{2.3.30}$$

This frequency is the longitudinal solution of Eq. (2.3.17), i.e., the equation of the simple harmonic oscillator, after assuming that the electric field only contributes to the longitudinal components of the displacement vector $\mathbf{u}$. From Eqs. (2.3.24) and (2.3.29), the electric field for the LO-phonons can be written as

$$\mathbf{E}_{latt} = -\omega_{LO}\sqrt{n_{cells} m_{nucl}(\varepsilon_{r,\infty}^{-1} - \varepsilon_{r,0}^{-1})}\mathbf{u}. \tag{2.3.31}$$

The amplitude of the displacement vector from Eq. (2.3.19) can be calculated by applying the quantization condition to the effective energy of the system as

$$\hbar\omega_{\mathbf{Q}} = V_c n_{cells} \frac{\omega_{\mathbf{Q}}}{2\pi} \int\limits_0^{\frac{2\pi}{\omega_{\mathbf{Q}}}} m_{nucl} \left(\frac{\partial \mathbf{u}}{\partial t}\right)^2 \mathrm{d}t = V_c n_{cells} \frac{1}{2} m_{nucl} \omega_{\mathbf{Q}}^2 \left(\mathbf{U_0}\right)^2 . \tag{2.3.32}$$

We find the amplitude of the lattice displacements from the above equation as

$$|\mathbf{U_0}| = \sqrt{\frac{2\hbar}{V_c n_{cells} m_{nucl} \omega_{LO}}}. \tag{2.3.33}$$

For the LO-phonon scattering rate, the perturbation potential is found by integrating the electric field in Eq. (2.3.31), with the displacement vector definition from Eq. (2.3.19)

$$\hat{V}_{pert} = -e_0 \int \mathbf{E}_{latt} d\mathbf{R} = iM(Q) \left[e^{i(\mathbf{QR} - \omega_{\mathbf{Q}} t)} - e^{-i(\mathbf{QR} - \omega_{\mathbf{Q}} t)} \right], \tag{2.3.34}$$

where

$$M(Q) = \frac{1}{2Q} e_0 \sqrt{\varepsilon_{r,\infty}^{-1} - \varepsilon_{r,0}^{-1}} \sqrt{\frac{2\hbar\omega_{LO}}{V_c}}. \tag{2.3.35}$$

The displacement amplitude is parallel to the phonon wavevector ($\mathbf{U_0} \| \mathbf{Q}$), thus we can write for $\mathbf{QU_0}/|\mathbf{Q}|^2 = U_0/Q$. The perturbation potential in Eq. (2.3.34) is used with the wavefunctions of Eq. (2.3.3), to find the absolute square of the matrix element

$$\begin{aligned} \left|V_{nm}^{LOPh}\right|^2 &= \left|< m|\hat{V}_{pert}|n >\right|^2 = \\ = M(Q)^2 &\left| \int\limits_{-\frac{L_x}{2}}^{\frac{L_x}{2}} \int\limits_{-\frac{L_y}{2}}^{\frac{L_y}{2}} \int\limits_{-\frac{L_z}{2}}^{\frac{L_z}{2}} \frac{1}{L_x L_y} \left[e^{i(q_z z - \omega_{\mathbf{Q}} t) + i(\mathbf{q} - \mathbf{k} + \mathbf{k}')\mathbf{r}} - e^{-i(q_z z - \omega_{\mathbf{Q}} t) + i(-\mathbf{q}_{||} - \mathbf{k} + \mathbf{k}')\mathbf{r}} \right] \psi_n(z) \psi_m^*(z) \mathrm{d}^3\mathbf{R} \right|^2 = \\ = M(Q)^2 &\left| \int\limits_{-\frac{L_z}{2}}^{\frac{L_z}{2}} \mathrm{sinc}(k'_x - k_x + q_x) \mathrm{sinc}(k'_y - k_y + q_y) e^{i(q_z z - \omega_{\mathbf{Q}} t)} \psi_n(z) \psi_m^*(z) \mathrm{d}z - \right. \\ &\left. - \int\limits_{-\frac{L_z}{2}}^{\frac{L_z}{2}} \mathrm{sinc}(k'_x - k_x - q_x) \mathrm{sinc}(k'_y - k_y - q_y) e^{-i(q_z z - \omega_{\mathbf{Q}} t)} \psi_n(z) \psi_m^*(z) \mathrm{d}z \right|^2 \end{aligned} \tag{2.3.36}$$

The squared perturbation potential represents at this point both phonon emission and absorption. Since $\mathbf{q}$ cannot be equal to $\mathbf{k} - \mathbf{k}'$ and $\mathbf{k}' - \mathbf{k}$ at the same time, and we neglect interferences, i.e., terms like $\mathrm{sinc}(q_x - k'_x + k_x)\mathrm{sinc}(q_x - k_x + k'_x)$, we can separate the above matrix element to two different scattering mechanisms, one for phonon emission and one for absorption. We can rewrite the two cases as

$$\left|V_{nm}^{LOPh}\right|_{e,a}^2 = \frac{4\pi^2}{L_x L_y} M(Q)^2 \delta(\mathbf{k}' - \mathbf{k} \pm \mathbf{q}) \left| \int e^{\pm i(q_z z - \omega_{\mathbf{Q}} t)} \psi_n(z) \psi_m^*(z) \mathrm{d}z \right|^2 , \tag{2.3.37}$$

where the "sinc" functions are approximated by δ functions in Eq. (2.3.36). Performing a sum over the phonon wavevector, and converting the sum into an integral by using $\sum\limits_{\mathbf{Q}} \rightarrow \frac{V_c}{8\pi^3} \int\int\int \mathrm{d}^3\mathbf{Q}$, we get the total scattering matrix element between the electron and phonon system

$$\begin{aligned}
\left\langle \left|V_{nm}^{LOPh}\right|_{e,a}^2 \right\rangle_Q &= e_0^2 \left(\varepsilon_{r,\infty}^{-1} - \varepsilon_{r,0}^{-1}\right) \frac{\hbar\omega_{LO}}{4\pi L_x L_y} \int \frac{1}{\left|\mathbf{k}-\mathbf{k}'\right|^2 + q_z^2} \left| \int e^{\pm i(q_z z - \omega_{\mathbf{Q}} t)} \psi_n(z) \psi_m^*(z) \mathrm{d}z \right|^2 \mathrm{d}q_z = \\
&= e_0^2 \left(\varepsilon_{r,\infty}^{-1} - \varepsilon_{r,0}^{-1}\right) \frac{\hbar\omega_{LO}}{4\pi L_x L_y} \int\int \frac{1}{\left|\mathbf{k}-\mathbf{k}'\right|^2 + q_z^2} e^{\pm i q_z (z-z')} \mathrm{d}q_z \psi_n(z) \psi_n^*(z') \psi_m^*(z) \psi_m(z') \mathrm{d}z\mathrm{d}z' = \\
&= e_0^2 \left(\varepsilon_{r,\infty}^{-1} - \varepsilon_{r,0}^{-1}\right) \frac{\hbar\omega_{LO}}{4\pi L_x L_y} J(|\mathbf{k}-\mathbf{k}'|).
\end{aligned} \tag{2.3.38}$$

Here, the in-plane phonon wavenumber is $q = |\mathbf{k}-\mathbf{k}'|$ since we have used the momentum conservation in Eq. (2.3.37). Furthermore, we have defined the quantity J, that is proportional to the electron-phonon form factors. This quantity is numerically evaluated in EMC as

$$J(q) = \int\int \frac{\pi}{|\mathbf{k}-\mathbf{k}'|} e^{-|\mathbf{k}-\mathbf{k}'||z-z'|} \psi_n(z) \psi_n^*(z') \psi_m^*(z) \psi_m(z') \mathrm{d}z\mathrm{d}z', \tag{2.3.39}$$

for every initial state n and final state m. We now apply Fermi's golden rule for harmonic perturbations from Eq. (2.3.10), with the perturbation potential from Eq. (2.3.38) and sum over the final wavevectors $\mathbf{k}'$, to find the electron LO-phonon scattering rate

$$W_{n\mathbf{k}m}^{e,a} = \frac{m_{||,m} e_0^2 \omega_{LO}}{8\pi^2 \hbar^2} \left(N_{Ph} + \frac{1}{2} \pm \frac{1}{2}\right) \left(\varepsilon_{r,\infty}^{-1} - \varepsilon_{r,0}^{-1}\right) \int\limits_0^{2\pi} J(q) \mathrm{d}\theta. \tag{2.3.40}$$

Here the sum was converted to an integral using

$$\sum_{\mathbf{k}'} \rightarrow \frac{L_x L_y m_{||,m}}{4\pi^2 \hbar^2} \int_0^{2\pi} \int_{E_m}^{\infty} \mathrm{d}E_m(\mathbf{k}') \mathrm{d}\theta, \tag{2.3.41}$$

and q is defined as

$$\begin{aligned}
q(\theta) = |\mathbf{k}-\mathbf{k}'| = \Bigg(& k^2 \left(1 + \frac{m_{||,m}}{m_{||,n}}\right) - 2k \sqrt{\frac{m_{||,m}}{m_{||,n}} k^2 + \frac{2m_{||,m}}{\hbar^2} \left(E_n - E_m \mp \hbar\omega_{LO}\right)} \cos(\theta) + \\
& + \frac{2m_{||,m}}{\hbar^2} \left(E_n - E_m \mp \hbar\omega_{LO}\right) \Bigg)^{1/2}.
\end{aligned} \tag{2.3.42}$$

In the above expression, the scattering angle between electron initial and final wavevectors is given by θ. The spatial integral terms in Eq. (2.3.39) are the so-called LO-phonon form factors, while the integral over the angle in Eq. (2.3.40) is called the theta-integral. The theta integral is a common numerical integral that has to be evaluated for most of the scattering rates. In EMC the rates are tabulated with respect to n, m and $\mathbf{k}$, where in each tabulation, the theta-integral is stored. $N_{Ph} + 1$ and N_{Ph} stand for the number of LO-phonons emitted and absorbed which multiply the rates for phonon emission and absorption to account for scattering with all the phonons and

$$N_{Ph} = \left[\exp\left(\frac{\hbar\omega_{LO}}{k_B T}\right) - 1\right]^{-1} \tag{2.3.43}$$

is given by the Bose-Einstein distribution. The +1 in the case of $N_{Ph} + 1$, accounts for spontaneous emission.

2.3.5 Impurity scattering

In doped semiconductors, the transport electrons interact with the donors through the conduction band bending and through Coulomb forces. The doping is taken into account by the Poisson equation which produces conduction band bending and thus can modify the alignment of the states. In the planar direction, ionized donors can also contribute to the dynamics of electron transport. We implement the impurity scattering in this section to account for the complete treatment of the donor-related effects in EMC. The perturbation potential produced by a single ionized impurity at the position of z_{imp} is given by the Coulomb potential,

$$V_{pert}^{imp}(\mathbf{r}) = \frac{e_0^2}{4\pi\varepsilon\sqrt{r^2 + |z - z_{imp}|^2}}. \tag{2.3.44}$$

Our wavefunctions provided by the Schrödinger solver in Section 2.1 are extended in transverse direction as shown in Eq. (2.3.3), giving the three dimensional wavefunctions of the system. We need to calculate the matrix element in the basis of these functions for applying Fermi's golden rule. For an initial state n and a final state m we calculate the matrix element as

$$V_{nm}^{imp} = A^{-1} \int\int V_{pert}^{imp} e^{-i\mathbf{qr}} \mathrm{d}^2\mathbf{r} \psi_m^* (z) \psi_n (z) \mathrm{d}z, \tag{2.3.45}$$

where $\mathbf{q} = \mathbf{k} - \mathbf{k}'$. Switching to polar coordinates and integrating in the planar directions, we get

$$\begin{aligned} V_{nm}^{imp} &= \frac{e_0^2}{4\pi\varepsilon A} \int \int_0^\infty \int_0^{2\pi} \frac{r e^{-\mathrm{i}qr\cos(\theta)}}{\sqrt{r^2 + |z - z_{imp}|^2}} d\theta dr \psi_m^* (z) \psi_n (z) \mathrm{d}z = \\ &= \frac{e_0^2}{2\varepsilon A} \int \int_0^\infty \frac{r J_0(qr)}{\sqrt{r^2 + |z - z_{imp}|^2}} dr \psi_m^* (z) \psi_n (z) \mathrm{d}z = \\ &= \frac{e_0^2}{2A\varepsilon q} \int \psi_m^* (z) \psi_n (z) e^{-q|z - z_{imp}|} \mathrm{d}z. \end{aligned} \tag{2.3.46}$$

Here we observe that the inner integral in Eq. (2.3.45) is the same as taking the Fourier transform of Eq. (2.3.44). In the above equation, $J_0(qr)$ stands for the Bessel function of the first kind. The relevant part of the above equation is the end result giving the matrix element V_{mn}^{imp}. The square of V_{mn}^{imp} is needed for calculating the scattering rate by the use of Fermi's golden rule. For finding the interaction of the electron with the potential provided by all the impurities, we sum over the position of the impurities z_{imp}

$$\left|V_{nm}^{imp,total}\right|^2 = \frac{1}{A}\left(\frac{e_0^2}{2\varepsilon q}\right)^2 f_{mn}^{imp}, \tag{2.3.47}$$

where the electron-impurity form factors between an initial state n and a final state m in the EMC solver are defined as

$$f_{nm}^{imp} = \int\left[\int \psi_m^*\left(z\right)\psi_n\left(z\right)e^{-q\left|z-z'\right|}dz\right]^2 N(z')\mathrm{d}z'. \tag{2.3.48}$$

The function $N(z)$ is the volume density of the donors if z is in the doped region and 0 otherwise. In Eq. (2.3.47), the summation over impurities was converted to an integral using the integral definition $\sum f(z_i)\Delta z \approx \int f(z)\mathrm{d}z$. Furthermore instead of A^2, we have A in the denominator since the average distance Δz between two impurities is given by $\Delta z_{imp} = A^{-1}N^{-1}(z)$. We now apply Fermi's golden rule for static perturbations from Eq. (2.3.14) to find the scattering rate

$$W_{n\mathbf{k}m\mathbf{k}'} = \frac{2\pi}{\hbar}\frac{1}{A}\left(\frac{e_0^2}{2\varepsilon q}\right)^2 f_{mn}^{imp}\delta\left(E_m(\mathbf{k}') - E_n(\mathbf{k})\right). \tag{2.3.49}$$

Finally to find the scattering rate from an initial state n and initial wavevector $\mathbf{k}$ to a final state m, we need to sum Eq. (2.3.49) over $\mathbf{k}'$ and convert the sum to an integral using Eq. (2.3.41) to get

$$\begin{aligned} W_{n\mathbf{k}m} &= \frac{2\pi}{\hbar}\frac{1}{A}\left(\frac{e_0^2}{2\varepsilon}\right)^2 f_{mn}^{imp}\sum_{\mathbf{k}'}\frac{1}{q^2}f_{mn}^{imp}\delta\left(E_m - E_n + \frac{\hbar^2\left|\mathbf{k}'\right|^2}{2m_{||,m}} - \frac{\hbar^2\left|\mathbf{k}\right|^2}{2m_{||,n}}\right) = \\ &= \frac{m_{||,m}e_0^4}{8\pi\varepsilon^2\hbar^3}\int_0^{2\pi}\frac{f_{mn}^{imp}(q(\theta))}{q^2(\theta)}\mathrm{d}\theta. \end{aligned} \tag{2.3.50}$$

The effective masses $m_{||,n}$ and $m_{||,m}$ are for the initial and final state and they were introduced in Section 2.2.2. The above scattering rate is used in EMC for impurity scattering, where q is defined by Eq. (2.3.42), with $\omega_{LO} = 0$.

2.3.6 Interface roughness scattering

The interface between two materials in a heterostructure is not flat. The layers penetrate into each other forming islands with a mean height and a correlation length. The correlation length is related to the size of the islands, and the mean height to their deviation from the flat interface. The treatment of interface roughness is fully empirical [39, 40]. For deriving the interface roughness scattering rate, we start by defining a position dependent deviation $\Delta(\mathbf{r})$ from the flat interface, where its autocorrelation function is empirically defined as a Gaussian

$$\left\langle\Delta\left(\mathbf{r}\right)\Delta\left(\mathbf{r}+\mathbf{d}\right)\right\rangle = \frac{1}{A}\int\Delta\left(\mathbf{r}\right)\Delta\left(\mathbf{r}+\mathbf{d}\right)\mathrm{d}^2\mathbf{r} = \Delta^2 e^{-\frac{|\mathbf{d}|^2}{\Lambda^2}}. \tag{2.3.51}$$

Furthermore, we assume that we have the interface at $z = z_0$. The perturbation potential is then the change of the barriers and wells by the amount $\Delta(\mathbf{r})$ defined as

$$V_{pert}^{int} = V_0 \left[H\left(z - z_0\right) - H\left(z - z_0 - \Delta\left(\mathbf{r}\right)\right)\right], \tag{2.3.52}$$

where V_0 is the band offset and $H(z)$ is the Heaviside function. Using Eq. (2.3.3), we calculate the matrix element between an initial state n and a final state m as

$$V_{mn}^{int}(z_0) = \frac{V_0}{A} \psi_n\left(z_0\right) \psi_m^*\left(z_0\right) \int \Delta\left(\mathbf{r}\right) \exp\left(i\mathbf{qr}\right) \mathrm{d}^2\mathbf{r}. \tag{2.3.53}$$

Here we have used, that $\psi_n(z_0) \approx \psi_n(z_0 + \Delta(\mathbf{r}))$. The total interface roughness squared matrix element is given by

$$\begin{aligned} \left|V_{nm}^{int,total}\right|^2 &= \frac{{V_0}^2}{A^2} \sum_{z_0} \left|\psi_n\left(z_0\right) \psi_m^*\left(z_0\right)\right|^2 \int\int \Delta\left(\mathbf{r}\right) \Delta\left(\mathbf{r}+\mathbf{d}\right) \mathrm{d}^2\mathbf{r} e^{i\mathbf{qd}} \mathrm{d}^2(\mathbf{r}+\mathbf{d}) = \\ &= \frac{{V_0}^2}{A} \sum_{z_0} \left|\psi_n\left(z_0\right) \psi_m^*\left(z_0\right)\right|^2 \Delta^2 \int\int r e^{-\frac{d^2}{\Lambda^2} + iqdCos(\theta)} \mathrm{d}\theta \mathrm{d}d = \\ &= \frac{2\pi {V_0}^2}{A} \sum_{z_0} \left|\psi_n\left(z_0\right) \psi_m^*\left(z_0\right)\right|^2 \Delta^2 \int r e^{-\frac{d^2}{\Lambda^2}} J_o(qd) \mathrm{d}d = \\ &= \frac{\pi {V_0}^2}{A} \sum_{z_0} \left|\psi_n\left(z_0\right) \psi_m^*\left(z_0\right)\right|^2 \Delta^2 \Lambda^2 e^{-\frac{1}{4}\Lambda^2 q^2}. \end{aligned} \tag{2.3.54}$$

The last term in the above equation is now used in Fermi's golden rule for static perturbations, i.e., Eq. (2.3.14) for deriving the scattering rate

$$W_{n\mathbf{k}m} = \frac{2\pi^2}{\hbar} \frac{{V_0}^2}{A} \sum_{z_0} \left|\psi_n\left(z_0\right) \psi_m^*\left(z_0\right)\right|^2 \Delta^2 \Lambda^2 \sum_{\mathbf{k}'} e^{-\frac{1}{4}\Lambda^2 q^2} \delta\left(E_m - E_n + \frac{\hbar^2 \left|\mathbf{k}'\right|^2}{2m_{||,m}} - \frac{\hbar^2 \left|\mathbf{k}\right|^2}{2m_{||,n}}\right). \tag{2.3.55}$$

Using Eq. (2.3.41), we get the scattering rate from an initial state $n\mathbf{k}$ to a final state m

$$W_{n\mathbf{k}m} = \frac{m_{||,m}}{2\hbar^3} \sum_{z_0} \left|\psi_n\left(z_0\right) \psi_m\left(z_0\right)\right|^2 {V_0}^2 \Delta^2 \Lambda^2 \int_0^{2\pi} e^{-\frac{1}{4}\Lambda^2 q(\theta)^2} \mathrm{d}\theta, \tag{2.3.56}$$

where q is defined by Eq. (2.3.42), with $\omega_{LO} = 0$.

2.3.7 Alloy scattering

In the case of ternary materials like InGaAs, InAlAs or AlGaAs, the lattice has not exactly a zinc-blende shape. Electrons interacting with the lattice are propagating in a distorted potential, which we want to include in this section. This is done by defining a ternary alloy system $\mathrm{A}_x\mathrm{B}_{1-x}\mathrm{C}$, from the binary materials AC and BC, where x represents the concentration of material A on a scale from 0 to 1. The potential in case of an alloy material can be defined as [41]

$$u(\mathbf{r}) = \sum_{\tau}^{\#A\,\text{atoms}} U_{\text{A}}(\mathbf{r}-\tau) + \sum_{\tau}^{\#B\,\text{atoms}} U_{\text{B}}(\mathbf{r}-\tau), \tag{2.3.57}$$

where U_A and U_B are the potentials of the binary materials AC and BC and τ is the position of the atomic sites. The above potential, u, is constructed as the sum of the potential of the two alloys [41]. We divide u into two parts U_1 and U_2. The first is the potential profile, where we define our basis solutions [41]

$$U_1(\mathbf{r}) = x \sum_{\tau}^{\#A\,\text{atoms}} U_{\text{A}}(\mathbf{r}-\tau) + (1-x) \sum_{\tau}^{\#B\,\text{atoms}} U_{\text{B}}(\mathbf{r}-\tau) \tag{2.3.58}$$

and the second component is the perturbation potential which will give the alloy scattering

$$U_2(\mathbf{r}) = (1-x) \sum^{\#A\,\text{atoms}} U_{\text{A}}(\mathbf{r}-\tau) + x \sum_{\tau}^{\#B\,\text{atoms}} U_{\text{B}}(\mathbf{r}-\tau). \tag{2.3.59}$$

We define the potential of a single atomic site as a δ-function multiplied by a constant lattice volume Ω_0 and the potential of materials AC or BC

$$U_{\text{A,B}}(\mathbf{r}-\tau) = \delta(\mathbf{r}-\mathbf{R}_{\text{A,B}})\Omega_0 U_{\text{A,B}}. \tag{2.3.60}$$

Here $\Omega_0 = a^3/4$ is the volume of the Wiegner-Seitz cell and a is the lattice constant. The choice of the 0-energy point is arbitrary, thus it is taken at

$$U_A + U_B = 0. \tag{2.3.61}$$

Substituting Eq. (2.3.60) into Eq. (2.3.59) we get for the difference-potential

$$U_2(\mathbf{r}) = \Omega_0(1-x)U_A \sum_{\mathbf{R}_A} \delta(\mathbf{r}-\mathbf{R}_A) + \Omega_0 x U_B \sum_{\mathbf{R}_B} \delta(\mathbf{r}-\mathbf{R}_B). \tag{2.3.62}$$

Defining the conduction band offset as $V_0 = U_A = -U_B$, we get the alloy scattering potential defined as [42]

$$\delta V_{eff}(\mathbf{r}) = \Omega_0 V_0 \left[\sum_{\mathbf{R}_\text{A}} (1-x)\delta(\mathbf{r}-\mathbf{R}_\text{A}) - \sum_{\mathbf{R}_\text{B}} x\delta(\mathbf{r}-\mathbf{R}_\text{B}) \right]. \tag{2.3.63}$$

The above potential was found by replacing the "difference potential" in [41] with δ-functions. We now calculate the matrix element for the potential in Eq. (2.3.63), with the envelope functions Eq. (2.3.3) where L_x and L_y are the planar dimensions of the alloy material, and $\psi_{n,m}$ is normalized to 1. The scattering matrix element is found to be [42]

$$V^a_{nm} = \frac{\Omega_0 V_0}{L_x L_y}\left[(1-x)\sum_{\mathbf{R}_\mathrm{A}}\psi^*_m(z_\mathrm{A})\psi_n(z_\mathrm{A})e^{i\mathbf{q}_{||}\mathbf{R}^{||}_\mathrm{A}} - x\sum_{\mathbf{R}_\mathrm{B}}\psi^*_m(z_\mathrm{B})\psi_n(z_\mathrm{B})e^{i\mathbf{q}_{||}\mathbf{R}^{||}_\mathrm{B}}\right]. \tag{2.3.64}$$

According to Fermi's golden rule in Eq. (2.3.14), the absolute-square of the matrix element V^a_{nm} must be calculated. The lattice vectors of the disorder sites $\mathbf{R}_\mathrm{A}$ and $\mathbf{R}_\mathrm{B}$ are defined as random variables if we model the alloys as a random material containing material A with x probability and material B with $1-x$ probability. The number of A material sites is N_A, the number of B material sites N_B and the absolute square for the above matrix element in terms of Kronecker deltas is

$$\begin{aligned}|V^a_{nm}|^2 = \left(\frac{\Omega_0 V_0}{L_x L_y}\right)^2 \sum_{\mathbf{R}}\sum_{\mathbf{R}'}\psi^*_m(z)\psi_n(z)\psi_m(z')\psi^*_n(z')e^{i\mathbf{q}_{||}(\mathbf{R}^{||}-\mathbf{R}'^{||})}\Bigg[(1-x)^2\sum_{\mathbf{R}_\mathrm{A}}\delta_{\mathbf{R},\mathbf{R}_\mathrm{A}}\sum_{\mathbf{R}_{\mathrm{A}'}}\delta_{\mathbf{R}',\mathbf{R}_{\mathrm{A}'}} \\ +x^2\sum_{\mathbf{R}_\mathrm{B}}\delta_{\mathbf{R},\mathbf{R}_\mathrm{B}}\sum_{\mathbf{R}_{\mathrm{B}'}}\delta_{\mathbf{R}',\mathbf{R}_{\mathrm{B}'}} - (1-x)x\sum_{\mathbf{R}_\mathrm{A}}\delta_{\mathbf{R},\mathbf{R}_\mathrm{A}}\sum_{\mathbf{R}_\mathrm{B}}\delta_{\mathbf{R}',\mathbf{R}_\mathrm{B}} - x(1-x)\sum_{\mathbf{R}_\mathrm{A}}\delta_{\mathbf{R}',\mathbf{R}_\mathrm{A}}\sum_{\mathbf{R}_\mathrm{B}}\delta_{\mathbf{R},\mathbf{R}_\mathrm{B}}\Bigg].\end{aligned} \tag{2.3.65}$$

In random alloy scattering the lattice sites are uncorrelated. This means that the expectation value of an atomic position can be written as

$$E\mathbf{R}^* E\mathbf{R} = E\left|\mathbf{R}\right|^2, \tag{2.3.66}$$

where

$$E\mathbf{R} = \frac{1}{n}\sum_{i=1}^{n}\mathbf{R}_i. \tag{2.3.67}$$

The total number of lattice sites N fulfills the relations

$$N = N_\mathrm{A} + N_\mathrm{B} = N_x N_y N_z. \tag{2.3.68}$$

Using the properties of uncorrelated random variables from Eq. (2.3.66) and the definition of the expectation value of samples from Eq. (2.3.67), we can reduce the terms of Eq. (2.3.65) to find

$$\begin{aligned}|V^a_{nm}|^2 = x(1-x)\left(\frac{\Omega_0 V_0}{L_x L_y}\right)^2 \sum_{\mathbf{R}}\sum_{\mathbf{R}'}\psi^*_m(z)\psi_n(z)\psi_m(z')\psi^*_n(z')e^{i\mathbf{q}_{||}(\mathbf{R}^{||}-\mathbf{R}'^{||})}\Bigg[N_\mathrm{B}\sum_{\mathbf{R}_\mathrm{A}}\delta_{\mathbf{R},\mathbf{R}_\mathrm{A}}\delta_{\mathbf{R}',\mathbf{R}_\mathrm{A}} \\ +N_\mathrm{A}\sum_{\mathbf{R}_\mathrm{B}}\delta_{\mathbf{R},\mathbf{R}_\mathrm{B}}\delta_{\mathbf{R}',\mathbf{R}_\mathrm{B}} - \sum_{\mathbf{R}_\mathrm{A}}\delta_{\mathbf{R},\mathbf{R}_\mathrm{A}}\sum_{\mathbf{R}_\mathrm{B}}\delta_{\mathbf{R}',\mathbf{R}_\mathrm{B}} - \sum_{\mathbf{R}_\mathrm{A}}\delta_{\mathbf{R}',\mathbf{R}_\mathrm{A}}\sum_{\mathbf{R}_\mathrm{B}}\delta_{\mathbf{R},\mathbf{R}_\mathrm{B}}\Bigg].\end{aligned} \tag{2.3.69}$$

Here we used that $N_\mathrm{A}/N \approx x$ and $N_\mathrm{B}/N \approx 1-x$ [43]. Since in III-V semiconductors the lattice constants have usually similar lengths, setting $\mathbf{R}_\mathrm{A} = \mathbf{R}_\mathrm{B}$ yields a good approximation and we have for the number of random terms in the infinite limit

$$\underset{N\to\infty}{lim}\frac{N(1-x)\delta_{\mathbf{R},\mathbf{R}'}\sum\limits_{\mathbf{R}_\mathrm{A}}\delta_{\mathbf{R},\mathbf{R}_\mathrm{A}}+Nx\delta_{\mathbf{R},\mathbf{R}'}\sum\limits_{\mathbf{R}_\mathrm{B}}\delta_{\mathbf{R},\mathbf{R}_\mathrm{B}}-\sum\limits_{\mathbf{R}_\mathrm{A}}\sum\limits_{\mathbf{R}_\mathrm{B}}\delta_{\mathbf{R},\mathbf{R}_\mathrm{A}}\delta_{\mathbf{R}',\mathbf{R}_\mathrm{B}}-\sum\limits_{\mathbf{R}_\mathrm{A}}\sum\limits_{\mathbf{R}_\mathrm{B}}\delta_{\mathbf{R},\mathbf{R}_\mathrm{B}}\delta_{\mathbf{R}',\mathbf{R}_\mathrm{A}}}{N}=\delta_{\mathbf{R},\mathbf{R}'}. \tag{2.3.70}$$

Replacing the above expression in Eq. (2.3.69), we get the average scattering potential [42]

$$\left\langle |V_{nm}|^2 \right\rangle_{\text{average}} \approx x(1-x)\frac{\Omega_0 V_0}{L_x L_y}\frac{L_z}{N_z}\sum_z |\psi_n(z)|^2\,|\psi_m(z)|^2\,. \tag{2.3.71}$$

We now recall Fermi's golden rule for static perturbations, Eq. (2.3.14), and apply it to the scattering potential from Eq. (2.3.71). The alloy scattering rate is then

$$W_{n\mathbf{k}m\mathbf{k}'} = \frac{2\pi}{\hbar}|V_{nm}|^2\,\delta\left(E_m(\mathbf{k}')-E_n(\mathbf{k})\right) = C\delta\left(E_m(\mathbf{k}')-E_n(\mathbf{k})\right), \tag{2.3.72}$$

where

$$C = x(1-x)\frac{\Omega_0 V_0^2}{L_x L_y}\int\limits_{\text{alloy}} |\psi_n(z)|^2\,|\psi_m(z)|^2\,\mathrm{d}z. \tag{2.3.73}$$

We integrate over the final $\mathbf{k}'$ state, to get the scattering rate from $n\mathbf{k}$ to m [42], yielding

$$\begin{aligned} W_{n\mathbf{k}m} &= \frac{L_x L_y}{4\pi^2}\frac{2\pi}{\hbar}C\int\int\delta\left(E_m - E_n + \frac{\hbar^2\mathbf{k}'}{2m_{||,m}} - \frac{\hbar^2\mathbf{k}}{2m_{||,n}}\right)\mathrm{d}\mathbf{k}' = \\ &= C\frac{L_x L_y}{2\pi}\frac{m_{||,m}}{\hbar^3}\int\int\delta\left(E_m - E_n + t - \frac{\hbar^2\mathbf{k}_n}{2m_n}\right)dt d\theta = L_x L_y\frac{m_m}{\hbar^3}C = \\ &= m_{||,m}\frac{\Omega_0}{\hbar^3}V_0^2 x(1-x)\int\limits_{\text{alloy}} |\psi_n(z)|^2\,|\psi_m(z)|^2\,\mathrm{d}z. \end{aligned} \tag{2.3.74}$$

The above scattering rate can be generalized for quantum cascade lasers to

$$W_{n\mathbf{k}m} = m_{||,m}\int\frac{\Omega_0(z)}{\hbar^3}V_0(z)^2 x(z)[1-x(z)]\,|\psi_n(z)|^2\,|\psi_m(z)|^2\,\mathrm{d}z. \tag{2.3.75}$$

Here we took all the variables into the integral, since they change with the different type of layers in the heterostructure. In the current EMC implementation, we use Eq. (2.3.75) for calculating the alloy scattering rate.

2.3.8 Electron-electron scattering

In addition to different scattering mechanisms related to the lattice or growth of the structures, electrons also scatter with other electrons. Electron-electron scattering is the main mechanism responsible for thermalization within the subbands. In the EMC simulation, e-e scattering is implemented as a two-body process [44, 45]. An electron in an initial state $|n\mathbf{k}\rangle$, i.e., subband n and in-plane wavevector $\mathbf{k}$, scatters to a final state $|m\mathbf{k}'\rangle$, accompanied by a transition of a second electron from a state $|i\mathbf{k}_0\rangle$ to

$|j\mathbf{k}'_0\rangle$. We derive e-e scattering by defining the perturbation [46, 45, 47] given by the Coulomb potential of an electron

$$V^{ee}_{pert} = \frac{e_0^2}{4\pi\varepsilon A}\frac{e^{-i(\mathbf{k_0}\mathbf{r}'+\mathbf{k}'_0\mathbf{r}')}}{\sqrt{|\mathbf{r}-\mathbf{r}'|^2+(z-z')^2}}\psi_j^*(z')\psi_i(z'). \tag{2.3.76}$$

The perturbation potential in Eq. (2.3.76) is given by the wavefunction of Eq. (2.3.3) for the initial and final state of the electron multiplied by the Coulomb potential. The perturbation potential from Eq. (2.3.76) has to be taken in the basis of the other electron to find the matrix element

$$V^{ee}_{nimj} = \frac{e_0^2}{4\pi\varepsilon A^2}\int\limits_{-\infty}^{\infty}\int\limits_{-\infty}^{\infty}\int\int\frac{e^{-i(\mathbf{k}\mathbf{r}+\mathbf{k_0}\mathbf{r}'-\mathbf{k}'\mathbf{r}-\mathbf{k}'_0\mathbf{r}')}}{\sqrt{|\mathbf{r}-\mathbf{r}'|^2+(z-z')^2}}\psi_n(z)\psi_i(z')\psi_m^*(z)\psi_j^*(z')\mathrm{d}\mathbf{r}\mathrm{d}\mathbf{r}'\mathrm{d}z\mathrm{d}z' \tag{2.3.77}$$

We use the substitutions $\mathbf{d}=\mathbf{r}-\mathbf{r}'$, $\mathbf{q}=\mathbf{k}-\mathbf{k}'$ and $\mathbf{q_0}=\mathbf{k_0}-\mathbf{k_0}'$ in Eq. (2.3.77) and calculate the matrix element V^{ee}_{nimj} as

$$\begin{aligned} V^{ee}_{nimj} &= \frac{e_0^2}{4\pi\varepsilon A^2}\int\limits_{-\infty}^{\infty}\int\limits_{-\infty}^{\infty}\psi_m^*(z)\psi_n(z)\psi_j^*(z')\psi_i(z')\int e^{-i\mathbf{r}'(\mathbf{q}+\mathbf{q_0})}\mathrm{d}\mathbf{r}'\int\frac{e^{-i\mathbf{q}\mathbf{d}}}{\sqrt{|\mathbf{d}|^2+(z-z')^2}}\mathrm{d}\mathbf{d}\mathrm{d}z\mathrm{d}z' = \\ &= \frac{e_0^2}{2\varepsilon A^2 q}F_{nimj}(q)\int e^{-i\mathbf{r}'(\mathbf{q}+\mathbf{q_0})}\mathrm{d}\mathbf{r}' = \frac{e^2}{2\varepsilon A q}F_{nimj}(q), \end{aligned} \tag{2.3.78}$$

where $F_{nimj}(q)$ represents the e-e scattering form factor defined by

$$F_{nimj}(q) = \int\limits_{-\infty}^{\infty}\int\limits_{-\infty}^{\infty}\psi_n(z)\psi_i(z')\psi_m^*(z)\psi_j^*(z')e^{-g|z-z'|}\mathrm{d}z\mathrm{d}z', \tag{2.3.79}$$

which is tabulated in our EMC tool and $g=|\mathbf{k}_0-\mathbf{k}|$. The square of the perturbation potential of Eq. (2.3.78) is

$$\left|V^{ee}_{nimj}\right|^2 = \frac{e_0^4\pi^2}{\varepsilon^2 A^3 q^2}\delta(\mathbf{k}+\mathbf{k_0}-\mathbf{k}'-\mathbf{k}'_0)\left|F_{nimj}(q)\right|^2, \tag{2.3.80}$$

where we kept the conservation of momentum in a δ-function form. We now apply Fermi's golden rule for static perturbations from Eq. (2.3.14) and get the scattering rate

$$W_{n\mathbf{k}m\mathbf{k}'i\mathbf{k_0}j\mathbf{k}'_0} = \frac{e_0^4 2\pi^3}{\hbar\varepsilon^2 A^3 q^2}\delta(\mathbf{k}+\mathbf{k_0}-\mathbf{k}'-\mathbf{k}'_0)\delta(E_{tot})\left|F_{ijmn}(q)\right|^2, \tag{2.3.81}$$

where

$$E_{tot} = \frac{\hbar^2(\mathbf{k}')^2}{2m_{||,m}} - \frac{\hbar^2(\mathbf{k})^2}{2m_{||,n}} + \frac{\hbar^2(\mathbf{k}'_0)^2}{2m_{||,j}} - \frac{\hbar^2(\mathbf{k_0})^2}{2m_{||,i}} + E_m - E_n + E_j - E_i. \tag{2.3.82}$$

We sum Eq. (2.3.81) over all the initial and final states of the second electron weighted by the distribution function of the initial state [11],

$$W_{n\mathbf{k}m\mathbf{k}'\mathbf{k}'_0} = \sum_{i,j,\mathbf{k_0}} f(\mathbf{k_0})W_{n\mathbf{k}m\mathbf{k}'i\mathbf{k_0}j\mathbf{k}'_0}. \tag{2.3.83}$$

Summing over the final wavevector $\mathbf{k_0'}$ of Eq. (2.3.83) and converting the sum to an integral, we get

$$W_{n\mathbf{k}m\mathbf{k'}} = \frac{e_0^4 \pi}{2\hbar\varepsilon^2 A^2 q^2} \sum_{i,j,\mathbf{k_0}} f_i(\mathbf{k_0})\delta(E_{tot}) \left|F_{nimj}(q)\right|^2 . \tag{2.3.84}$$

A further simplification of the above scattering rate cannot be performed analytically in the case of non-parabolic bands due to the different effective masses corresponding to the states m, n, j and i in Eq. (2.3.82). Furthermore the consideration of screening and spin would further complicate the derivation of the non-parabolic scattering rate. We will now discuss the case of e-e scattering for parabolic bands.

2.3.8.1 Scattering rate for parabolic band structure

Electron-electron scattering in case of parabolic bands assumes the same effective mass for each of the states. The energy conservation requires $E_{tot} = 0$ where E_{tot} defined by Eq. (2.3.82) simplifies to its parabolic case E^p_{tot} given by

$$E^p_{tot} = \frac{\hbar^2}{2m_{||}} \left[(\mathbf{k}')^2 - \mathbf{k}^2 + (\mathbf{k_0'})^2 - \mathbf{k_0}^2 \right] + E_m - E_n + E_j - E_i. \tag{2.3.85}$$

By using the substitutions $\mathbf{g} = \mathbf{k_0} - \mathbf{k}$ and $\mathbf{g}' = \mathbf{k_0'} - \mathbf{k}'$and $\mathbf{k} + \mathbf{k_0} - \mathbf{k}' - \mathbf{k_0'} = 0$ we can rewrite the above equation as

$$E^{p,s}_{tot} = \frac{\hbar^2}{4m_{||}} \left[\mathbf{g}^2 - (\mathbf{g}')^2 + \mathbf{g_0}^2 \right], \tag{2.3.86}$$

where $\mathbf{g}_0^2 = (E_m - E_n + E_j - E_i)4m_{||}/\hbar^2$. By writing the initial and final electron wavevectors in terms of $\mathbf{g}$ and $\mathbf{g}'$, we transform the energy conservation $E^p_{tot} = 0$ to the energy conservation containing the above substitutions $E^{p,s}_{tot} = 0$.

We find the scattering rate of the first electron from its initial state n and wavevector $\mathbf{k}$ to the final state m by summing Eq. (2.3.84) over $\mathbf{k}'$ and converting the sum to an integral,

$$\begin{aligned} W_{n\mathbf{k}m} &= \frac{e_0^4 \pi}{2\hbar\varepsilon^2 A^2 q^2} \sum_{i,j,\mathbf{k_0},\mathbf{k}'} f_i(\mathbf{k_0})\delta(E^p_{tot}) \left|F_{nimj}(q)\right|^2 \\ &= \frac{e_0^4}{8\pi\hbar\varepsilon^2 A} \sum_{i,j,\mathbf{k_0}} f_i(\mathbf{k_0}) \int \frac{\left|F_{nimj}(q)\right|^2}{q^2} \delta(E^p_{tot}) \mathrm{d}\mathbf{k}'. \end{aligned} \tag{2.3.87}$$

By using Eq. (2.3.86) and $\mathbf{g} = \mathbf{k_0} - \mathbf{k}$, $\mathbf{g}' = \mathbf{k_0'} - \mathbf{k}'$ and $\mathbf{k} + \mathbf{k_0} - \mathbf{k}' - \mathbf{k_0'} = 0$ the substitutions $-\mathrm{d}\mathbf{k_0'} = \mathrm{d}\mathbf{k}' = \mathrm{d}g_x' \mathrm{d}g_y'/4$ and $\mathbf{g} - \mathbf{g}' = 2\mathbf{q}$ can be made, and we can we rewrite Eq. (2.3.87) as

$$W_{n\mathbf{k}m} = \frac{e_0^4}{32\pi A\hbar\varepsilon^2} \sum_{i,j,\mathbf{k}_0} f_i\left(\mathbf{k}_0\right) \int \frac{\left|F_{nimj}(q)\right|^2}{q^2} \delta\left(E^{p,s}_{tot}\right) \mathrm{d}\mathbf{g}' = \frac{e_0^4 m_{||}}{16\pi A\hbar^3\varepsilon^2} \sum_{i,j,\mathbf{k}_0} f_i\left(\mathbf{k}_0\right) \int_0^{2\pi} \frac{\left|F_{nimj}(q)\right|^2}{q^2} \mathrm{d}\theta, \tag{2.3.88}$$

where

$$q = \frac{1}{2} \left[2g^2 - 2g\sqrt{g^2 + g_0^2}\cos(\theta) + g_0^2 \right]^{1/2} . \tag{2.3.89}$$

The above scattering rate does not include screening of electrons and their exchange interaction. For their modeling, Eq. (2.3.88) needs to be generalized [11] to

$$W_{n\mathbf{k}m} = \frac{m_{||}}{4\pi A\hbar^3} \sum_{i,j,\mathbf{k}_0} f_i\left(\mathbf{k}_0\right) \int_0^{2\pi} \left|M_{nimj}\left(q\right)\right|^2 \mathrm{d}\theta. \tag{2.3.90}$$

Different approaches with varying degrees of complexity exist to compute the transition matrix element M_{nimj} from the bare Coulomb matrix elements in Eq. (2.3.78). First, the screened Coulomb matrix elements $V^{ee,s}_{mnji}(q)$ are obtained from $V^{ee}_{mnji}\left(q\right)$ by applying a more or less sophisticated screening model. In the random phase approximation (RPA), they are found by solving the equation system [48]

$$V^{ee,s}_{nimj} = V^{ee}_{nimj} + \sum_{ab} V^{\mathrm{ee}}_{namb}\Pi_{ab}V^{ee,\mathrm{s}}_{aibj}. \tag{2.3.91}$$

Here, $\Pi_{ab}\left(q\right)$ is the polarizability tensor, given in the long wavelength limit ($q \rightarrow 0$) by

$$\Pi_{ab} = \begin{cases} \frac{n_{2\mathrm{D},a}-n_{2\mathrm{D},b}}{E_a-E_b}, & a \neq b, \\ -\frac{m_{||}}{\pi\hbar^2} f_a\left(0\right), & a = b. \end{cases} \tag{2.3.92}$$

Here $n_{2D,a}$ is the sheet doping density for the state a. For collisions of electrons with parallel spin, interference occurs between $V^{ee,s}_{nimj}$ and the 'exchange' matrix element $V^{ee,s}_{nijm}$ [49]. Accounting for this exchange effect, the magnitude squared of the transition matrix element M_{nimj} is then given by [45, 49]

$$\begin{aligned} \left|M_{nimj}\right|^2 = {} & \frac{p_a}{2}\left[\left|V^{\mathrm{ee,s}}_{nimj}\left(q\right)\right|^2 + \left|V^{ee,\mathrm{s}}_{nijm}\left(q'\right)\right|^2\right] \\ & + \frac{p_p}{2}\left|V^{\mathrm{ee,s}}_{nimj}\left(q\right) - V^{ee,\mathrm{s}}_{nijm}\left(q'\right)\right|^2, \end{aligned} \tag{2.3.93}$$

where $p_a = p_p = 1/2$ are the probabilities for antiparallel and parallel spin collisions, respectively, and

$$q' = \frac{1}{2}\left[2g^2 + g_0^2 + 2g\left(g^2 + g_0^2\right)^{1/2}\cos(\theta)\right]^{1/2}, \tag{2.3.94}$$

with $g = |\mathbf{g}|$.

Commonly, simplified screening models are used to avoid the numerical load associated with solving Eq. (2.3.91) [31, 50]. Furthermore, often the exchange effect is neglected when calculating M_{nimj} [49].

2.3.8.2 Non-parabolic band structure

Electron-electron interaction in EMC is implemented with the inclusion of non-parabolic bands. Its inclusion is based on the work of Bonno and Thobel [47]. They derive non-parabolicity for the case of two body processes, based on the non-parabolic density of states. Generally, the determination of the electron final wavevector from the scattering rate Eq. (2.3.84) and energy conservation Eq. (2.3.82) is possible only numerically. If one assumes that the states have different effective masses, however a constant effective mass within a subband, we can a derive an analytical solution. The derivation of e-e scattering rates in this case requires several transformations and is quite lengthy, thus we restrict ourselves to the discussion of the energy conservation, which requires that

$$\begin{aligned}
x &= k_{ix} + k_{nx}, \\
y &= k_{iy} + k_{ny}, \\
(g')^2 &= \frac{4}{\frac{1}{m_{||,j}} + \frac{1}{m_{||,m}}} \left[\frac{2}{\hbar^2} (E_i + E_n - E_j - E_m) + \frac{1}{m_{||,i}} k_i^2 + \frac{1}{m_{||,n}} k_n^2 \right] - x^2 - y^2,
\end{aligned} \tag{2.3.95}$$

where g' was defined in Section 2.3.8.1. We can observe, that by setting the effective masses equal, we get back the parabolic case of Eq. (2.3.86). The new definition of energy conservation can be used to derive the non-parabolic scattering rates using the same notations as in Section 2.3.8.1. The determination of the final wavevector $\mathbf{g}'$ is based on

$$\begin{aligned}
g'_x &= \frac{g_y}{g} h_x + \frac{g_x}{g} h_y, \\
g'_y &= -\frac{g_x}{g} h_x + \frac{g_y}{g} h_y,
\end{aligned} \tag{2.3.96}$$

where $h_x = h_x(\mathbf{k}_n, \mathbf{k}_i)$, $h_y = h_y(\mathbf{k}_n, \mathbf{k}_i)$ are functions of the initial wavevectors for the first and second electron and were determined analytically.

2.4 Material gain

For analyzing the lasing performance, the material gain is an important quantity and will be derived in this section. The gain spectrum of the simulated QCLs can be compared to luminescence measurements and can give an estimate for the efficiency of the devices. QCLs are usually stacked structures, with layer thicknesses in the few nm range where the alternating barriers and wells are grown. Since the wavelengths are much smaller than the barrier and well thicknesses in our superlattice structures, a uniform dielectric constant within the material can be assumed [51]. The QCL operates in TM mode [52]. For this case, the effective dielectric constant ε_m in the gain medium is given by [51, 53]

$$\frac{1}{\varepsilon_m} = \frac{t_b/\varepsilon_b + t_w/\varepsilon_w}{t_b + t_w}. \tag{2.4.1}$$

Here, the t_b and t_w are the total thickness of the barriers and wells in one period, respectively. The ε_w and ε_b stand for the dielectric constants in the wells and barriers. For our simulations, we have used the effective values provided by the corresponding experimental groups.

For GaAs-based QCLs in this thesis we have used an effective refractive index $n_0 = \sqrt{\varepsilon_m} = 3.8$, measured from the mode spacing of the TM modes in the laser resonator [25, 54]. This value practically does not change for the different THz QCL designs considered in this thesis, since they are all based on metal-metal waveguides with a 10 μm thick active region. Furthermore, the refractive indices of GaAs and $\mathrm{Al}_{0.15}\mathrm{Ga}_{0.85}\mathrm{As}$ have very similar values. The frequency dependence of the dielectric constants can be interpolated by combining Eqs. (2.3.28) and (2.3.29). Using the corresponding material parameters, it is then found that the refractive indices for GaAs and $\mathrm{Al}_{0.15}\mathrm{Ga}_{0.85}\mathrm{As}$ differ only by 3-4% throughout the THz regime.

Furthermore, in this thesis two types of mid-infrared InGaAs-based structures are investigated. For the high power QCL [7], an effective refractive index value of $n_0 = 3.24$ has been used, which contains the influence of both the active region and the InP claddings [55]. For the short-injector QCL emitting at 8μm [56], the same value has been taken [57].

The relations for the generalized optical power per unit volume in case of a gain medium [58] are

$$P_V = (n^n W^a_{nm} - n^m W^e_{nm})\hbar\omega_q, \tag{2.4.2}$$

where W^a_{nm} is the stimulated single-electron absorption rate from the initial state n to the final state m and W^e_{nm} is the stimulated single-electron emission rate from the initial state n to the final state m. The mode frequency is denoted by ω_l while n^n and n^m are the volume densities of the population in states n and m. The volume densities generally are not in steady state, but change in time, as the gain gets saturated. Fermi's golden rule can be used to determine the absorption and emission rates [58]

$$\begin{aligned} W^a_{mn} &= \frac{2\pi}{\hbar}\left|\frac{e_0}{m_z^*}\mathbf{A}^l_0 \langle\hat{\mathbf{p}}\rangle_{nm}\right|^2 \delta(E_m - E_n + \hbar\omega_l) \\ W^e_{mn} &= \frac{2\pi}{\hbar}\left|\frac{e_0}{m_z^*}\mathbf{A}^l_0 \langle\hat{\mathbf{p}}\rangle_{nm}\right|^2 \delta(E_n - E_m - \hbar\omega_l). \end{aligned} \tag{2.4.3}$$

Here $\mathbf{A}^l_0$ is the vector potential of the optical field in the lth mode and $\langle\hat{\mathbf{p}}\rangle_{nm}$ is the momentum of the electron. We can also see from Eq. (2.4.3), that the stimulated emission and absorption rates are equal. Usually in a rectangular cavity we have multiple propagating modes, represented here by the modal index l. We now proceed by deriving the spectral gain for a single mode and drop the mode index l. The wave function of the electron for the total system in Eq. (2.3.3) is used here and the propagation direction is assumed to be z. For finding the stimulated emission rate, we must first find the matrix element for the momentum operator $\hat{\mathbf{p}}_{nm} = -i\hbar\nabla$ using Eq. (2.3.3) for the basis functions

$$\langle\hat{\mathbf{p}}\rangle_{nm} = \begin{bmatrix} \delta_{n_x,m_x}\delta_{n_y,m_y}\delta_{n_z,m_z}\hbar k_{n_x} \\ \delta_{n_x,m_x}\delta_{n_y,m_y}\delta_{n_z,m_z}\hbar k_{n_y} \\ \delta_{n_x,m_x}\delta_{n_y,m_y}p^z_{n_z,m_z} \end{bmatrix}. \tag{2.4.4}$$

Here, δ_{n_z,m_z} is the Kronecker symbol and follows from the orthogonality of the wavefunctions, while n_x,

n_y and n_z are the initial state in the x, y and z directions, respectively. The rates from Eq. (2.4.3), i.e., the stimulated absorption and emission rates are equal for a single electron so it is enough to calculate the stimulated emission rate, which is written as

$$W^e_{mn} = \frac{2\pi}{\hbar}\left(\frac{e}{m^*_z}\right)^2 \delta_{x_n,x_m}\delta_{y_n,y_m}\left[A^0_x\hbar k_{n_x}\delta_{n_z,m_z} + A^0_y\hbar k_{n_y}\delta_{n_z,m_z} + A^0_z p^z_{n_z,m_z}\right]^2 \delta(E_n - E_m + \hbar\omega). \quad (2.4.5)$$

Due to interaction with photons, the initial and final state of the electron is never the same, so we always have the case of $n_z \neq m_z$ and Eq. (2.4.5) simplifies to

$$W^e_{mn} = \frac{2\pi}{\hbar}\left|\frac{e}{m^*_z}A^0_z p^z_{n_z,m_z}\right|^2 \delta_{n_x,m_x}\delta_{n_y,m_y}\delta(E_m - E_n + \hbar\omega). \quad (2.4.6)$$

We use Eq. (2.4.2) together with the above equation to determine the dissipated (or gained) power per unit volume

$$P_V = 2\pi(n^n - n^m)\omega\left|\frac{e}{m^*_z}A^0_z p^z_{n_z,m_z}\right|^2 \delta_{n_x,m_x}\delta_{n_y,m_y}\delta(E_m - E_n + \hbar\omega). \quad (2.4.7)$$

The time-averaged dissipated power per unit volume (effective power) in case of a monochromatic field can be additionally determined with the expression [59]

$$P_V = 2\sigma\left(-A^0_z\omega\right)^2, \quad (2.4.8)$$

which is a direct consequence of Maxwell's equations. Here σ is the conductivity of the medium. Usually Eq. (2.4.8) is used to calculate the power dissipation of an electromagnetic wave in a passive medium. If we have positive gain, then we have a negative conductivity, meaning that $g(\omega) = -\sigma Z$, where Z is the waveimpedance in the material. Now we can calculate the gain as

$$g(\omega) = -\frac{P_V}{2\left(-A^0_z\omega\right)^2}Z = \pi(n^m - n^n)\frac{1}{\omega}\left|\frac{e}{m^*_z}p^z_{n_z,m_z}\right|^2 Z\delta_{n_x,m_x}\delta_{n_y,m_y}\delta(E_m - E_n + \hbar\omega). \quad (2.4.9)$$

The oscillator strength

$$f^o_{mn} = \frac{2}{m^*_z\omega\hbar}\left|p^z_{n_z,m_z}\right|^2 \quad (2.4.10)$$

can be used to simplify our formula and Eq. (2.4.9) is rewritten as

$$g(\omega) = \frac{\pi}{2m^*_z}(n^m - n^n)e^2 Z f^o_{mn}\delta_{n_x,m_x}\delta_{n_y,m_y}\delta(\omega_{mn} - \omega). \quad (2.4.11)$$

Because of dissipative processes, the stimulated-emission rate always has a finite linewidth, so the δ-function is replaced by a Lorentzian-line [12]

$$\delta(\omega_{mn} - \omega) \mapsto \rho(\omega) = \frac{1}{2\pi}\frac{\Delta\omega}{(\omega - \omega_{mn})^2 + \left(\frac{\Delta\omega}{2}\right)^2}. \quad (2.4.12)$$

The Lorentzian linewidth can be related to the spontaneous emission time, and to the dissipation times of the initial and final states, as [52]

$$\Delta\omega = \frac{1}{T_n} + \frac{1}{T_m} + \frac{2}{T_{\text{dephasing}}}. \tag{2.4.13}$$

Here T_n^{-1} and T_m^{-1} are the out-scattering rates from the initial and final state, while $T_{\text{dephasing}}^{-1}$ is the broadening due to non-diagonal effects, that are neglected in EMC. We use in our framework the phenomenology of the finite linewidth to calculate the gain and we also assume that $n_x = m_x$, $n_y = m_y$, i.e., momentum is conserved (neglecting the momentum of the photon). For this case, we get the material gain

$$g(\omega) = \frac{\pi f_{mn}^o}{2m_z^*}(n^m - n^n)e_0^2 Z\rho(\omega), \tag{2.4.14}$$

which is also used in a slightly different form in our EMC method for calculating gain spectra. The peak gain is

$$g(\omega_{n_z m_z}) = \frac{f_{mn}^o}{m_{||,m}}(n^m - n^n)e_0^2 \frac{Z}{\Delta\omega}. \tag{2.4.15}$$

We note, that in EMC, we use a generalized form of the scattering rates in Eq. (2.4.3) and sum over the Lorentzians to account for several transitions contributing to the spectral gain. For further details of the photon scattering rates in EMC, we refer to Section 6.3.

2.5 Monte-Carlo algorithm

The EMC algorithm provides the solution of the Boltzmann transport Eq. (2.0.3) by means of a statistical average over carriers to find the distribution function. EMC can provide a straightforward modeling for various mechanisms like

- scattering rate between levels
- phonon distribution
- current density
- parasitic current between levels
- electroluminescence
- gain and gain bandwidth
- inversion
- injection efficiency
- output power

- electron temperature
- dwell time
- occupations
- electron distribution
- influence of various scattering rates on all the above.

Our solver considers a predefined number of electrons (a standard of 10000), and calculates the path of each electron through the device in time. The microscopic nature of this approach offers the straightforward extraction and implementation of new effects.

We now have all the ingredients to discuss the algorithm for solving the Boltzmann equation. The EMC program is based on the basis functions in the pre-defined heterostructure, which are found by the Schrödinger solver discussed in Section 2.1, coupled to a Poisson solver, to account for the redistribution of charges given by the doping in the structure. For solving the Poisson equation, one must know the occupations of the different levels, however at the first run this is not possible, thus we must assume some occupations. If the band-bending is small, this assumption can be accurate enough, like in the case of resonant phonon depopulation THz QCLs, or short injector mid-infrared structures. However, for bound-to continuum QCLs shown in the next section, so called self-self consistent simulations should be performed since the doping in these structures highly influences the tilt of the conduction band. For bound-to continuum QCLs, after running EMC, the occupations are used in the Poisson solver to calculate again the band bending. This is done until the conduction band profile does not change. Such self-self consistent simulations are critical for finding the correct alignment of the states, since those are influenced by the change of the conduction band profile which largely affects the whole dynamics in these structures. For moderately doped structures, however, avoiding self-self consistent approaches can save a lot of simulation time while results are still accurate enough. In this case we assume a Fermi distribution [27] for the occupation of the states or sometimes we can even assume equal occupations for each state. The use of a Fermi distribution is favorable for calculating thermally occupied subbands for QCLs with low doping. We have also used equal occupations in the states, and especially in resonant phonon depopulation structures, where the doping is very small, the band bending was described well-enough by this approach.

The next step after finding the wavefunctions by the SP solver is to execute the EMC program. The algorithm starts by importing the structural parameters like amount and position of the doping, barrier-well interface coordinates, temperature, material types and their concentration in the wells and barriers (for alloy scattering), band offset, dielectric constants and roughness parameters. These are all needed for the evaluation of the scattering rates. Additionally, the wavefunctions and non-parabolic average in-plane effective masses for the different levels, which are read in from the SP output files. The EMC program has

electron-electron scattering	1
LO-phonon absorption	2
LO-phonon emission	3
spontaneous photon emission	4
alloy disorder	5
acoustic phonons	6
impurities	7
interface roughness	8
stimulated photon emission/absorption	9

Table 2.1: Scattering rate indices in the code

also built-in material constants like the lattice constant, phonon energy, sound velocity, material density and alloy scattering potential of the different materials (GaAs, SiGe, or InGaAs).

The calculation of the different form factors is the next step. All the scattering mechanisms have form factor calculating routines which are needed for the evaluation of the scattering rates. The most time consuming evaluation is the calculation of the electron-electron form factors, since there we have to integrate over the wavefunctions of the initial and final state of the first and second electron. The form factors are written in files for their later evaluation if needed or for a second run if we want to

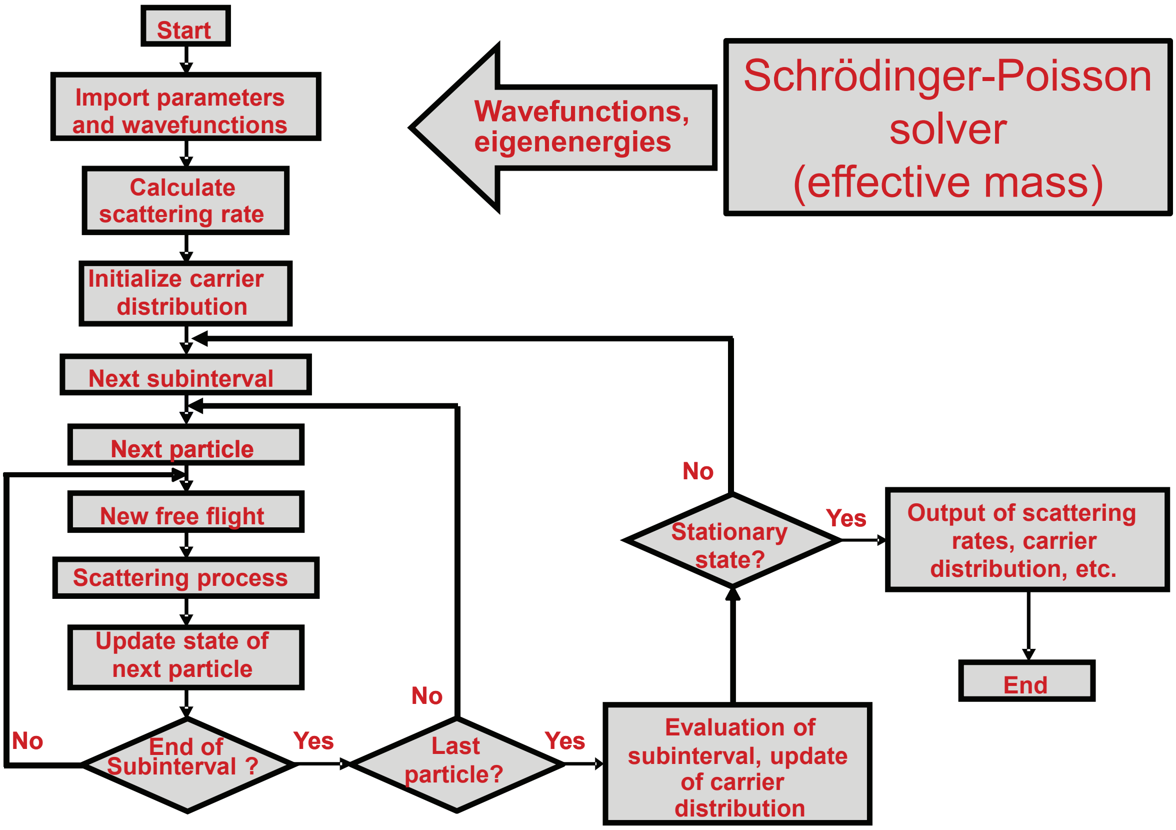
Start
Import parameters and wavefunctions
Calculate scattering rate
Initialize carrier distribution
Next subinterval
Next particle
New free flight
Scattering process
Update state of next particle
End of Subinterval ?
No
Yes
Last particle?
No
Yes
Evaluation of subinterval, update of carrier distribution
Stationary state?
No
Yes
Output of scattering rates, carrier distribution, etc.
End
Wavefunctions, eigenenergies
Schrödinger-Poisson solver (effective mass)

Figure 2.5.1: The schematic diagram of the Monte-Carlo algorithm

see the results with different parameters that do not change the wavefunctions. The scattering rates are calculated based on the form factors and stored. The tabulation is performed for each initial state, initial wavevector and final state. Each scattering rate has an index in the EMC code shown in Table 2.1. For stimulated photon processes we need only one index, since we can distinguish between emission and absorption by comparing the energies of the initial and final states. If the initial level is higher in energy than the final one we have emission, otherwise absorption. A three dimensional matrix is used to store the scattering rates as a function of the initial and final state, and the scattering type of the transition. The corresponding matrix element is incremented for each scattering event occurring. After convergence this matrix will contain the count of the scattering events of a specific type, between two given levels evaluated on a random basis.

Since we are interested in a steady state solution, the simulation time has to be chosen in such a way that the carrier distributions do not change much towards the end of the simulation. Furthermore the carrier distributions should be initialized in a manner which is not very improbable. Hence, the carriers are initialized by assuming a Fermi distribution in the case of the first run. If self-self consistent simulations are performed, the carrier distributions are read in from the previous run.

The Monte-Carlo algorithm has three basic loops. The external loop is for the predefined time step which divides the simulation into time-subintervals. The second loop, which is inside the time loop is the electron loop, which goes from the first to the last simulated electron out of the 10000 simulated electrons. The innermost loop is the scattering and free-flight loop. These are illustrated in the schematic of the EMC algorithm in Fig. 2.5.1.

The program computes the solution as follows. After the initializations and calculations of the scattering rates, the time-dependent simulation starts. In each time-interval we take the carriers sequentially and each carrier undergoes a free flight and then scattering. The scattering type and final state of each electron are chosen completely random, based on the tabulated scattering rates. After the choice of the scattering type and final state, the scattering angle, i.e., the angle $\angle\mathbf{k},\mathbf{k}'$ is chosen again randomly, to determine the complete final wavevector, $\mathbf{k}'$ of the electron. Once the wavevector is determined we apply the Pauli exclusion principle, to check if the final state is available based on its occupation probability. If the scattering mechanism is rejected, a new free flight is performed and we choose a new scattering process as illustrated in Fig. 2.5.1. We do this for every particle until we reach the last one. Then we are in the outer loop again and we can average and statistically extract the current and carrier distribution. The program does not stop when these have converged, it only stops when it has reached the end the of the pre-defined simulation time. Hence, the simulation time must be long enough to reach a stationary state. After the steady state solution has been reached we can postprocess our data and extract the required observables like current, carrier distributions, gain etc.

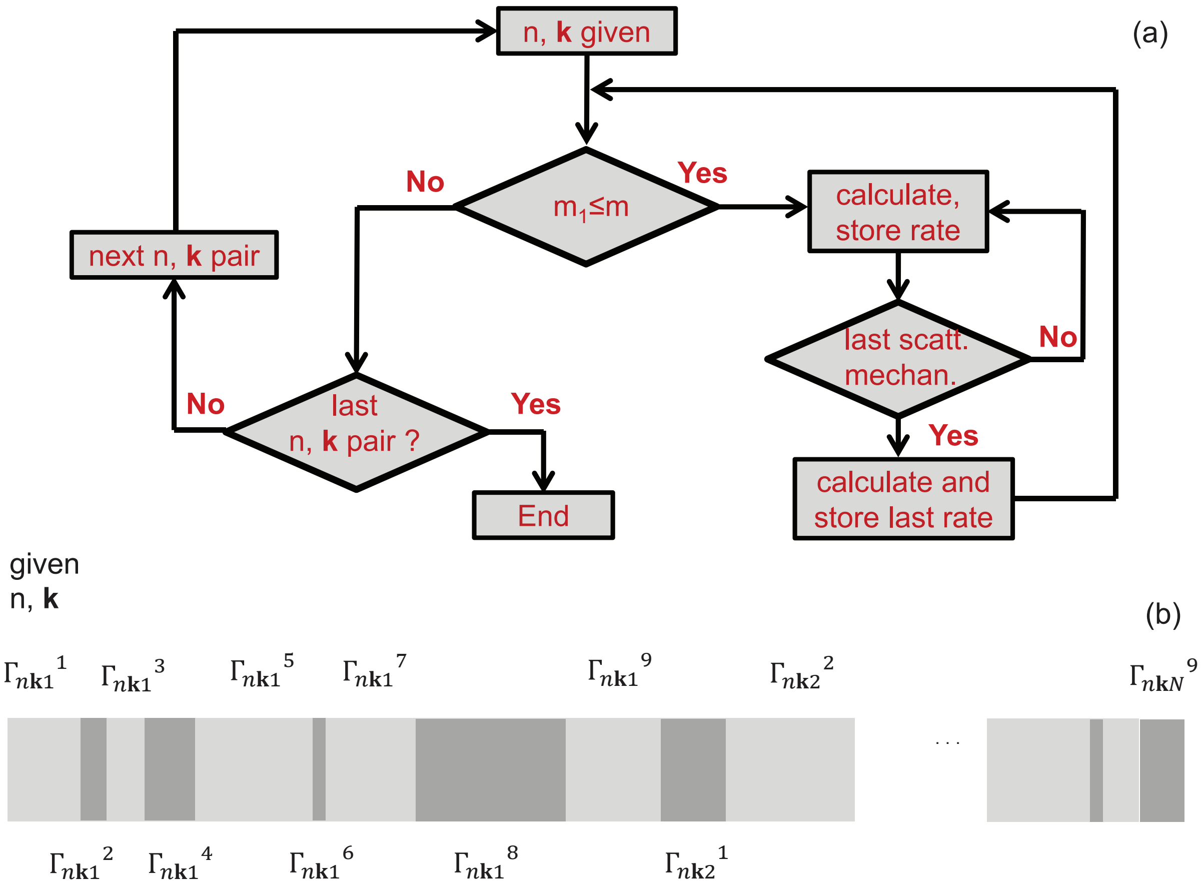
(a)
n, k given
m₁≤m
Yes
No
calculate, store rate
last scatt. mechan.
No
Yes
calculate and store last rate
next n, k pair
last n, k pair ?
No
Yes
End
given n, k
(b)
$\Gamma_{n\mathbf{k}1}{}^1$
$\Gamma_{n\mathbf{k}1}{}^3$
$\Gamma_{n\mathbf{k}1}{}^5$
$\Gamma_{n\mathbf{k}1}{}^7$
$\Gamma_{n\mathbf{k}1}{}^9$
$\Gamma_{n\mathbf{k}2}{}^2$
$\Gamma_{n\mathbf{k}N}{}^9$
...
$\Gamma_{n\mathbf{k}1}{}^2$
$\Gamma_{n\mathbf{k}1}{}^4$
$\Gamma_{n\mathbf{k}1}{}^6$
$\Gamma_{n\mathbf{k}1}{}^8$
$\Gamma_{n\mathbf{k}2}{}^1$

Figure 2.5.2: Scattering rate tabulation, for choosing the final state and scattering type.

2.5.1 Choice of the scattering mechanism and final state

The choice of scattering from the initial electron state to a final state as well as the type of scattering mechanism are randomly performed in EMC. The probability for scattering is calculated based on the scattering rates in Sections 2.3.4, 2.3.5, 2.3.6 and 2.3.8. We calculate scattering rates of the form $W^j_{n\mathbf{k}m}$, where j is the scattering type index defined in Table 2.1, n the initial state, $\mathbf{k}$ the initial in-plane wavevector and m the final state. These rates will define an interval in Fig. 2.5.2 (b) which is proportional to the probability of the scattering event. All the transition rates from the initial state $n\mathbf{k}$ are stored and calculated based on the flowchart in Fig. 2.5.2 (a). The random choice of the scattering type is based on the interval shown in Fig. 2.5.2 (b), which is generated by the flowchart that uses the expression $\Gamma^j_{n\mathbf{k}m} = \sum\limits_{m_1=1}^{m-1}\sum\limits_{j_1=1}^{9} W^{j_1}_{n\mathbf{k}m_1} + \sum\limits_{j_1=1}^{j} W^{j_1}_{n\mathbf{k}m}$ for every j and m. In EMC we also define a global maximum of the scattering rates $\Gamma_{max} = \max\limits_{n,\mathbf{k}} \Gamma^9_{n\mathbf{k}N}$ which is needed for the random choice of scattering type and final state. We observe that all the scattering in the device must be smaller then Γ_{max}. Furthermore, the choice is performed as follows:

- We generate a random number r on the $(0,1)$ interval and from this a random scattering rate $r\Gamma_{max}$

- If $r\Gamma_{max} < W^{9}_{n\mathbf{k}N}$ then we look for the case $W^{j}_{n\mathbf{k}m} < r\Gamma_{max}$ by incrementing m and j monotonically. If we find the case when for a given j and m $W^{j}_{n\mathbf{k}m} < r\Gamma_{max}$, however either $W^{j+1}_{n\mathbf{k}m} > r\Gamma_{max}$ or $W^{1}_{n\mathbf{k}m+1} > r\Gamma_{max}$ then the scattering type will be j and the final state will be m.
- If $r\Gamma_{max} \geq W^{9}_{n\mathbf{k}N}$, then self scattering occurs, i.e., the electron keeps its initial state and momentum.

In summary the random variable $r\Gamma_{max}$ either points into the interval shown in Fig. 2.5.2 (b), hence we know the scattering type and final state, or points outside this interval, and then self-scattering occurs, i.e., the state and momentum of the electron does not change.

Even when the choice of the scattering type and final state was performed, self scattering can still arise from rejection of a configuration involving an initial state and wavevector $n\mathbf{k}$, a final state m and a scattering mechanism. This can happen since there can be configurations when the transition of $n\mathbf{k} \to m$ is not allowed due to energy conservation, screening or Pauli's exclusion principle. Energy cannot be conserved for example in the case of LO-phonons when the level spacing is too small for a phonon emission, or in the case of impurities when the initial state energy is lower than the final state energy etc.

2.5.2 Choice of the final angle after scattering

We have discussed the choice of the scattering mechanism and the final state based on their probabilities. After scattering occurs from the initial state and wavevector $n\mathbf{k}$ to the final state m, we need to choose the scattering angle of the electron. This is needed for finding its complete final wavevector. The electron kinetic energy after scattering is already known due to energy conservation, thus by determining the scattering angle its full wavevector can be computed. The scattering angle is chosen randomly, based on the form-factors of the given scattering mechanism. We discuss the choice of the scattering angle for LO-phonon scattering. For the other mechanisms the choice is done in a similar manner. Energy conservation for each scattering mechanism, requires that Eq. (2.3.42) holds (for static perturbations, e.g., impurity, alloy, interface roughness scattering, $\omega_{LO} = 0$). Thus we can relate a randomly chosen angle $0 \leq \theta_r \leq 2\pi$ to a momentum exchange of the amount $q(\theta_r)$. If the q-dependent terms in the scattering rates, for example $J(q(\theta_r))$ in Eq. (2.3.39) are larger than $r_1 \times \max\{J(q)\}$, where r_1 is a random number between 0 and 1, then this randomly chosen scattering angle is accepted. Otherwise a new scattering angle is generated and a new random number r_1. After the scattering angle is calculated, we have the complete information on the final state wavevector.

2.5.3 Pauli's exclusion principle

Electrons that scatter go from an initial state n and wavevector $\mathbf{k}$ to a final state m. If the final state is unoccupied, as in most of the cases with low carrier concentrations, the scattering can take place. For higher carrier densities, however, there is a considerable probability that in the final state there is an electron, meaning that the exclusion principle should be taken into account. If we denote the number of simulated electrons in EMC as N_s, then we can define an effective area $A_{eff} = N_s/n_{2D}$ where n_{2D} is the sheet density, which is known from the amount of doping. The next step is to define a kinetic energy grid with grid spacing Δk_x and Δk_y. Every cell can contain at most $n_c = A_{eff}\Delta k_x \Delta k_y/4\pi^2$ electrons from the total number of N_s. After each scattering event, both k_x and k_y change for the scattered electron. This means that if we define a 2D grid with Δk_x and Δk_y grid spacing, we can count the number of electrons in each cell and subtract an electron from the cell corresponding to the initial state $n\mathbf{k}$ in the grid and add this electron to the cell of the final state $m\mathbf{k}'$ in the grid. Here, $\mathbf{k}$ is the wavevector before scattering, and $\mathbf{k}'$ is the final wavevector. However, there is a probability that the final cell is occupied, especially if n_{2D} is high. The exclusion principle is implemented as follows. The variable that counts the electrons over the kinetic grid discussed above is $f_d^e(k_x, k_y, n)$, where n represents the state of the electron.

After a scattering mechanism is chosen and the corresponding final state and scattering angle is determined, we must test if the final state is unoccupied. This is done by randomly generating a number r between 0 and 1 and testing the inequality $f_d^e(k_x', k_y', m)/n_c < r$. If it holds, the number of electrons is increased by one in the final state ($f_d^e(k_x', k_y', n) \rightarrow f_d^e(k_x', k_y', m) + 1$) and decreased by one in the initial state ($f_d^e(k_x, k_y, n) \rightarrow f_d^e(k_x, k_y, n) - 1$). If the inequality does not hold, then it means that the state is already occupied and we reject the transition to the final state m, and self-scattering occurs.

2.6 Electron-electron scattering and space-charge effects in quantum cascade lasers

We present some examples for the use of the theory presented in Section 2.3.8, namely for the influence of e-e scattering and space-charge effects on bound to continuum (BTC) and resonant-phonon depopulation quantum cascade lasers. For the case of e-e scattering, screening as well as exchange effects will be discussed. However, we first present some typical quantum cascade designs and briefly explain their working principles.

2.6.1 Quantum cascade lasers

Quantum cascade lasers are typically built from the $\mathrm{In}_x\mathrm{Ga}_{1-x}\mathrm{As}/\mathrm{In}_y\mathrm{Al}_{1-y}\mathrm{As}$ material system, mainly for the mid-infrared, or $\mathrm{GaAs}/\mathrm{Al}_x\mathrm{Ga}_{1-x}\mathrm{As}$ material system for the THz regime. They are composed of a repeated sequence of alternating epitaxial layers grown by molecular beam epitaxy (MBE) or metal-organic chemical vapor deposition (MOCVD). The alternating layer materials have different bandgaps, thus they form quantum wells and barriers in the conduction band. The layer thicknesses and material composition should be designed in such a way, at a so-called design bias, that population inversion occurs between two levels which will be the upper and the lower laser level. We present two different design approaches to reach population inversion in a quantum cascade laser:

- Resonant phonon (RP) depopulation structures, see Fig. 2.5.3 (a). These QCLs are designed in such a way, that they have an upper and lower laser level, marked by the bold solid lines, and one or several upper and lower phonon levels which have a spacing of one LO-phonon energy (36 meV in GaAs). In these structures, the lower laser level is aligned with the upper phonon level for a fast extraction of the electrons by means of LO-phonon scattering to the lower phonon level and from there electrons get re-injected into the upper laser level of the next period. In other words, the lower laser level gets depopulated by LO-phonon scattering and inversion is achieved. An example for a resonant phonon depopulation QCLs can be found in Fig. 2.5.3 (a).

- Bound to continuum (BTC) transitions, in Fig. 2.5.3 (b). In these designs, the lasing transition occurs from an upper laser level (bold solid line) to the miniband below. The miniband, or 'continuum' is formed by many closely spaced energetic states. These structures have several quantum wells in a period, since the miniband must be formed from many states. The lower laser level is the highest state of the miniband in the energy period, which contains only a few electrons. This level gets depleted due to the closely lying states in the miniband, which are strongly coupled. Te

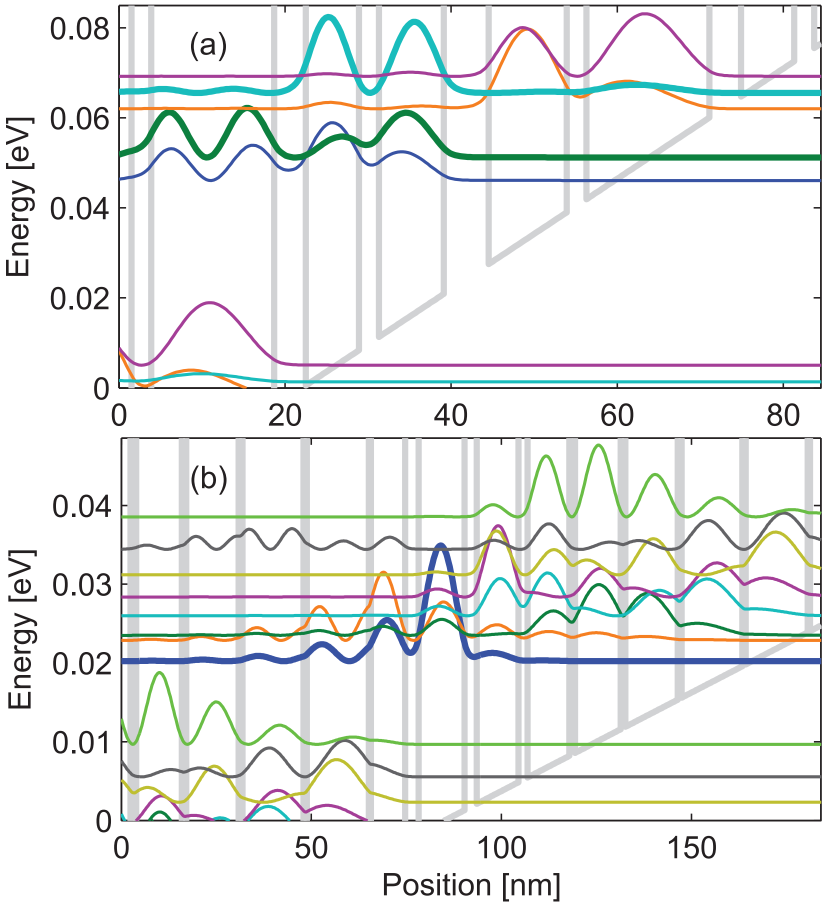

Figure 2.5.3: (a) Resonant phonon depopulation and (b) bound to continuum quantum cascade lasers.

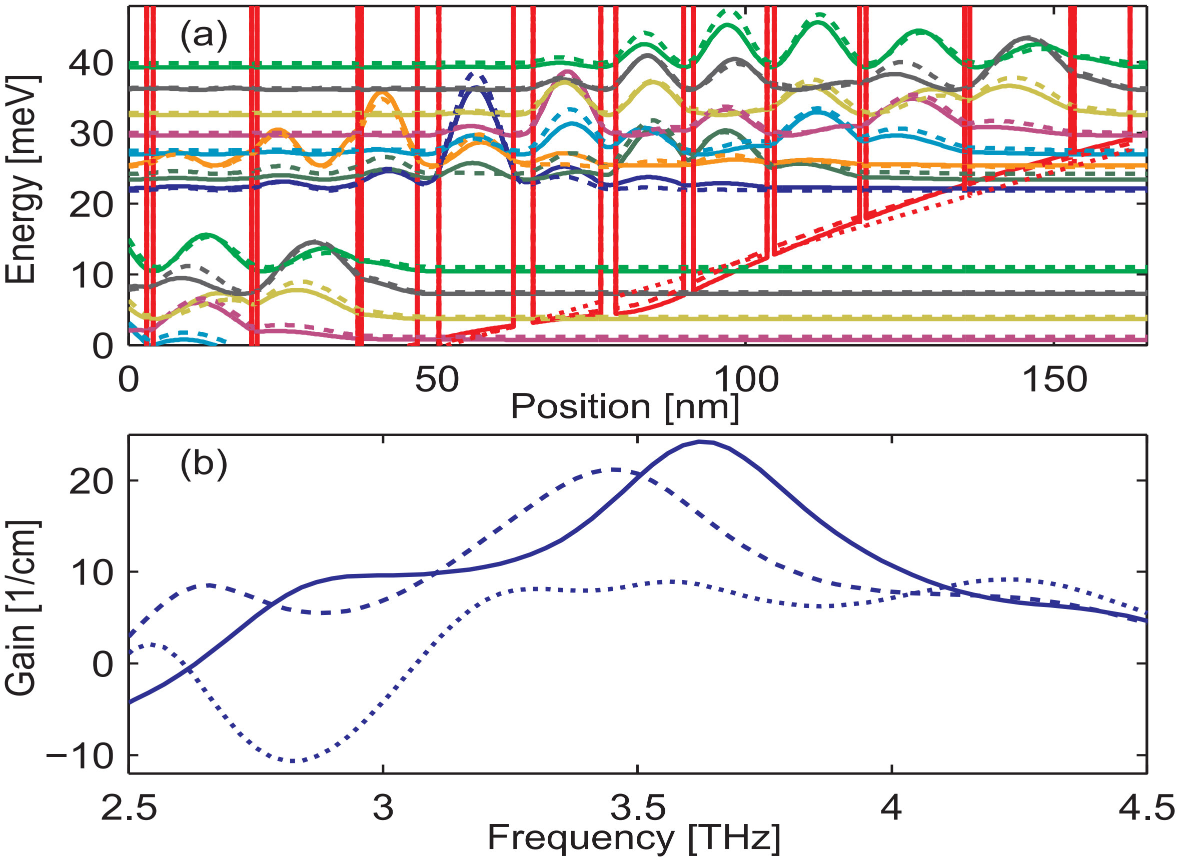

Figure 2.6.1: (a) Conduction band profile and squared wavefunctions, obtained for thermally occupied subbands (dashed lines) and self-self consistent simulations (solid lines).The conduction band profile without space charge effects included is also displayed as a reference (dotted line). (b) Simulated spectral gain versus frequency for the three cases of accounting space charge effects, shown above.

and

depletion of the lower laser state leads to the filling of the upper laser state (lowest state in the miniband) and in this way population inversion is reached between the upper laser level and the lower laser level of the next miniband.

In the material systems of today's QCLs, the main scattering mechanism that governs the dynamics and performance of the structures is the electron-phonon scattering. The depletion of the lower laser level is mainly governed by LO-phonon scattering. After the depletion of the lower laser level, electrons should be efficiently carried into the upper laser level of the next period. This is done by the injector levels, which are usually to some degree overlapped with the upper laser level for an efficient electron injection. In this thesis we will mainly focus on bound to continuum and resonant phonon depopulation structures, both in the THz and infrared regime.

2.6.2 Space charge effects

We present simulations for a 3.5 THz BTC design [60] to demonstrate the importance of e-e interactions and space-charge effects on the transport and material gain in such structures. In particular, the validity of neglecting the exchange effect in Section 2.3.8.1 and employing simplified screening models for the evaluation of e-e scattering is investigated. Also the importance of self-self consistent simulations for a proper inclusion of space charge effects is discussed. All scattering mechanisms are evaluated self-consistently in our EMC simulation tool. Interface roughness (IR), however, whose parameters are hard to measure and depend critically on the growth conditions, has to be described in terms of a phenomenological model [12, 61]. We have used the typical values of $\Lambda = 10\,\mathrm{nm}$ for the correlation length and $\Delta = 0.12\,\mathrm{nm}$ for the mean height of interface roughness in theses structures [12, 62].

In Fig. 2.6.1, the simulated conduction band states as well as the spectral gain of the investigated BTC QCL is shown for a lattice temperature $T_\mathrm{L} = 10\,\mathrm{K}$ at the design bias of 2.5 kV/cm, where the maximum gain is obtained in the simulation. Solid lines indicate the fully self-self consistent result, i.e., Schrödinger-Poisson (SP) and EMC simulations are carried out iteratively until convergence is reached. The dashed lines are results obtained by solving the SP system once in the beginning assuming a thermal carrier distribution [27] and then performing a self-consistent EMC simulation, which is a quite common approach [30, 31, 24, 63]. For comparison, also the conduction band profile and spectral gain is shown as obtained with deactivated Poisson solver (dotted lines), i.e., when no band bending is taken into account as a result of space charge effects. In all the three cases, carrier-carrier scattering is evaluated taking into account the exchange interactions as well as screening considered in random phase approximation (RPA). RPA is implemented by repeatedly solving Eq. (2.3.91) to account for changes in the carrier distribution during the EMC simulation.

Based on the results shown in Fig. 2.6.1 we affirm that the proper inclusion of space charge effects largely affects the simulation outcome for the investigated BTC structure. A significant tilt of the conduction band is observed when taking the Poisson equation into account for the modeling of space charge effects (solid and dashed lines in Fig. 2.6.1 (a)), which change the subband eigenenergies and wave functions. By comparing our results to experimental data we can confirm that only the simulation results with space charge effects included are in line with experiment. The gain profile obtained without the Poisson solver is exceedingly reduced and broadened, see Fig. 2.6.1 (b) (dotted curve). The low peak gain of around $9\,\mathrm{cm}^{-1}$ at 4.2 THz contradicts the experimentally observed lasing of the QCL at 3.5 THz [60]. The large gain bandwidth also disagrees with electroluminescence measurements, that yield full width at half maximum (FWHM) widths of clearly below 1 THz [60]. The inclusion of space charge effects results a realistic gain profile which is centered around 3.5 THz and it is in good agreement with experiment. The FWHM widths of 0.65 THz (solid curve) and 0.66 THz (dashed curve) agree qualitatively with the linewidth extracted from electroluminescence measurements (0.85 THz at 10 K) [60]. Still, the two gain profiles are different to some degree, having peak gain values of $24.2\,\mathrm{cm}^{-1}$ for the self-self consistent and

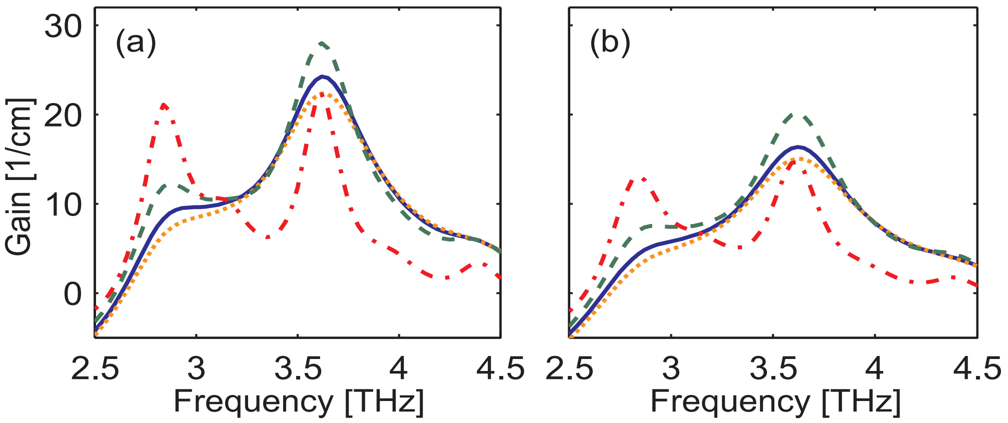

Figure 2.6.2: Simulated gain spectra vs frequency, obtained by fully taking into account (solid curves) and ignoring the exchange effect (dotted curves), and by ignoring parallel (dashed curves) spin collisions. As a reference, the result obtained without e-e scattering is also shown (dash-dotted curves). The simulation results are shown for a lattice temperature of (a) 10 K and (b) 90 K.

$21.2\,\mathrm{cm}^{-1}$ for the self-consistent approach. This gives an insight into the importance of self-self consistent EMC simulations for terahertz BTC designs, where space charge effects tend to play a pronounced role in contrast to equivalent RP structures.

2.6.3 Exchange effect

There are two standard approaches to account for e-e scattering without considering the actual spin dependence. The first method tends to overestimate the exchange effect by completely neglecting the parallel spin collisions [44, 49], implying $p_a = 1/2$, $p_p = 0$ in Eq. (2.3.93). The second approach ignores the spin dependence of electrons. In this way two electrons colliding with parallel and antiparallel spin are treated in the same way [49], which corresponds to $p_a = 1$, $p_p = 0$ in Eq. (2.3.93). In RP structures, where a moderate amount of doping is used, at elevated temperatures the carrier transport is dominated by LO-phonon scattering and the contribution of the exchange effect is usually negligible. In BTC designs, however, where minibands are formed by closely spaced energy levels, e-e scattering plays a more pronounced role [12].

Fig. 2.6.2 contains the self-self consistent gain spectra at $T_\mathrm{L} = 10\,\mathrm{K}$ and $T_\mathrm{L} = 90\,\mathrm{K}$, with the self-consistent inclusion of screening, i.e., taking into account screening in the RPA. Results are shown for $p_a = p_p = 1/2$ (solid curve), $p_a = 1$, $p_p = 0$ (dotted curve), $p_a = 1/2$, $p_p = 0$ (dashed curve), and $p_a = p_p = 0$ (dash-dotted curve). The dash-dotted curves yield very narrow gain spikes around 2.8 and 3.6 THz, largely deviating from the experimental electroluminescence measurements [60]. This is a direct proof of the importance of e-e scattering for such QCLs. As discussed in Section 2.6.2, for $T_\mathrm{L} = 10\,\mathrm{K}$ the full simulation with the included exchange effect yields a realistic gain profile, as shown by the solid curve in Fig. 2.6.2 (a). Ignoring the exchange effect (dotted curve) leads to an overestimation of e-e scattering, resulting in a peak gain reduction by 8%, and an increase of the full width at half maximum (FWHM) gain bandwidth by 11%. Completely neglecting parallel spin collisions (dashed curve), however, leads to a gain bandwidth reduction of 24%, and an increase of the peak gain by 15%. For a lattice temperature $T_\mathrm{L} = 90\,\mathrm{K}$, Fig. 2.6.2 (b) shows the reduction and broadening of the gain due to the increase of temperature which is in good agreement with experiment [60, 12]; also for this temperature, ignoring the parallel spin collisions or exchange effect has the same effects on the simulated gain profile as for the case of $T_\mathrm{L} = 10\,\mathrm{K}$.

In Fig. 2.6.3, the electron temperatures and the relative occupations of the different states within the miniband are shown at $T_\mathrm{L} = 10\,\mathrm{K}$ (compare Fig. 2.6.1 (a)). We perform a least square fit of the electron distribution functions provided by EMC to a Maxwellian to find the electron temperatures. While the occupations of the different subbands slightly depend on the implementation of the exchange effect, the electron temperatures show a stronger dependence. For example, the extracted temperature for the 8th level (at 39.3 meV) varies from 121.6 K to 146.7 K, depending on the implementation of the spin dependence. The pronounced dependence of the spectral gain and electron temperature on the implementation, and the reduced sensitivity of the occupations, becomes clear by looking at the average dwell time of an electron in a given subband, which is the inverse of the out-scattering rate from this subband. In Fig. 2.6.4, the dwell time is shown for the eight energy levels, characterized by their eigenenergies. For the case when scattering is low, the dwell time is high, corresponding to the case when parallel spin collisions are ignored in the simulation (dashed curve). This is consistent with the increased peak-gain and reduced linewidth values of the corresponding gain profile in Fig. 2.6.2 (a), which are closely related to the out-scattering rate [12]. The electron dwell time, on the other hand, increases by a similar factor for all the subbands which explains the relative insensitivity of subband occupations to the chosen implementation of Eq. (2.3.93).

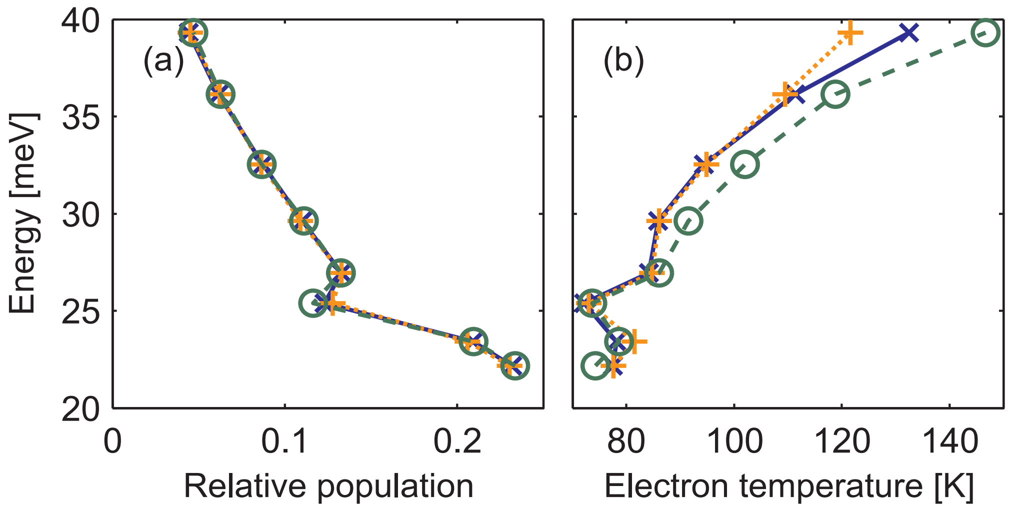

Figure 2.6.3: (a) Subband occupations and (b) subband temperatures extracted from our EMC simulations, by fully taking into account (x-marks, solid curves) and ignoring the exchange effect (plus signs, dotted curves), and by ignoring parallel spin collisions (circles, dashed curves). The lines are guide to the eye.

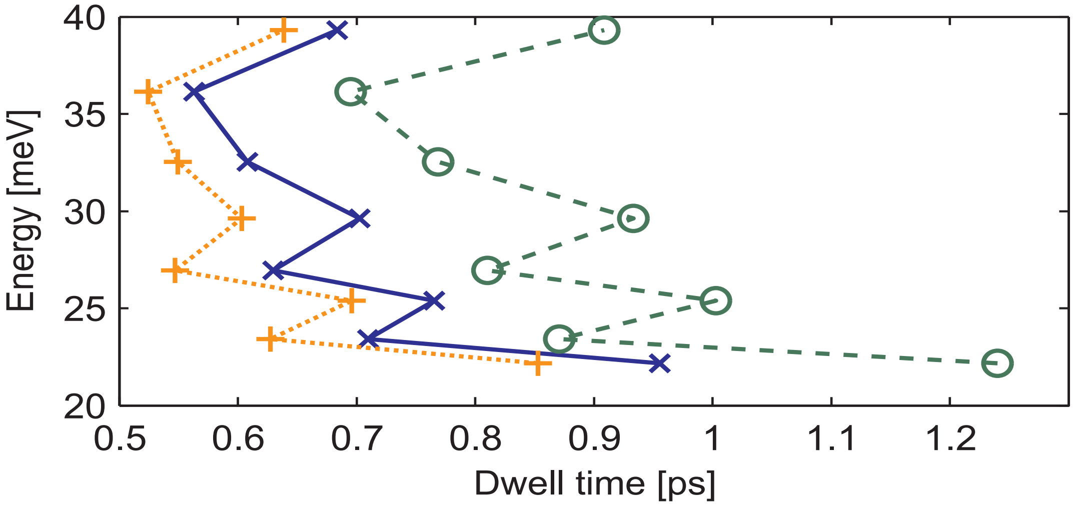

Figure 2.6.4: Electron dwell times, simulated by our EMC method, by fully taking into account (x-marks, solid curves) and ignoring the exchange effect (plus signs, dotted curves), and by ignoring parallel spin collisions (circles, dashed curves). The lines are guide to the eye.

2.6.4 Screening

Screening is commonly taken into account using simplified models rather than solving Eq. (2.3.91) directly, since the computational effort involved in the RPA is increased. For instance, we can account for screening by defining a wavenumber q_s in Eq. (2.3.78), i.e., replacing the pre-factor $e_0^2/(2\varepsilon q)$ by $e_0^2/[2\varepsilon(q+q_\mathrm{s})]$. In single subband models, the screening wavenumber q_s is obtained from Eq. (2.3.91) by assuming that screening is caused only by a single subband, e.g., the ground state [31, 50]. For RP structures, the modified single subband model [50] for screening of e-e interactions has been shown to yield improved results, with

$$q_\mathrm{s} = \frac{e_0^2}{2\varepsilon}\frac{m_{||}}{\pi\hbar^2}\sum_i f_i(\mathbf{k}=\mathbf{0}), \tag{2.6.1}$$

where i sums over the subbands in one period.

In Fig. 2.6.5, the intrasubband Coulomb matrix elements V_{1111} (Fig. 2.6.5 (a)) and V_{1212} (Fig. 2.6.5 (b)), as well as the intersubband element V_{1122} (Fig. 2.6.5 (c)) are shown as a function of the wavenumber q. Here, 1 and 2 denote the upper laser level at 22.2 meV and the level directly above at 23.4 meV, see Fig. 2.6.1 (a). Displayed are the screened matrix elements based on the RPA (solid lines) and the simplified model according to Eq. (2.6.1) with $q_\mathrm{s} = 0.0237\,\mathrm{nm}^{-1}$ (dashed lines), as well as the bare matrix elements defined in Eq. (2.3.78) (dotted lines). In the simplified screening model the intersubband elements approach zero for small wavenumbers, as shown in Fig. 2.6.5 (c), in contrast to the exact implementation of the RPA. A more accurate result is obtained by taking the simplified screening model only for the intrasubband matrix elements, and by treating intersubband scattering without screening [64].

The self-self consistently calculated gain spectra at $T_\mathrm{L} = 10\,\mathrm{K}$ and $T_\mathrm{L} = 90\,\mathrm{K}$ are shown in Fig. 2.6.6. Here, the exchange effect is included, but different screening models are used, in contrast to Fig. 2.6.2.

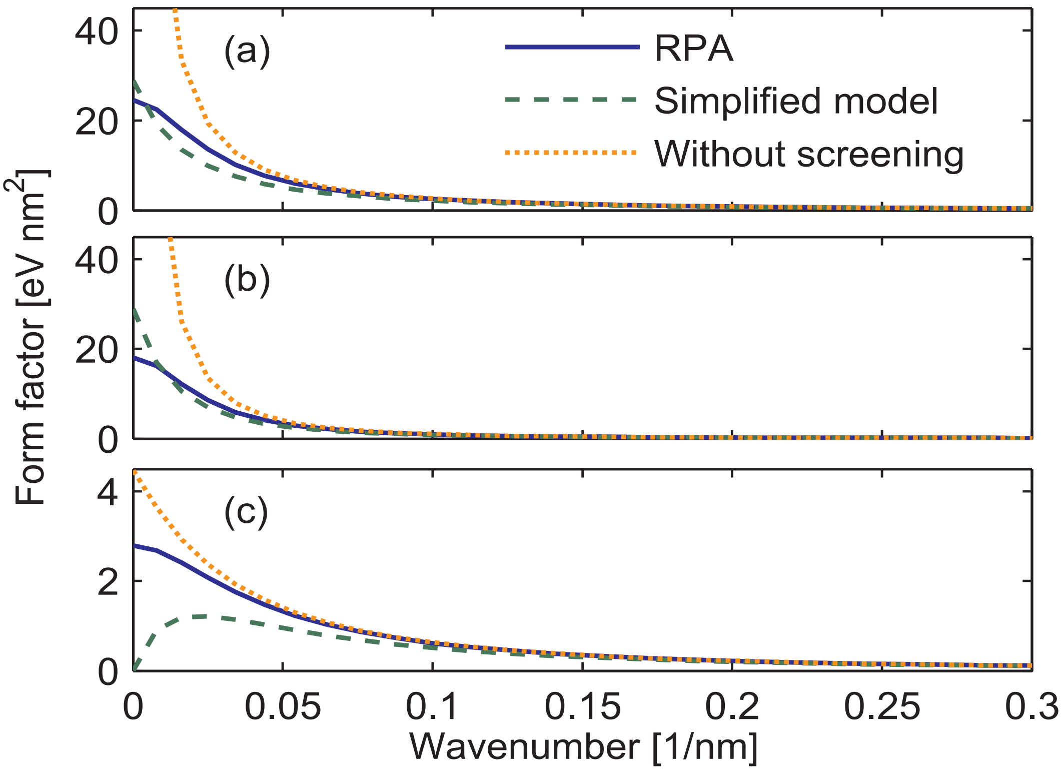

Figure 2.6.5: Coulomb matrix elements, as obtained with different types of screening models for the structure shown in Fig. 2.6.1(a). (a) V_{1111}; (b) V_{1212}; (c) V_{1122}.

The exact evaluation of the RPA (solid curves), which we consider as the reference curve, agrees well with experiment, as shown in Section 2.6.2. We find an overestimation of the screening of the intersubband elements by applying the simplified screening model to all matrix elements, as shown in Fig. 2.6.5 (c), and thus a resulting underestimation of scattering. The resulting spectral gain profile at 10 K (dashed curve

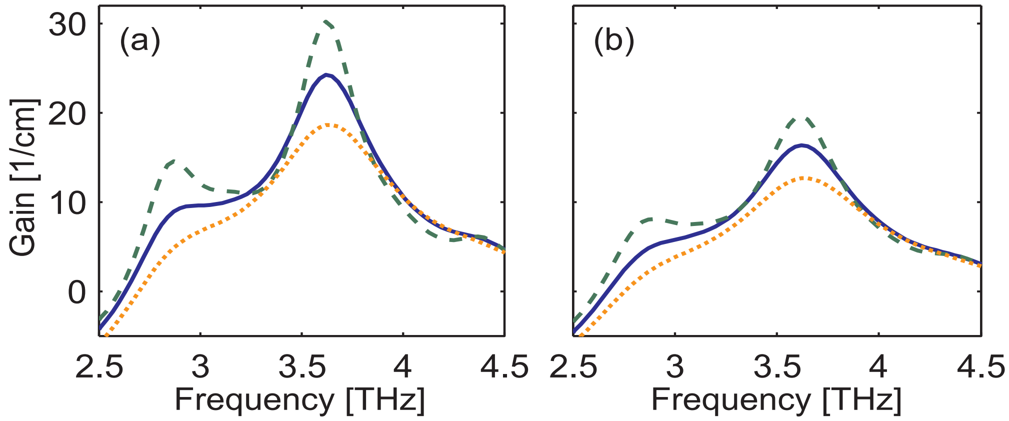

Figure 2.6.6: Spectral gain as a function of frequency, obtained by our EMC method. The three cases shown account for screening in the RPA (solid curves), in the modified single subband model for all matrix elements (dashed curves) or in the modified single subband model for the intrasubband elements only (dotted curves), i.e., treating intersubband elements as unscreened. (a) $T_\mathrm{L} = 10\,\mathrm{K}$; (b) $T_\mathrm{L} = 90\,\mathrm{K}$.

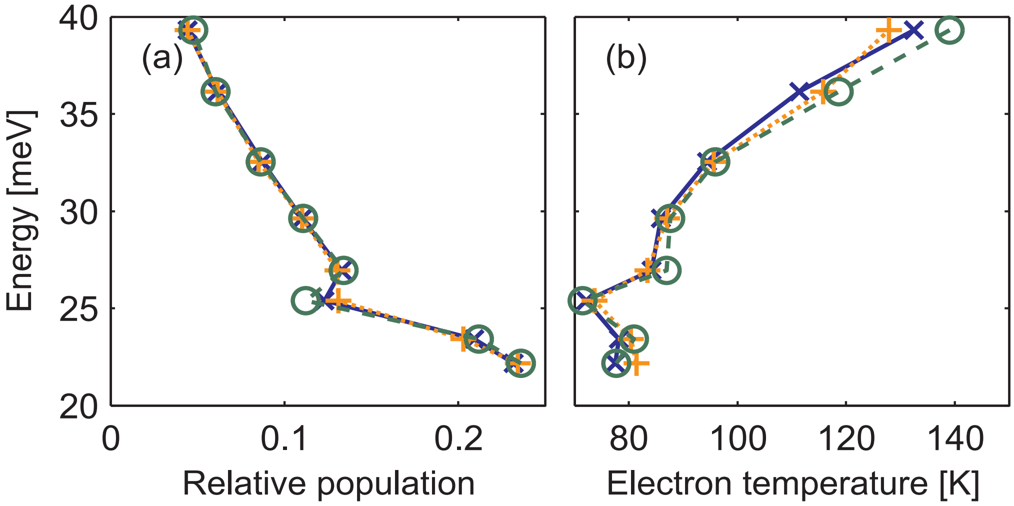

Figure 2.6.7: (a) Relative subband occupations and (b) subband temperatures, as obtained by our EMC method where for the screening we have used the RPA (x-marks, solid curves) and the modified single subband model for all matrix elements (circles, dashed curves) or for the intrasubband elements only (plus signs, dotted curves). The lines are guide to the eye.

in Fig. 2.6.6 (a)) features a 25% enhanced gain peak and a very narrow spectral bandwidth (FWHM) of 0.43 THz, as compared to an experimental value of 0.85 THz. On the other hand, by completely ignoring the screening effect for the intersubband matrix elements, we overestimate the intersubband scattering, thus resulting in a lowered and broadened gain profile (dotted curves). As can be seen from Fig. 2.6.6 (b), the simulation results at $T_{\mathrm{L}} = 90\,\mathrm{K}$ are affected in a similar way by using the above discussed approximations.

In Fig. 2.6.7, we compare the relative subband occupations and electron temperatures at $T_{\mathrm{L}} = 10\,\mathrm{K}$ for the different screening models. In spite of the fact that the spectral gain in Fig. 2.6.6 greatly depends on

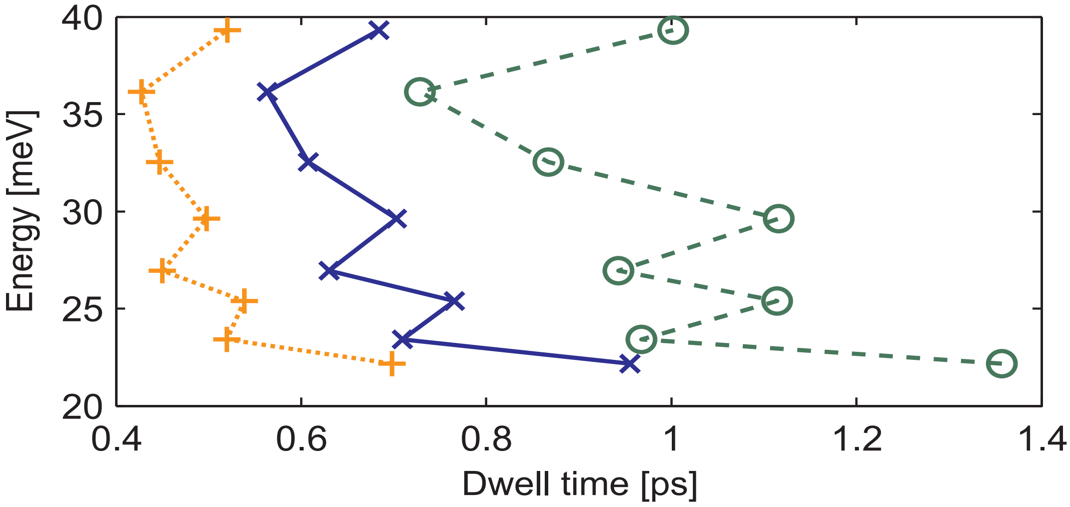

Figure 2.6.8: Electron dwell times, extracted from our EMC simulations which were obtained by taking into account screening in the RPA (x-marks, solid curves), and using the modified single subband model for all matrix elements (circles, dashed curves) or for the intrasubband elements only (plus signs, dotted curves). The lines are guide to the eye.

the applied screening model, the occupations of the miniband levels in Fig. 2.6.7 (a) are quite insensitive to the chosen implementation. This is similar to the behavior in Fig. 2.6.3, which is consistent with the fact that the average dwell time of an electron in a level strongly depends on the chosen screening model, but is changed by a similar factor for all subbands as shown in Fig. 2.6.8. We attribute this to the structure of the minibands, which are quasi-continuous in BTC QCLs. In contrast, the energetic separation of the levels greatly varies for RP QCLs, and simple approaches like the single subband screening model have been shown to significantly affect the level occupations [31, 50]. For this case, only a single subband which is usually the ground level, is considered [50]. However, it should be noted that also for the analyzed BTC QCL, this method would provide somewhat less accurate results than using Eq. (2.6.1), as done in our simulations. The electron distribution as a function of kinetic energy within each subband can be represented by fitted electron temperatures in Fig. 2.6.7 (b) and these show a moderate dependence on the screening model. As an example, the calculated temperatures in the 8th state (at 39.3 meV) range from 127.9 K to 139.0 K for the different types of screening. Here once again, more relevant deviations from the RPA calculation would arise by implementing a single subband screening model rather than Eq. (2.6.1), i.e., the modified single subband model.

2.7 Summary

We have derived the basic theory for the treatment of carrier transport in quantum cascade lasers by means of EMC methods. Starting from the Schrödinger equation, the transfer matrix method for finding the wavefunctions was discussed. An example was shown for the application of the transfer matrix method to find the wavefunctions in a leaky quantum well. Non-parabolicity was introduced both in the confined and in the planar direction of the structures, which is particularly important for mid infrared QCLs due to their large laser level spacing. Fermi's golden rule was derived from time-dependent perturbation theory

chapter/section	2.6	3.1, 3.3	3.2	4	5.1	5.1.3	5.2
non-parabolicity (in plane)	×	×	×	×	×	×	√
non-parabolicity (in growth direction)	×	×	×	×	√	√	√
electron-electron scattering (parabolic)	√	√	√	√	√	√	×
phonon scattering (parabolic)	√	√	√	√	√	√	×
impurity scattering (parabolic)	√	√	×	√	√	√	×
interface roughness scattering (parabolic)	√	√	√	√	√	√	×
alloy scattering (parabolic)	×	×	×	×	√	√	×
electron-electron scattering (non-parabolic)	×	×	×	×	×	×	√
phonon scattering (non-parabolic)	×	×	×	×	×	×	√
impurity scattering (non-parabolic)	×	×	×	×	×	×	√
interface roughness scattering (non-parabolic)	×	×	×	×	×	×	√
alloy scattering (non-parabolic)	×	×	×	×	×	×	√
photon scattering (parabolic)	×	×	×	×	×	√	×
photon scattering (non-parabolic)	×	×	×	×	×	×	√

Table 2.2: Scattering mechanisms and approximations used in the thesis.

for the case of static and harmonic perturbations. The non-parabolic scattering mechanisms were derived from scratch by starting from the physical interpretation of each mechanism, arriving at its perturbation Hamiltonian and using Fermi's golden rule to find the scattering rate. Based on the scattering rates, the structure of the Monte-Carlo algorithm was discussed, furthermore examples for its application to device analysis were presented. These examples illustrate the influence of electron-electron scattering on the transport and optical properties of bound to continuum quantum cascade lasers. Particularly the importance of the correct screening model as well as the influence of the exchange effect for electron spin modeling was shown.

The implementation of the different mechanisms in this chapter was performed gradually. Hence we give in Table 2.2 the approximations and effects that are included in each of the sections in this thesis.

Chapter 3

Comparison of EMC and NEGF methods for cascade structures

A detailed analysis of quantum transport theory can offer a good understanding of the microscopic processes in quantum cascade structures such as QCLs and Stark ladders with THz transitions. In typical THz QCLs, the level spacing and lasing transitions are much smaller than for the case of mid-infrared QCLs. Coherent tunneling of electrons between quantum wells could play an important role in these structures. Furthermore, accurate transport models are required to identify the detrimental effects [24, 65, 27, 66] that decrease the occupation inversion and the optical gain in state of the art THz quantum cascade lasers (QCLs). Two intensely used theories for modeling of transport in QCLs are the non-equilibrium Green's function method (NEGF) and the Ensemble Monte Carlo method (EMC).

The non-equilibrium Green's function method (NEGF) [16] is a frequently implemented quantum transport model, while our EMC method is considered to be semiclassical [25, 12]. NEGF is a very general scheme to treat quantum effects such as particle correlations, carrier confinement and interferences, as well as energy and momentum relaxation and phase breaking scattering events self-consistently [19]. The NEGF method requires the self-consistent solution of the Keldysh and the Dyson equation and the scattering self-energies of every implemented scattering mechanism. These expressions have been implemented in a real space basis. The choice of the basis increases the numerical load significantly but allows for the consideration of electrons confined in quantum wells, as well as propagating electrons in the continuum. We have to solve a system of four coupled partial differential equations in order to determine the Green's functions and self-energies. In this way, the scattering states, the transition probabilities between them and their occupations are calculated self-consistently. We emphasize that the solution of the four coupled differential equations is numerically very demanding. Once the Green's functions have been computed, observables such as the current and the electron density can be straightforwardly calculated [19, 67]. They automatically include all coherent and incoherent effects that are represented by the system's Hamilton operator and the scattering self-energies. Further details of the NEGF model can be found in [19] and the references therein. Exact inclusion of higher order many particle interactions such as the inelastic electron-electron scattering is typically unfeasible in NEGF. Furthermore it is common to either simulate a limited amount of QCL periods or to approximate the in-plane momentum by a typical single value due to numerical restrictions. Simulating only a limited amount (1-2) of QCL periods with an exact NEGF approach without e-e scattering, can take from a few days to weeks. For these reasons, numerically more efficient models are frequently implemented in literature which imply different approximations.

One example for numerically effective methods is our EMC method based on the solution of the semiclassical Boltzmann equation in a subset of the eigenfunctions of the device Hamilton operator. This subset is restricted to low eigenenergies and the Boltzmann equation is solved to determine the occupancies of the device states through distribution functions and scattering rates. Except for the solution of the Poisson equation, no further iterations enter the EMC method which gives a major numerical advantage. However, the device electrons in this method are represented in an incomplete basis which misses the continuum states. In addition, these basis functions have an infinite lifetime which is known to yield artificially sharp resonances in the charge transport. This is in particular problematic for the calculation of the optical gain. For this reason, the common EMC method was extended to calculate the optical gain assuming a Lorentzian level broadening according to the intersubband out-scattering rates [12]. EMC also neglects non-diagonal scattering [17, 18], i.e., scattering with perturbation potentials in the form $V_{mm}V_{nn}$ and $V_{mi}V_{jn}$ which is implemented in NEGF. Furthermore, the semiclassical nature of the EMC method may lead to a significant overestimation of the current density in the presence of degenerate device states and an underestimation of coherent transport. However, the reduction of numerical load makes it well suited for systematic variations of a large number of device parameters.

We show in this chapter that the EMC and NEGF results agree well in regimes where coherent transport plays a minor role. Since the threshold current of typical resonant phonon depopulation structures lies in the incoherent regime (or lasing regime) [68], the EMC method is a well suited method for modeling transport. In particular, the numerical efficiency of EMC allows for the systematic improvement of future THz-QCL designs [22].

3.1 Stark ladders

The most elementary quantum cascade structures are Stark ladders [69]. They are favorable, since an interpretation of the obtained simulation results is facilitated by the relatively small number of states per period. Additionally, the short period length of the Stark ladders is numerically advantageous for our NEGF simulations. We compare the EMC and NEGF theories based on the obtained current-voltage (IV) characteristics and optical gain for the simulated Stark ladders. All parameters of both

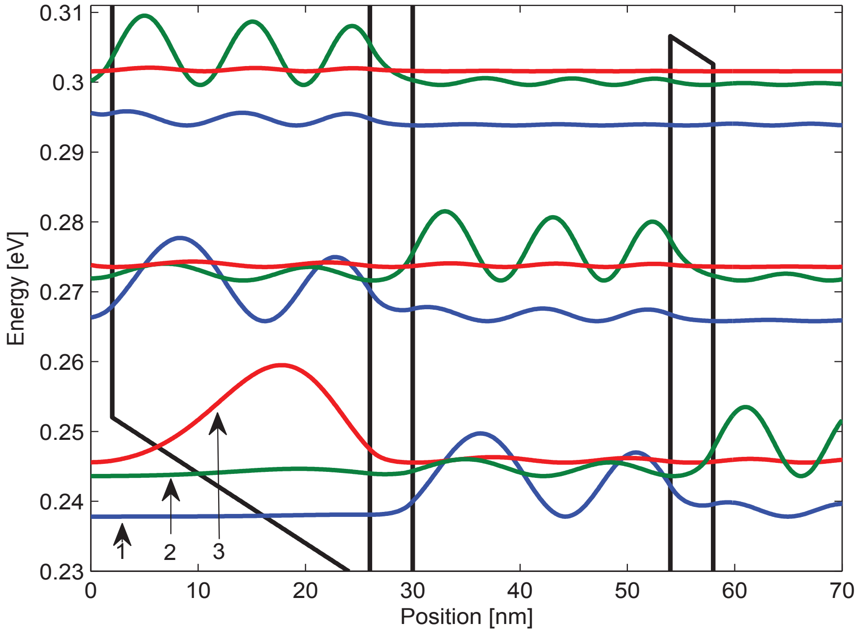

Figure 3.1.1: Conduction band profile and absolute square of the wavefunctions for the investigated Stark ladder [69], biased at 10 kV/cm. It consists of 40 Å $Al_{0.1}Ga_{0.9}As$ barriers and 240 Å wells. The doping in the well is 10^{10} cm^{-2}.

methods are either well established material parameters or taken from literature. Both transport models in this section take into account the incoherent scattering of electrons with longitudinal polar optical phonons (LO-phonons), acoustic phonons, charged impurities and rough interfaces, and the electron-electron interaction is considered in the Hartree approximation.

We apply the EMC and the NEGF method on electronic transport in two types of Stark ladders, i.e., 240 Å wells with 20 Å barriers and 240 Å wells with 40 Å barriers [69]. The Stark ladders for the second case are shown in Fig. 3.1.1, where we see a moderate extension of the states in the adjacent wells. This delocalization is even stronger when the barriers are halved. The lattice temperature and sheet doping density were taken as 100 K and 10^{10} cm^{-2}. The doping was reduced to a factor of 10 smaller than in the original design [69] for using the approximate sheet doping in resonant phonon depopulation THz QCLs.

The current-voltage characteristics are compared in Fig. 3.1.2 (a) for the 20 Å barrier case and in Fig. 3.1.2 (b) for the 40 Å barrier case, showing a good agreement. For Stark ladders as for resonant phonon depopulation THz QCLs, the current is mainly carried by LO-phonon scattering while Coulomb scattering plays only a secondary role. We identify a leakage region for the Stark ladder with 20 Å barriers, where conduction of electrons through continuum states is identified by NEGF. The NEGF approach implements electronic states in real-space self-consistently, thus is able to take into account the continuum states adaptively. EMC, however, underestimates the current in the leakage region due to the limited number of higher lying states that it can use with periodic boundary conditions. The absorption for the 20 Å barrier case does not agree between the two methods (not shown), indicating

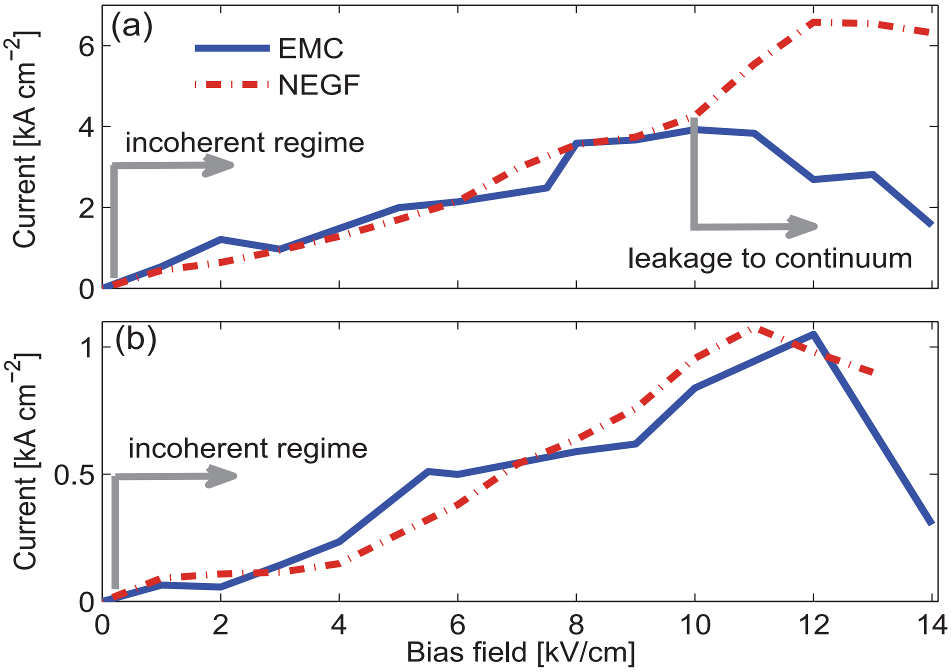

Figure 3.1.2: Calculated IV-characteristics of the GaAs/Al$_{0.1}$Ga$_{0.9}$As Stark ladders operating in the THz regime. The wells are 240 Å. Barrier widths are 20 Åin (a) and 40 Å in (b) respectively. Results of the EMC method are depicted by the solid line and agree in a large bias range with NEGF calculations (dash-dotted).

that EMC in this regime starts to become unreliable. We note, however, that barriers contain only 10% of aluminum and they are very thin compared to the wells, which gives almost the bulk limit. For this case the states become highly unbound and, as discussed in Section 2.1.3, the quasi-bound approximation becomes invalid, i.e., EMC fails to predict the current. At low bias fields, where several barriers still limit the coupling of the states to the continuum this does not happen. When the field is increased, however, the leakage into the state continuum sets in, and the EMC method underestimates the current density. This leakage is efficiently suppressed for increased barrier widths too, as shown in Fig. 3.1.2 (b) for the Stark ladder having 40 Å barriers. The onset of the leakage into the state continuum is shifted towards higher applied electric fields here and the results of both methods agree in a larger bias range. We also observe a factor of 6 increase in the maximum currents by halving the barriers, showing the sensitivity to the barrier thickness.

It is worth mentioning that a coherent transport regime is not present for the Stark ladders, as shown in Fig. 3.1.2. In the coherent transport regime, where scattering is suppressed due to the misalignment of the levels, EMC can also underestimate the current as we will see for THz QCLs. As shown in Fig. 3.1.3, the obtained spectral loss of the Stark ladder agrees well for the two methods. The spectral loss, however, can still disagree for some bias points even for the Stark ladder with 40 barriers. We attribute this to the remaining unbound nature of the states even for this barrier thickness, as well as the different boundary conditions of EMC and NEGF. While EMC used periodic boundary conditions, in NEGF three wells and

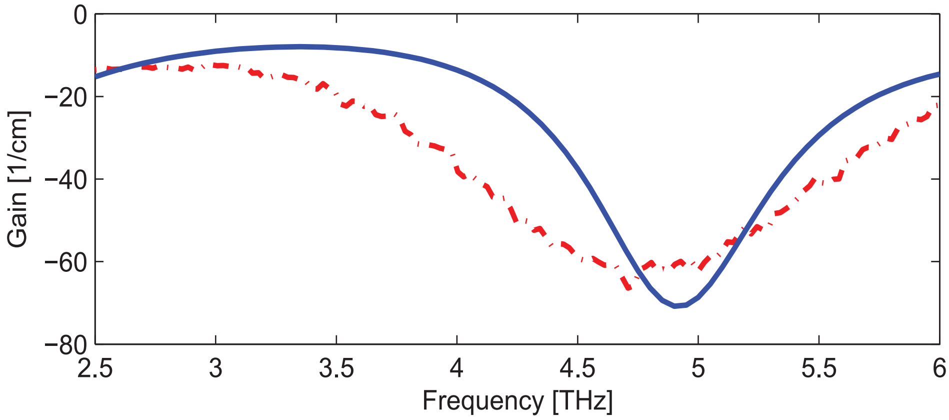

Figure 3.1.3: Theoretically predicted absorption for the Stark ladder with 40 Å barriers at 10 kV/cm, designed to operate at a frequency of 4.9 THz. Results of the EMC method (solid) nicely agree with results of the NEGF method (dash-dotted).

field-free periodic leads were used to 'approximate' the cascade periodicity.

We see a good agreement for the absorptions calculated by NEGF and EMC in Fig. 3.1.3. We mention, however, that we had to integrate the spatially resolved absorption coefficient in NEGF, which had some uncertainties in choosing the actual interval where the results are not influenced by the leads.

3.2 Quantum cascade laser emitting at 2.75 THz

We apply the EMC and NEGF method on stationary transport in the THz-QCL structure of [70] at a lattice temperature of 40 K and a sheet doping density of 1.95 $\times 10^{10}$ cm^{-2}. A single period of this QCL consists of a sequence of GaAs and $\mathrm{Al}_{0.15}\mathrm{Ga}_{0.85}\mathrm{As}$ layers of the widths (30) 92 (55) 80 (27) 66 (41) $\underline{155}$ Å, with the $\mathrm{Al}_{0.15}\mathrm{Ga}_{0.85}\mathrm{As}$ barriers given in parenthesis. The underlined well contains homogeneous doping. In both methods, we take electron-phonon and interface roughness [61] scattering into account. Electron-electron interaction is implemented in the Hartree approximation by a Poisson solver. In addition, we also account for inelastic electron-electron scattering in the EMC method. In order to illustrate the typical confinement energies and resonant laser states, Fig. 3.2.1 shows the magnitude squared of the wavefunctions used in the EMC method. The upper and lower laser levels are marked by solid lines.

States of adjacent periods are separated by the energy of an LO-phonon (36 meV). Thus, electrons traverse between the states of adjacent periods by the resonant emission of an LO-phonon. Thereby, the lower laser level gets emptied [71, 72]. The EMC method models electronic transport with eigenfunctions of the Hermitian Hamilton operator of the QCL structure. Incoherent scattering mechanisms that limit the electronic lifetime are not included in the determination of the QCL states. Thus, the electronic states in Fig. 3.2.1 are given as discrete levels. In EMC, elastic and inelastic scattering is only included in the calculation of the state occupancy. In contrast, the resonant energies, the state linewidth and state occupancies are self-consistently determined in the NEGF method.

In spite of this discrepancy, both models reproduce the experimental current-voltage (IV) character-

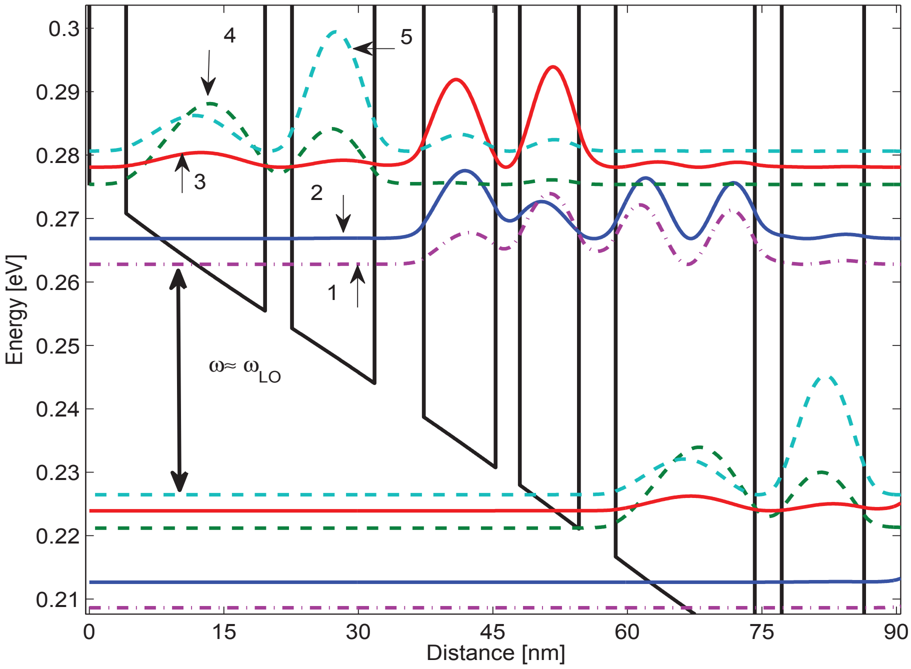

Figure 3.2.1: Energy levels and squared wavefunctions of the QCL at the peak-gain bias of 54.16 mV per period given by the EMC method.

istics for bias voltages above 30 mV per period, as shown in Fig. 3.2.2 (a). For bias voltages below 30 mV per period, however, the EMC method yields a very small current density. The energy separation of the electronic states simply does not allow efficient scattering of the electrons by LO-phonons for producing a current. We name this the coherent regime, since NEGF can still reproduce the experimental curve at these bias points. For this QCL, the dominant transport mechanism in this regime is the coherent multi-barrier tunneling [19]. We illustrate this in more detail in Fig. 3.2.2 (b), which shows IV-characteristics resulting from a ballistic NEGF calculation when all incoherent scattering mechanisms are neglected (* dashed line). At low bias voltages, results of the ballistic calculations agree with results of NEGF calculations including incoherent scattering (+ dashed line) which indicates the coherent nature of transport in this regime. Since coherent transport is neglected in EMC (× solid line in Fig. 3.2.2 (a)), the current density is very small in exactly that bias range which the NEGF formalism identifies as the coherent regime.

For voltages above 30 mV per period, the incoherent regime sets in. Here, incoherent scattering significantly enhances the current density in both methods. This is illustrated in Fig. 3.2.2 (b) for the example of interface roughness scattering. Calculations ignoring rough interfaces yield in the NEGF formalism (* dashed) and in the EMC method (• solid) a significantly smaller current density than the respective calculations including this effect (+ dashed for NEGF, × solid for EMC). Although the two methods require different interface roughness parameters (slightly larger interface roughness step height) to fit the experimental current, EMC can reproduce results of fully quantum mechanical calculations in

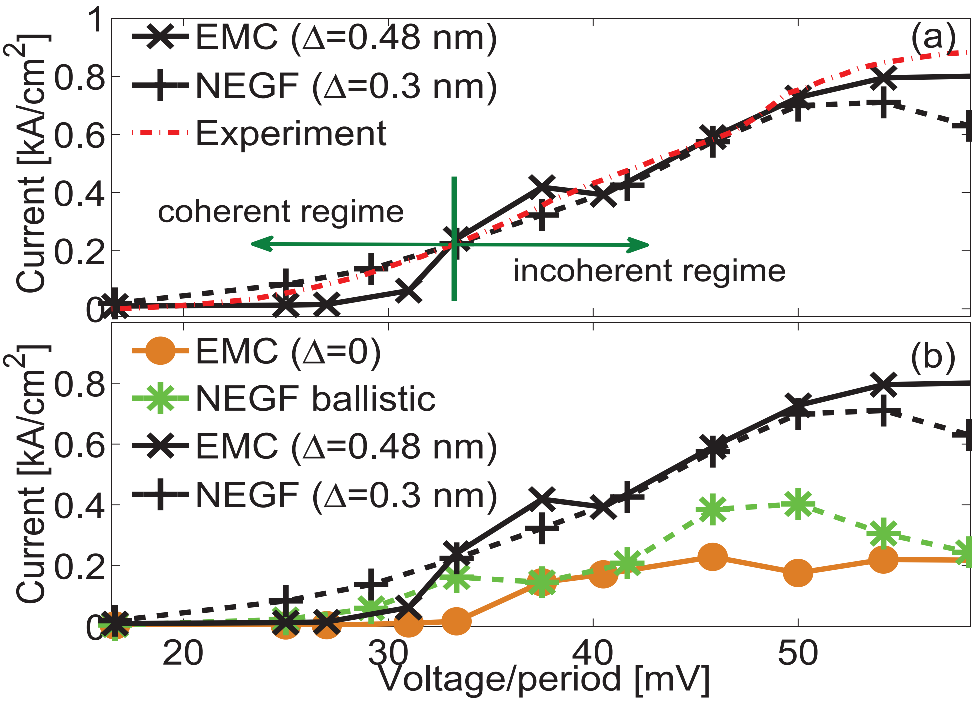

Figure 3.2.2: (a) Comparison of the simulated currents to experimental results. (b) Different cases of transport, which are shown to illustrate the contribution of the varying scattering and transport mechanisms.

the incoherent regime.

A well known issue arises when the discrete sharp energy levels in the EMC method get aligned [25]. Any narrow anticrossing of discrete states yields highly delocalized wavefunctions. Thus, the EMC method tends to overestimate the form factor and accordingly the scattering rate when discrete states are aligned. In this situation, the overestimation of scattering in the EMC method causes artificial current spikes [24] and often unreliable gain. Hence, bias voltages that correspond to aligned discrete states are commonly avoided in EMC calculations [25].

In contrast to the IV-characteristics, the optical gain is sensitive to the linewidth of the resonant states for every bias voltage. Therefore, the EMC method was augmented by a procedure that generates a spectrum of resonant QCL states with finite lifetime [12]. In this procedure, the discrete energy spectrum in Fig. 3.2.1 is multiplied by Lorentzian functions of widths that correspond to the calculated out-scattering rates. In order to show that this procedure gives consistent results, we compare in Fig. 3.2.3 the local density of states (LDOS) of the EMC (a) and the NEGF method (b).

We see a reasonable agreement between the resulting LDOS of both methods. The only significant difference is the missing resonance #4 in the NEGF calculation. State #4 in the EMC method originates from an alignment of state #5 with a state of the preceding QCL period (see Fig. 3.2.1 and Fig. 3.2.3 (a)). We model in our NEGF implementation only one QCL period with field free leads [73]. Therefore, the states of the preceding period lie at slightly different energies and this state anticrossing with state #5 is absent in the NEGF model (compare Fig. 3.2.3 (b) with (a)).

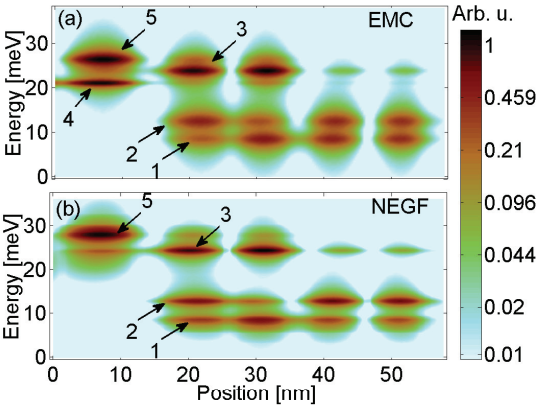

Figure 3.2.3: (a) EMC and (b) NEGF local density of states of the simulated QCL at the peak-gain bias of 54.16 mV per period. We observe similar linewidth and the missing level #4 in case of NEGF.

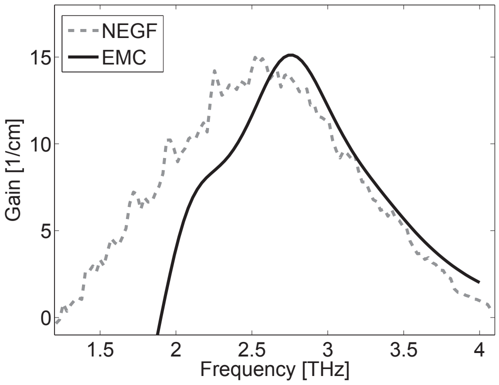

Figure 3.2.4: The optical gain in EMC (solid) and NEGF (dashed) at a bias of 54.16 mV per period. We get quantitative agreement. The slight asymmetry in EMC is explained in the text.

For the calculation of the gain in the EMC method we use the same procedure as for the LDOS, but here the Lorentzian are weighted with the occupation inversion [12]. Optical gain in the NEGF method is calculated in linear response [19], taking into account the occupation inversion and the finite linewidth. The qualitative agreement in the LDOS of both models (see Fig. 3.2.3) explains the good agreement of the predicted gain spectra shown in Fig. 3.2.4. We find the small discrepancy for photon frequencies below approximately 2 THz to originate from the missing resonance #4 in the NEGF calculation, (see Fig. 3.2.3 (a)).

3.3 Quantum cascade laser emitting at 3.4 THz

We investigate a resonant phonon THz-QCL [25] at a lattice temperature of 25 K. The conduction band profile and the relevant states in a single period of this QCL at a bias of 13.4 kV/cm are depicted in Fig. 3.3.1. The structure has a larger doping and lasing frequency than the previously investigated QCL. The upper and lower laser levels are marked by solid lines (4) and (2), while the upper and lower LO-phonon depopulation levels (1) and (5) are dashed. A resonant phonon-depopulation structure is based on the depletion of the lower laser level (2) through the upper phonon level (1) to the lower phonon level (5). Aftewards, electrons are re-injected into the upper laser level of the next period through the injection level (3). Note that the energy separation of the lower laser level (2) and state (5) of the next period approximately equals the LO-phonon energy.

The current-voltage characteristics for the 3.4 THz structure are compared to experiment in Fig. 3.3.2. Overall, the results of both methods agree well with experiments. However, we identify the same transport regimes as for the 2.75 THz QCL and find that the agreement of both methods depends on the respective regime. The coherent regime discussed in the previous section, is also identified for the 3.4 THz QCL. For low bias fields, the transport is typically dominated by coherent multi-barrier tunneling. For this

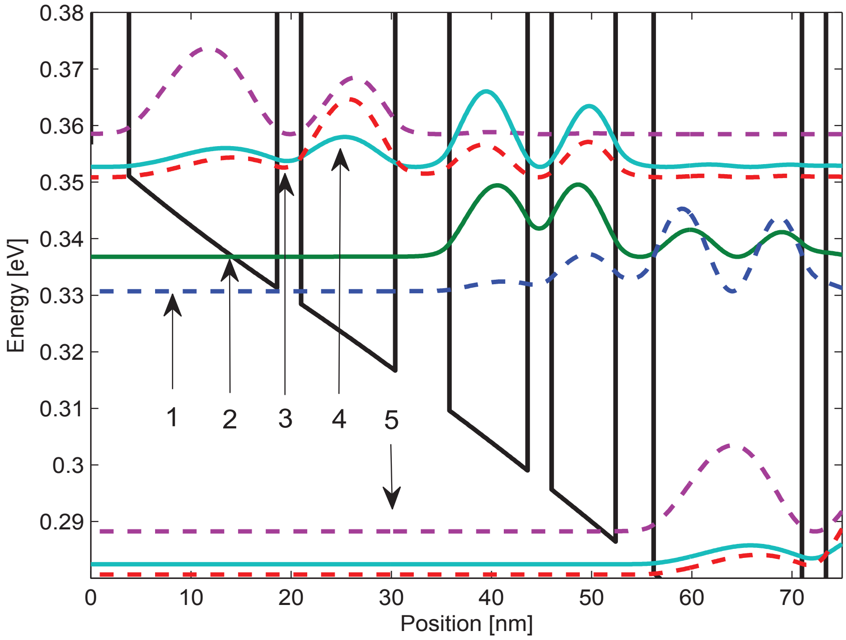

Figure 3.3.1: Conduction band profile and wavefunctions squared for the investigated QCL. The wavefunctions serve as input for the semiclassical EMC simulation. The modeled THz QCL (biased at 13.4 kV/cm) [25], consists of $Al_{0.15}Ga_{0.85}As$ barriers and GaAs wells with layer thicknesses (given in Å): (38) 64 (24) 78 (54) 94 (24) $\underline{148}$, where the values in the brackets represent the barriers. The underlined well contains a uniform sheet doping of 2.8 $\times 10^{10}$ cm^{-2}.

structure, however, as we see from the ballistic curves, coherent multibarrier tunneling does not increase the current in the coherent regime. We believe that the current is mainly carried here by the broadening of the levels, which still allow scattering transitions in contrast to sharp energy levels in EMC. We conclude that in the coherent regime, a realistic model requires the self-consistent inclusion of the level broadening and/or coherent multibarrier tunneling.

When the state alignment in this kind of QCL allows for the resonant emission of LO-phonons, a major fraction of the charge transport is controlled by incoherent scattering. This is the incoherent regime as illustrated in Fig. 3.3.2. The ballistic NEGF calculation (dotted), which ignores any kind of incoherent scattering, strongly deviates from the experimental data (dashed) for bias fields above 7 kV/cm. The bias of 7 kV/cm marks the borderline between the coherent and incoherent transport regimes. Since the EMC method does not include the finite linewidth of the resonant states, it notoriously underestimates the coherent tunneling at low bias fields. For this reason, the EMC method fails to predict transport in the coherent regime.

The 3.4 THz QCL exhibits large current spikes in the EMC simulation. These artifacts occur due to the narrow anticrossing of the device states especially between 7-10 kV/cm. Typically an anticrossing below 2 meV causes the wavefunctions to overlap considerably. Furthermore the energy conservation also gets fulfilled more easily due to the small level spacing. The large overlap and close level spacing favorizes scattering between these two levels, which is overestimated, leading to the overestimation of

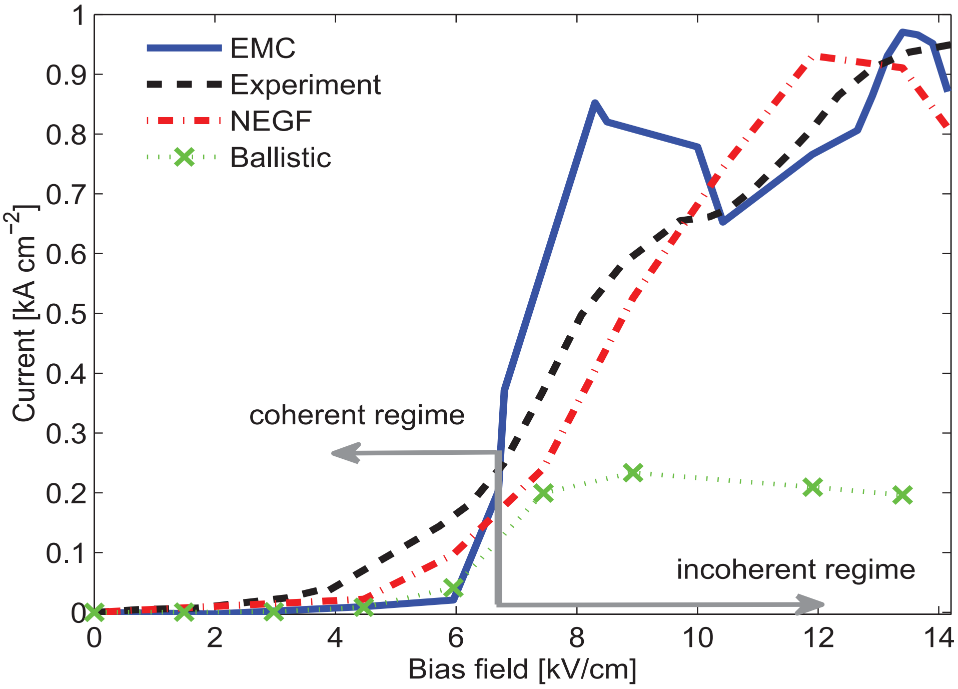

Figure 3.3.2: Calculated and experimental current-voltage characteristics of the THz-QCL in Ref. [25]. The ballistic NEGF calculation (dotted) ignores any incoherent scattering and yields much smaller current densities than results of NEGF calculations including all relevant scattering mechanisms (dash-dotted). Results of the EMC method (solid) agree quantitatively with NEGF calculations and experimental data (dashed) for bias fields above 10 kV/cm.

currents in the device. The current spike of the EMC method (solid in Fig. 3.3.2) at approximately 8.3 kV/cm originates from the alignment of the QCL states 1 and 3 (see Fig. 3.3.2). Current spikes, however usually do not occur in the region where the maximum gain is observed in THz QCLs. This is also the case for the 3.4 THz QCL, where EMC agrees well to the experiment above 10 kV/cm.

In Fig. 3.3.3 we compare the spectral gain profile for the two methods at the bias field of 13.4 kV/cm. We see a qualitative agreement, which confirms that in the incoherent regime transport is mainly semi-classical and the NEGF gain can be reproduced by EMC. We mention, however, that we consider the above results qualitative and the complete understanding of the nature of spectral gain in QCLs would

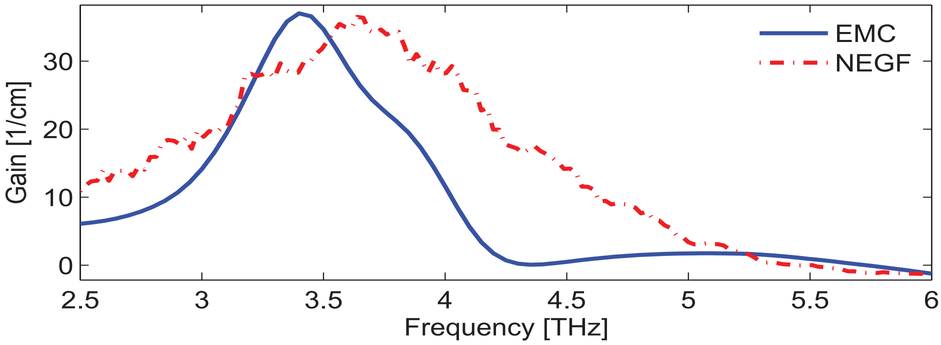

Figure 3.3.3: Spectral gain profile for the 3.4 THz QCL calculated by EMC and NEGF.

require further investigations.

3.4 Summary

We have compared results of the semi-classical EMC and the fully quantum mechanical NEGF method for stationary charge transport in quantum cascade lasers and Stark ladders. We find in the incoherent transport regime that the semi-classical EMC transport model nicely agrees in the predicted current density and optical gain with results of the fully quantum mechanical NEGF method. In particular, both models reproduce experimental results. For bias voltages significantly below threshold, coherent multi-barrier tunneling dominates the transport. Since EMC does not include this type of transport, it underestimates the current density in this regime. Nevertheless, the optimization of QCL designs requires reliable predictions close to and above threshold. Therefore, we have shown that for the purpose of design optimization, the numerical load of a detailed NEGF calculation can be avoided and the numerically efficient EMC method is appropriate.

For Stark ladders that have weakly confined states, we have found that tunneling in the continuum states above the structure can play a considerable role in transport, which is not reproducible by EMC. The results for the 2.75 THz and 3.4 THz QCL prove also that every QCL has different amounts of ballistic transport, however when all the scattering rates are included, the transport in the incoherent regime is semiclassical.

Chapter 4

Temperature performance of THz QCLs

Quantum cascade lasers offer a compact approach to coherent generation in the THz regime [9]. The frequency range of 1-10 THz is important for linking optics and electronics as well as many new applications could arise from compact laser sources in this range. For example THz imaging for biological, medical or security applications. Furthermore quality control for drug manufacturing, remote sensing of earth's atmosphere and study of star and galaxy formation as well as detection of concealed drugs explosives or weapons. A good summary of the work that has been done for covering the 'THz gap' has been recently published [9].

One alternative for generating coherent THz radiation are terahertz quantum cascade lasers (QCLs), which since 2001 have been subject to continuous optimization with respect to temperature performance and output power. Particularly, room temperature operation in the terahertz regime has been a long-standing goal. Progress has been made by introducing resonant phonon depopulation (RP) designs [71, 74], reducing the number of wells per device period [75], and by applying copper metal-metal waveguides [74]. Optimizations with respect to the diagonality of the lasing transition resulted in a 3.9 THz QCL operating at a record temperature of 186 K [66]. However, efforts in improving the temperature performance of a similar vertical 3.2 THz structure by introducing some degree of diagonality failed [76]. The goal of this chapter is to clarify these apparently contradicting results and to investigate the role of lasing transition diagonality for the optimization of RP terahertz QCLs with respect to temperature operation.

4.1 Design of THz QCLs

We have designed and analyzed three-quantum-well terahertz QCLs with different degrees of diagonality and frequencies between 1.8 and 4.8 THz. For the self-consistent modeling of QCLs, we have used our

Table 4.1: Overview of the designed THz QCLs. All layer thicknesses are given in angstrom, and bold numbers indicate barriers. The underlined wells are doped with a sheet density of $2.7\times10^{10}\,\mathrm{cm}^{-2}$ in their 55 Å-wide middle region.

Freq.	0% diagonal	30% diagonal	50% diagonal	70% diagonal
1.8 THz	**46**/98/**31**/76/**43**/161	**49**/94/**35**/78/**47**/161	**51**/92/**39**/80/**48**/161	**52**/91/**48**/80/**49**/161
2.3 THz	**48**/95/**27**/73/**42**/157	**51**/90/**31**/77/**46**/158	**52**/89/**35**/80/**47**/159	**52**/88/**42**/81/**48**/160
2.8 THz	**48**/94/**24**/72/**42**/157	**51**/89/**28**/78/**46**/159	**52**/87/**32**/80/**47**/159	**53**/86/**39**/81/**48**/159
3.2 THz	**48**/96/**20**/74/**42**/161	**51**/90/**24**/81/**46**/163	**52**/88/**29**/84/**47**/163	**52**/87/**36**/86/**48**/163
4.1 THz	**47**/99/**15**/73/**40**/164	**51**/88/**19**/83/**44**/164	**52**/86/**23**/87/**45**/164	**53**/85/**32**/89/**47**/164
4.8 THz	**49**/98/**12**/71/**39**/163	**52**/86/**15**/84/**42**/164	**53**/83/**20**/89/**44**/164	**54**/82/**29**/92/**45**/164

semiclassical ensemble Monte Carlo (EMC) simulation tool [28, 25, 31] which we compared to full quantum transport methods [28, 62] in the previous chapter. As discussed in the previous chapters, the EMC simulation tool has been specifically developed for the analysis of QCLs [12, 27], self-consistently including the scattering mechanisms, namely, electron-electron (e-e), electron-longitudinal optical and acoustic phonon, and electron-impurity scattering. Since interface roughness highly depends on the growth process and its exact parameters are difficult to measure, this scattering mechanism is included phenomenologically using typical parameter values [12, 62]. For the design of GaAs/$\mathrm{Al_{0.15}Ga_{0.85}As}$ THz QCLs, barrier heights between 135-150 meV are commonly used [71, 74, 75, 66, 76]. For our simulations we assumed a barrier height of 165 meV, corresponding to 72% conduction band offset [77]. This larger value was utilized to avoid sharp anticrossing of the lower laser level with weakly-bound upper states in the second downstream injector, arising in some of the investigated designs and leading to well-known simulation artifacts [25]. Effective electron masses of 0.067 in the wells and 0.076 in the barriers are assumed. We verified that the observed trends are robust with respect to the assumed barrier heights and interface roughness values.

For our analysis, we have designed QCLs with different degrees of diagonality at various operating frequencies. The degree of transition diagonality between upper and lower laser states is quantified in terms of the oscillator strength f_{osc}, normalized to the value for the corresponding vertical design $f_{\mathrm{osc}}^{\mathrm{vert}}$. Thus, for the vertical structures we have $f_{\mathrm{osc}}/f_{\mathrm{osc}}^{\mathrm{vert}} = 1$, corresponding to a 0% diagonal design. A design with $f_{\mathrm{osc}}/f_{\mathrm{osc}}^{\mathrm{vert}} = 0.7$ is referred to as a 30% diagonal structure, etc. In order to make the simulation results comparable, a special effort was made to keep laser designs very similar. In particular, the upper and lower laser level anticrossing energies with injector states (for injection and extraction, respectively) were kept in the range 1.5-1.6 meV and 3.3-3.6 meV, respectively. If we assume the $\mathrm{Al_{0.15}Ga_{0.85}As}$ barrier height to be 135 meV, these injection/extraction anticrossing energies become 1.95-2.0 meV for the injection anticrossing and 4.25-4.6 meV for the extraction anticrossing, which is in line with the injection/extraction anticrossing values used in current state-of-the-art devices [74, 75, 66, 76]. The energy separations between the upper and lower injector states were kept in the range 37-39 meV in all laser designs. These parameters combined with the desired laser operating frequency and diagonality of the laser transition uniquely define the layer sequence for the structure [75]. The layer thicknesses of the designed structures are summarized in Table 4. Experimentally, the 0% diagonal structures were tested for the 2.3 THz, 3.2 THz, and 4.1 THz

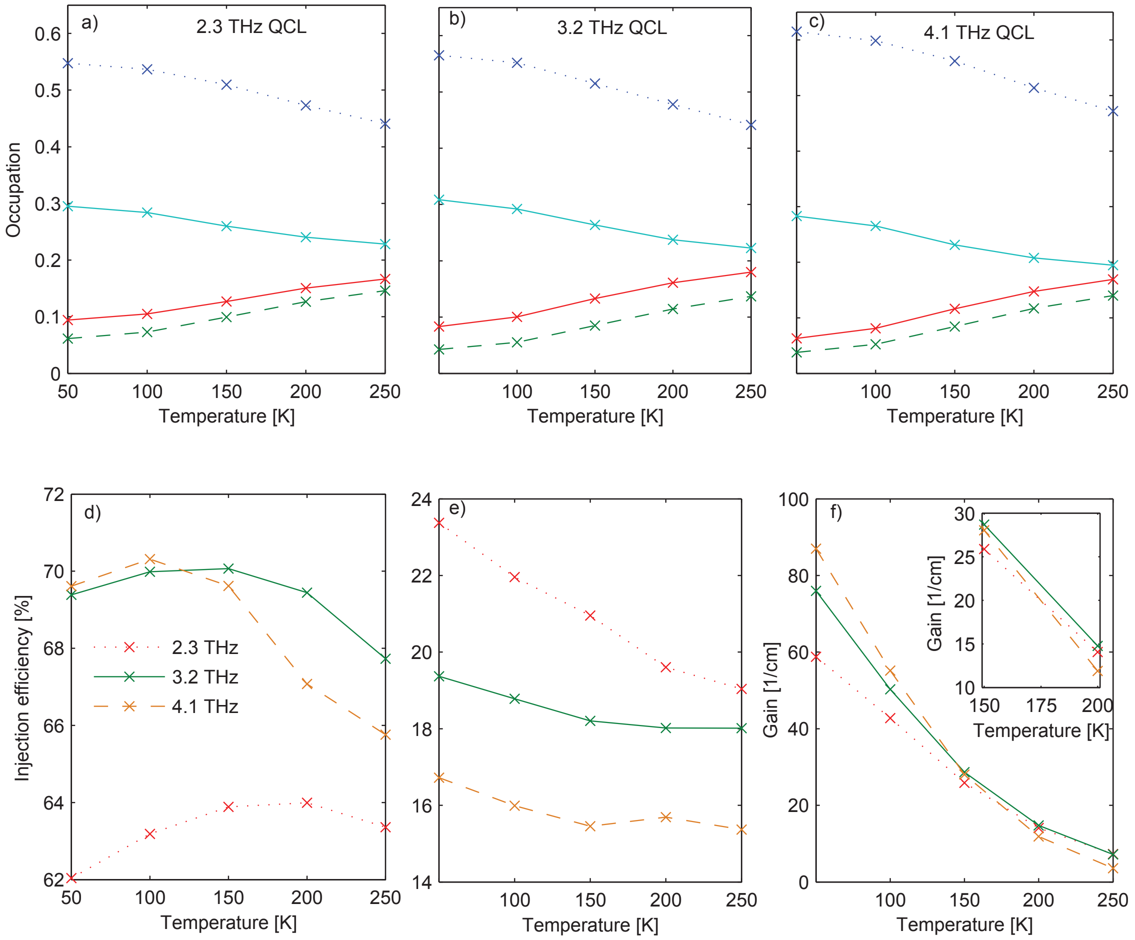

Figure 4.2.1: Occupation of the upper and lower laser level (solid lines), injection level (dashed lines) and ground level (dotted lines) for the a) 2.3, b) 3.2 and c) 4.1 THz structure. Furthermore, the temperature dependence of the d) injection efficiency into the upper laser level, e) parasitic injection efficiency into the lower laser level, and f) gain for the 2.3, 3.2 and 4.1 THz structure is shown. The inset contains a close-up of the gain in the technically relevant temperature range of 150-200 K, clearly showing the superior performance of the 3.2 THz QCL in this temperature range.

designs [76]. Also copper double-metal 3.2 THz QCLs with an active region based on a 30% diagonal transition were tested experimentally. The devices operated up to 174 K [76]. which is lower than the maximum operating temperature of 178 K for similar devices based on a vertical 3.2 THz design [76].

4.2 Temperature performance and frequency

We present simulation results for the structures from Table 4 with 0% diagonality at the frequencies of 2.3, 3.2 and 4.1 THz. The best performing device was operating up to about 174 K at a frequency of 3.2 THz [76, 22]. The three well design THz QCLs discussed in this chapter have four relevant energy states: the upper and lower laser level and the upper and lower phonon depopulation level in the injector well (the underlined wells in Table 4.

In Fig. 4.2.1 (a), (b) and (c), the temperature dependent occupations are shown for these levels.

Solid lines represent the upper and lower laser level, respectively, while the most occupied is the lower LO-phonon depopulation state. At elevated temperatures, all three structures exhibit a reduced upper laser level population and an increased lower laser level occupation, giving rise to a reduced inversion. Notably, the 2.3 THz structure features the lowest degradation with temperature, but also the smallest initial population difference. In contrast, the 4.1 THz QCL has the highest occupation inversion at low temperatures, but the degradation with temperature is also large. The 3.2 THz QCL is between these two cases, explaining the superior THz QCL performance at this frequency.

For a more detailed analysis, we have determined the injection efficiency into the upper laser level and the parasitic injection into the lower laser level, shown in Fig. 4.2.1 (d) and (e). The least efficient injection into the upper laser level and the strongest parasitic injection into the lower laser level is observed for the 2.3 THz QCL. This is a direct result of the close level spacing (reduced lasing frequency), which increases the parasitic coupling between injector and lower laser level. The increased initial population and its strong degradation with temperature for the 4.1 THz QCL is explained by the increased level spacing that favorizes LO-phonon scattering from the upper to the lower laser level. The thermally activated LO-phonon scattering is visible also in the decrease of injection efficiencies for the 4.1 THz structure between 150 and 250 K, while for lower frequency structures the decrease is moderate.

In terms of injection efficiencies, the devices operating at 3.2 and 4.1 THz have similar values, however the 3.2 THz structure has a slightly higher transition dipole (6.1 nm, while the 4.1 THz QCL has 5.8 nm) giving a higher overall gain. These small deviations result in an increase of the maximum operating temperature by a few Kelvins, which is observable experimentally. In Fig. 4.2.1 (f) we show the unsaturated spectral gain for the three structures, where the best performing device is the 3.2 THz QCL, as observed experimentally. The inset shows the technically relevant operating temperature regime between 150 and 200 K.

In summary, low frequency devices are limited by increased parasitic injection into the lower laser level due to the decrease of level spacing. High frequency devices are limited by thermally activated LO-phonon scattering from the upper to the lower laser level due to increased level spacing, which is now closer to the LO-phonon energy for these structures. There is an optimum frequency of around 3 THz, where the tradeoff between parasitic injection and thermal activation is optimum, making these THz QCLs the devices with the best temperature performance in the case of vertical lasing transitions.

4.3 Temperature performance and diagonality

As we go from 0% diagonal to 70% diagonal structures, the wavefunctions get more localized in a single well as shown in Fig. 4.3.1 for the 3.2 THz structure. From the basic perspectives of THz QCL design, the diagonal laser transition is expected to help improve the electron injection efficiency into the upper laser state, suppress electron leakage from the upper laser state to the downstream injector, and reduce the

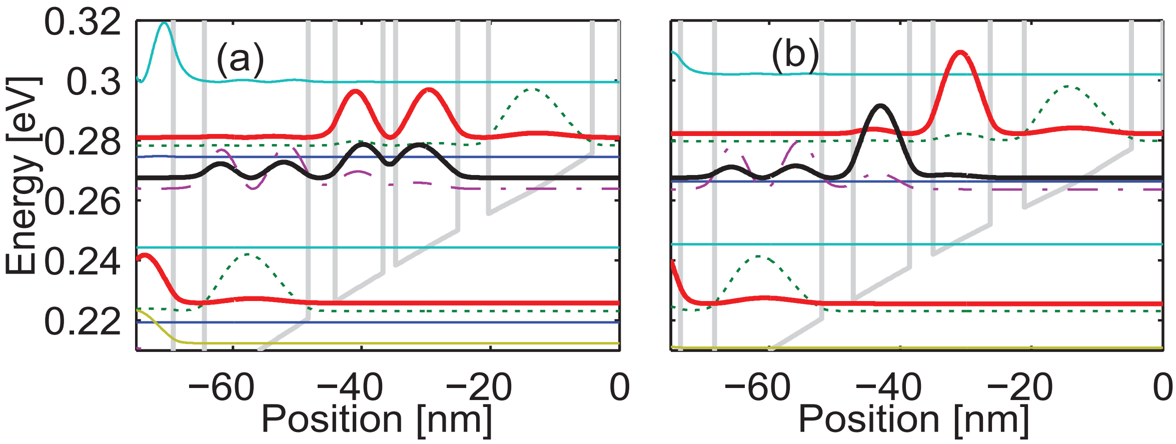

Figure 4.3.1: Conduction band diagram for the 3.2 THz QCL with (a) 0% diagonality and (b) 70% diagonality. Upper and lower laser levels are marked by red and black bold solid lines.

nonradiative electron scattering rate from the upper laser state; however, the diagonal laser transition results in smaller transition dipole moment compared to a vertical transition [66, 76]. One may expect that THz QCL structures based on vertical design may provide higher gain at lower operating temperatures, when electron injection into the upper laser state is efficient and the LO-phonon scattering of thermally excited electrons in the upper laser state [78] is suppressed. However, diagonal transitions may have advantages at higher operating temperatures. Because the parameters of the electron transport (injection efficiencies and lifetimes in various laser states) are difficult to estimate analytically, we use EMC simulations to compare the peak gain of devices with various diagonalities at different temperatures.

Fig. 4.3.2 shows the temperature dependent peak gain for the designed structures in Table 4, as obtained by our EMC simulations. As expected, for increased diagonality, we observe a decreased gain at low temperatures, but also a smaller gain degradation with temperature. At laser lattice temperatures around 150-200 K, representing the currently relevant range for temperature performance optimizations, diagonality does not offer an advantage for the low frequency structures that we studied. Specifically, in case of the 3.2 THz design we see no improvement of the temperature performance for the 30% diagonal as compared to the 0% diagonal structure, which is consistent with experimental observations [76]. For higher lasing frequencies, diagonal designs offer clear advantages. The reason is that when the energy spacing between upper and lower laser level increases towards the LO-phonon energy (36 meV in GaAs), scattering of thermally excited electrons in the upper laser level becomes very strong even at modest temperatures [78], resulting in reduced population inversion and thus a strongly decreased peak gain. This detrimental mechanism is suppressed in diagonal designs, which for high operating temperatures maintain increased population difference outweighing their reduced oscillator strength. For low frequency structures, where LO-phonon scattering of thermally excited electrons between the laser levels is less pronounced, diagonal designs offer an advantage only at higher operating temperatures, where the thermal activation of LO-phonons is stronger. Thus, for the currently reached operating temperatures [76, 66],

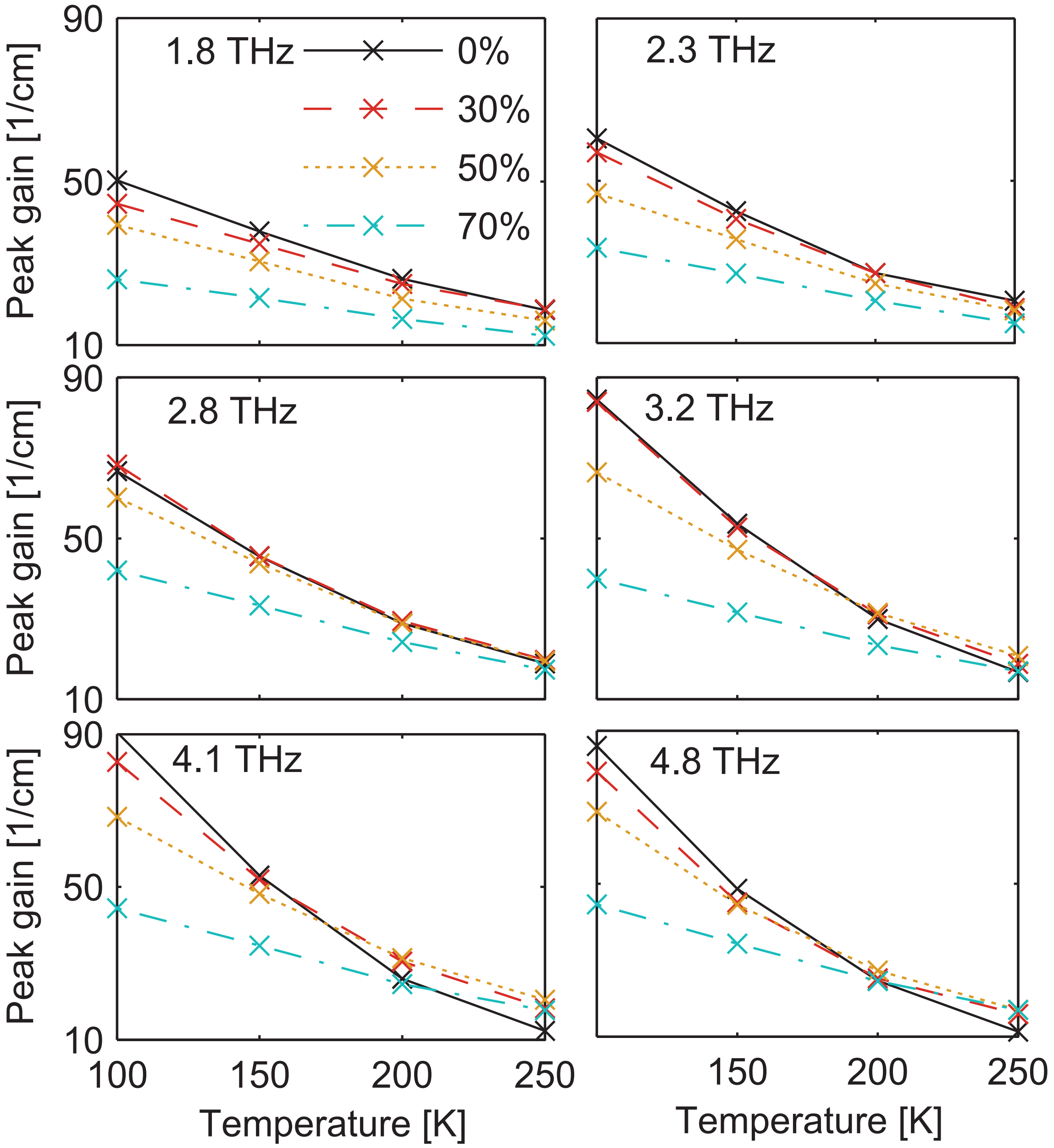

Figure 4.3.2: Dependence of the peak gain on the active region lattice temperature for different operating frequencies and diagonalities. The shown results are for optimum bias, which only weakly depends on temperature and has for each structure been determined at 150 K as to yield maximum gain.

we find improvements in peak gain only for designs operating above approximately 3.5 THz.

For additional details on our simulation results, we show in Fig. 4.3.3 the population inversion Δn between the upper and lower laser level and gain bandwidth Δf (full width at half maximum) at maximum gain, for 2.3 THz and 4.1 THz structures of different diagonalities. We note that the peak gain scales with $f_{\mathrm{osc}}\Delta n/\Delta f$. Overall, the 2.3 THz structures (Fig. 4.3.3 (a)) exhibit a higher Δf in our simulations than the 4.1 THz designs (Fig. 4.3.3 (b)), which is mainly due to increased Coulomb scattering as well as IR

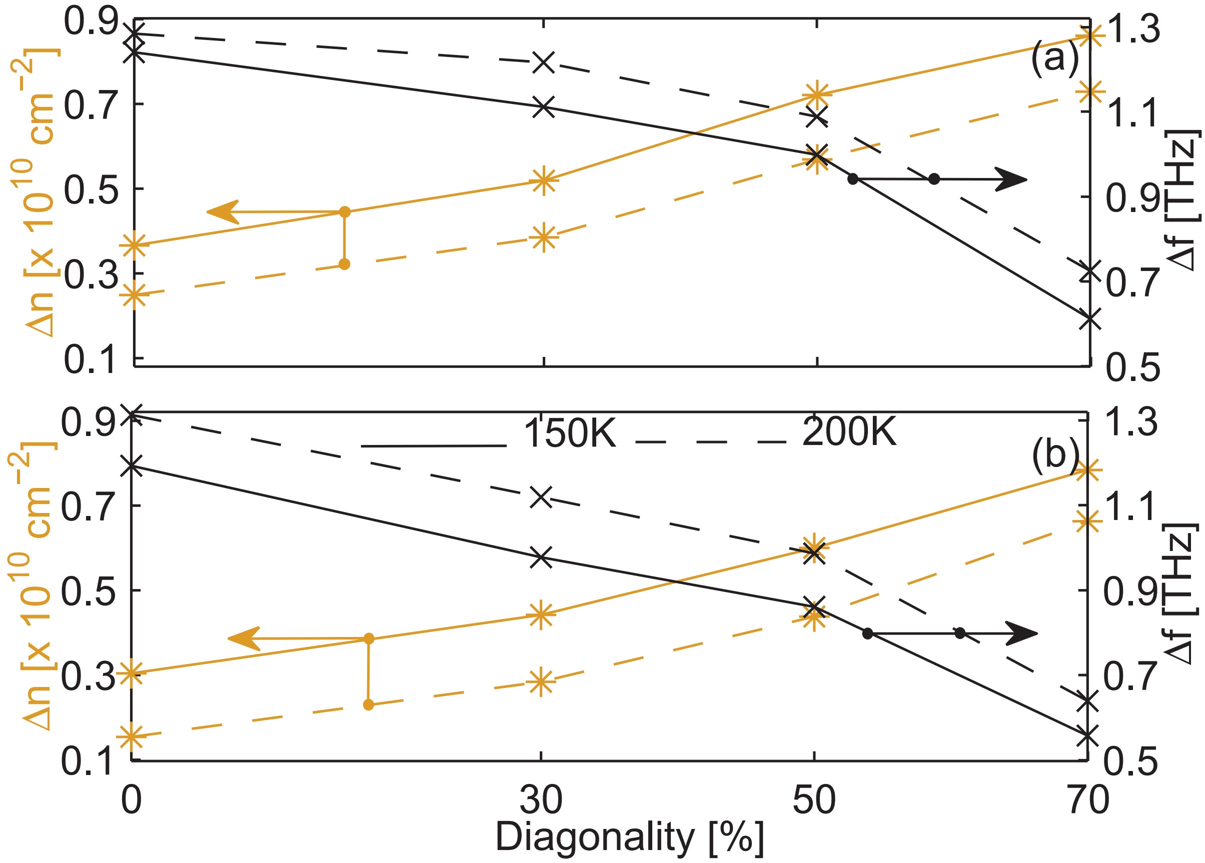

Figure 4.3.3: Δn and Δf for different degrees of diagonality for the (a) 2.3 THz QCL and (b) 4.1 THz QCL at lattice temperatures of 150 and 200 K, respectively. The bias is chosen as to maximize the peak gain.

scattering for these structures. Higher Δn and, to a lesser extent, smaller Δf of more diagonal designs overcompensate the reduction of f_{osc} in case of the 4.1 THz structures, however not for the 2.3 THz QCLs. For both structures, a decrease of Δf with increasing diagonality is observed. The gain broadening is related to scattering events involving the laser levels. For diagonal lasing transitions, all the contributions get reduced except for IR scattering, which may go up or down. Furthermore, we observe an increase of Δf with temperature, which is due to enhanced LO-phonon scattering.

The effect of diagonality d is further investigated by introducing the relative quantities $\Delta n_{\mathrm{rel}} = \Delta n(d)/\Delta n(0\%)$ and $\Delta f_{\mathrm{rel}} = \Delta f(d)/\Delta f(0\%)$. In Fig. 4.3.4 we plot Δn_{rel} and $\Delta f_{\mathrm{rel}}^{-1}$ as a function of temperature for $d = 30\%$ (Fig. 4.3.4 (a)) and $d = 50\%$ (Fig. 4.3.4 (b)). Comparing Fig. 4.3.4 (a) to (b), we find that Δn_{rel} increases with temperature. This trend is most pronounced for 4.1 THz devices with 50% diagonality. Very little change of $\Delta f_{\mathrm{rel}}^{-1}$ in the temperature range shown in Fig. 4.3.4 indicates that diagonal structures at elevated temperatures mainly profit from improved inversion. Finally, Fig. 4.3.4 clearly shows that diagonal designs offer a much stronger improvement in inversion for the 4.1 THz QCLs than for the 2.3 THz structures.

To investigate the robustness of our results, simulations with a fixed lasing transition linewidth (of

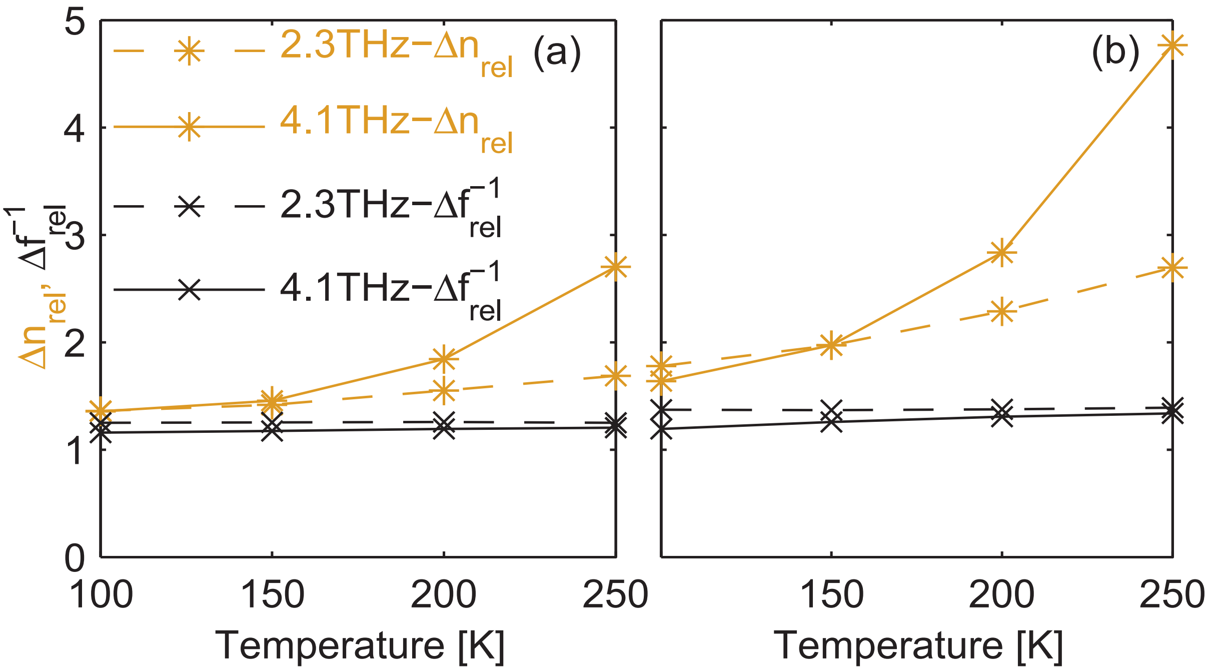

Figure 4.3.4: Temperature dependence for (a) 30% diagonality and (b) 50% diagonality of the relative inversion Δn_{rel} and relative inverse linewidth $\Delta f_{\mathrm{rel}}^{-1}$. The peak gain improvement is $\propto \Delta n_{\mathrm{rel}} \Delta f_{\mathrm{rel}}^{-1}$.

1 THz) were performed (not shown). They confirm the previously obtained trend of the spectral peak gains for the different structures. We find that for the case of a fixed linewidth, the gain improvement for diagonal designs is only slightly reduced.

4.4 Robustness with respect to interface roughness

We have doubled the interface roughness mean height from 1.2 to 2.4 Å, to check the generality of our results with respect to different material quality. We find the same message to be valid for increased interface roughness, as shown in Fig. 4.4.1. Here we see a reduction of gain with the increase of interface roughness (top figures). Furthermore, the optimum amount of diagonality for high frequency structures changes with interface roughness, thus it must be chosen carefully. For higher interface roughness, diagonality should be somewhat decreased to suppress the interface roughness scattering. All in all the curves are relatively close, meaning that these optimizations would change the maximum operating temperature only by a few Kelvin.

4.5 Summary

We have designed three-quantum-well THz QCLs at various frequencies featuring different degrees of diagonality, and analyzed the benefits of diagonal laser transitions for high temperature operation. The

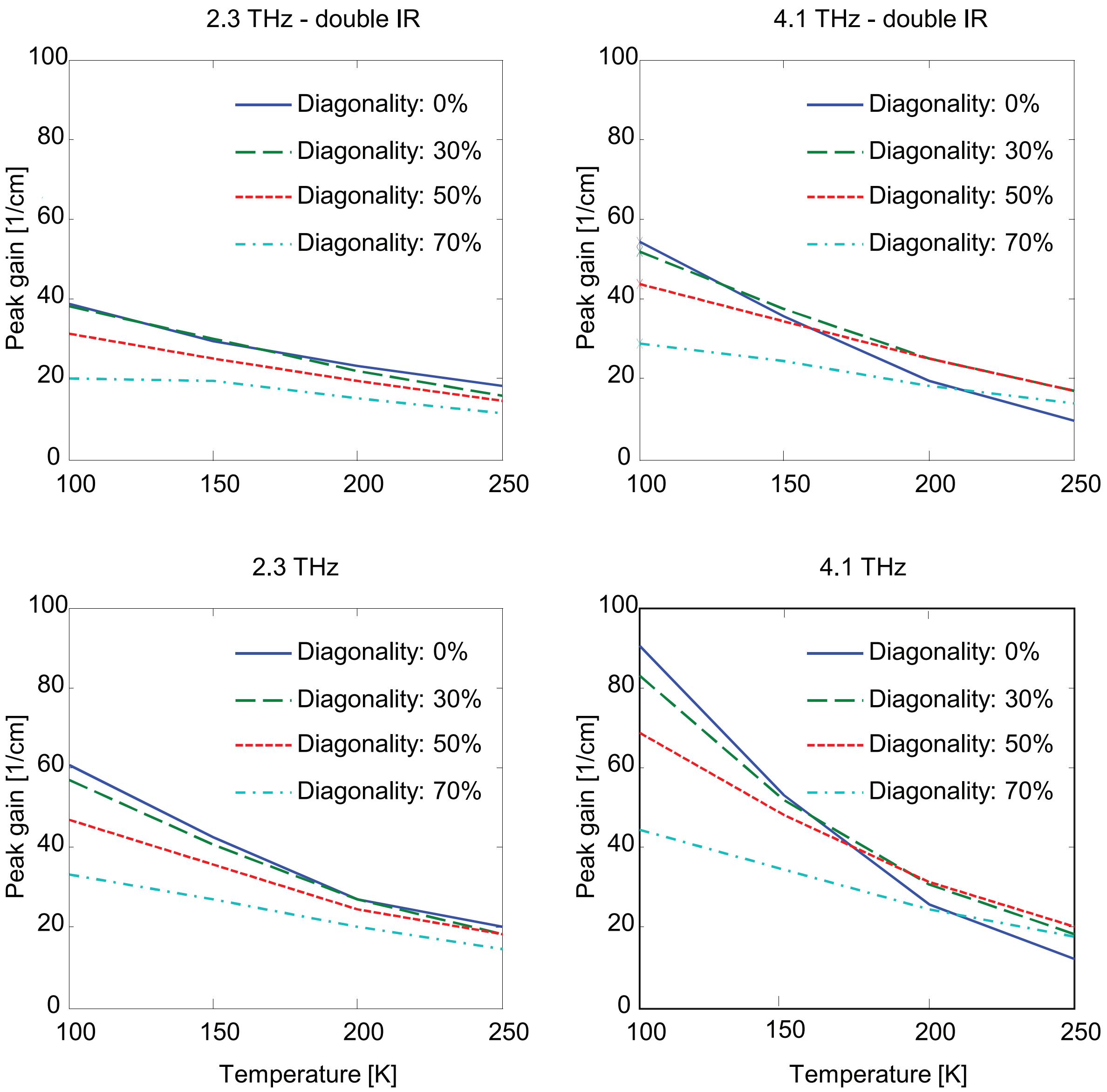

Figure 4.4.1: Peak gain of the simulated 2.3 THz and of the 4.1 THz QCLs with different diagonalities. The top figures were calculated with 2.4 Å interface roughness mean height, while the bottom plots correspond to our published results also shown in Fig. 4.3.2 (mean height of 1.2 Å and correlation length of 100 Å).

relatively good performance of vertical transition (0% diagonal) QCLs around 3 THz is explained by an interplay between parasitic injection in the lower laser level and LO-phonon emission between the lasing states. The former limits low frequency structures, while the latter gives a limit for high frequency QCLs. We find that the main advantage of diagonal structures is the considerably increased inversion; additionally, the reduced gain bandwidth of diagonal transitions is beneficial. These effects can outweigh the reduced oscillator strength and provide advantage in QCL temperature performance when diagonality is considered. For designs operating above approximately 3.5 THz, we find that diagonal structures offer advantages at operating temperatures already below 200 K. For lower frequencies the advantages offered by diagonal designs become relevant only at operating temperatures of 200-250 K or higher. These simulation results provide a basis for a further optimization of the temperature performance of terahertz QCLs.

Chapter 5

Modeling of mid-infrared quantum cascade lasers

We have specifically adapted the material parameters and the EMC code for the simulation of InGaAs-based mid-infrared (MIR) QCLs in this thesis. Since MIR QCL structures often reach a considerable wall-plug efficiency (WPE) and output power, we investigate the effects of the stimulated electronic processes on transport as well as the influence of the various scattering mechanisms. Furthermore we show that at various wavelengths EMC can well reproduce experimental results. The validation of our EMC solver against THz QCLs in Chapter 3 and Chapter 4 and infrared QCLs in this chapter will offer the possibility to model complex structures. One example would be difference-frequency generation of terahertz radiation which is a long standing goal.

5.1 Short injector QCL operating at 8 μm

In the following, we employ our self-consistent EMC simulation tool for the analysis of a short-injector mid-IR $\mathrm{In}_{0.6}\mathrm{Ga}_{0.4}\mathrm{As}/\mathrm{In}_{0.365}\mathrm{Al}_{0.635}\mathrm{As}$ QCL [56]. Such short injector and injectorless indium-based MIR QCLs are among the most efficient structures up to date, having high wall-plug efficiencies, emitting more light than heat in special cases [7] and easily providing watt level output powers at room temperature [79]. We discuss the role of the various scattering mechanisms and investigate the influence of non-parabolicity for the calculation of the subband energies and wave functions. We also model the carrier-light coupling in the structure and self-consistently calculate the QCL output power [33], and identify mechanisms which limit the obtainable output power. Our EMC simulation tool has proven of value for the simulation of THz QCLs [24, 12], and has been extended to account for effects relevant in MIR structures.

5.1.1 Effects included in the simulation

Scattering mechanisms included are electron (e)-longitudinal optical phonon interactions including hot phonons, as well as e-acoustic phonon, e-impurity, e-interface roughness, e-e and e-alloy scattering. All scattering mechanisms are self-consistently implemented, only using established material parameters [80] with scattering rates given by Fermi's golden rule. Since the exact values of the interface roughness parameters are not well known and depend on the growth conditions, we have measured the interface roughness indirectly from photoluminescence measurements at liquid nitrogen temperature and found a related scattering lifetime of 60 fs. In our simulations we used the interface roughness parameter values of Δ=0.06 nm and Λ=17 nm to explicitly reproduce this measured value and account for the product of $\Delta\Lambda \approx 1\,\mathrm{nm}^2$ given in [81, 82]. The EMC tool is coupled to a Schrödinger-Poisson solver which delivers the subband energies and wave functions [27]. Band non-parabolicity has been included to correctly account for the energetic level separation in the device, which is needed for the accurate calculation of the current-voltage (I-V) curves. Non-parabolicity is known to change the higher lying states in a heterostructure. For an appropriate implementation, we also corrected the non-parabolicity parameter by the split-off energy [37]. In our implementation, the temperature dependence of the non-parabolicity parameter enters via the temperature dependent bandgap. To account for alloy scattering in the investigated material system, we have added e-alloy scattering in the random alloy approximation [42] as derived in Section 2.3.7. The used scattering potentials were 420 meV and 500 meV in the wells and barriers respectively [83], which only depend on the type of the alloy materials but not their concentrations. For LO-phonon scattering, we took into account only InAs-like phonons, since the GaAs- and InAs-like LO-phonon energies (33 meV and 29 meV, respectively) are relatively close together [84].

5.1.2 Role of the scattering mechanisms

Room temperature results are shown for the short injector $\mathrm{In}_{0.6}\mathrm{Ga}_{0.4}\mathrm{As}/\mathrm{In}_{0.365}\mathrm{Al}_{0.635}\mathrm{As}$ mid-IR structure emitting at 8 μm [56]. The QCL consists of 64 periods in the active region; both facets are uncoated. Measurements were performed in pulsed mode.

Current-voltage curves for the present QCL were explicitly measured by growing the device without active region to account for the voltage drop at the contacts. We have performed EMC simulations for different bias points and have compared the obtained current-voltage characteristics and the optical output power to experiment. First we assess the importance of the different scattering mechanisms for the investigated structure. We evaluate their contributions to the current by switching off one type of scattering at a time in our simulations. LO-phonon scattering, which governs the carrier transport in the simulated QCL, is always taken into account. As shown in Fig. 5.1.1, interface roughness scattering plays an important role for the current, and a moderate influence of alloy scattering is also observed. Alloy scattering is found to be more important at higher biases, especially in the lasing region. Interestingly, Coulomb interactions, i.e., e-e and impurity scattering, practically do not contribute to the current, in

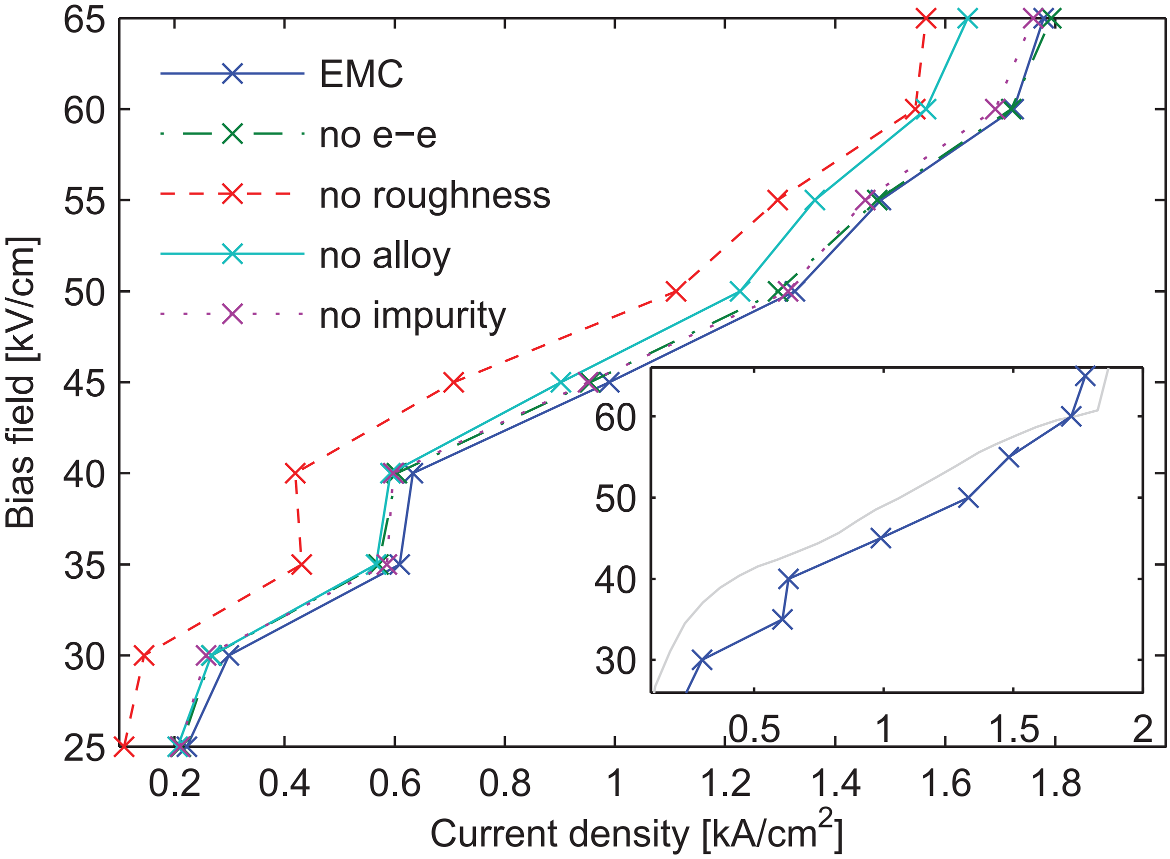

Figure 5.1.1: EMC simulation results for the current-voltage characteristics. We observe a large effect of interface roughness and also an influence of alloy scattering on the total current, while e-e scattering and impurity scattering can be practically neglected. A comparison to experiment is shown in the inset, where we find qualitative agreement between EMC and the experimental result.

contrast to GaAs/Al$_{0.15}$Ga$_{0.85}$As THz QCLs [29]. As shown in the inset of Fig. 5.1.1, we find good agreement for the EMC and experimental currents, however these simulations were done without taking into account carrier-light coupling. We note that stimulated photon emission and absorption events lead to an increased current in the lasing region as discussed further below [33], which can exceed the experimentally measured value. On the other hand, preliminary simulations indicate that an inclusion of lifetime broadening of the energy levels in EMC carrier transport simulations would result in a somewhat reduced current, counteracting this effect.

In Fig. 5.1.2, the influence of the various scattering mechanisms on the unsaturated spectral gain profile is investigated, i.e., carrier-light coupling is neglected here. We choose a bias of 60 kV/cm, yielding the maximum gain in our simulations. Also the experimental measurements indicate that this is close to the optimum bias, since the onset of the negative differential region occurs slightly above this point (see Fig. 5.1.1). Again we switch off one of the scattering mechanisms at a time and compare the result to the reference gain profile, obtained by the full EMC simulation. As shown in Fig. 5.1.2, interface roughness scattering is very important, significantly reducing the peak gain and increasing the gain bandwidth.

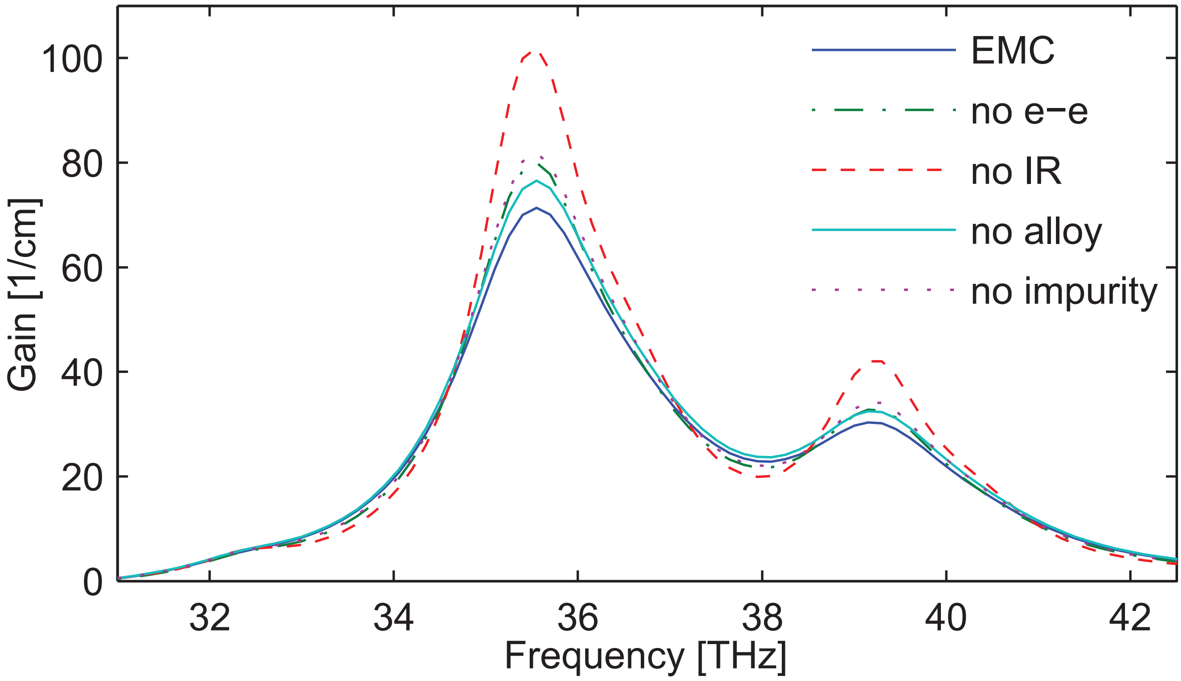

Figure 5.1.2: Influence of the different scattering mechanisms on the spectral gain profile. The result of the full EMC simulation is indicated by the bold solid line. The narrow solid, dashed, dotted and dash-dotted lines corresponds to the cases where we switch off alloy, interface roughness, impurity and e-e scattering, respectively. We see that interface roughness scattering leads to a significant reduction of the gain.

Surprisingly the influence of alloy scattering on the spectral gain, as shown by the narrow solid line, is much smaller than on the current. The influence of e-e and impurity scattering on the gain is moderate. We conclude that gain broadening is mainly due to LO-phonon scattering as the dominant scattering mechanism and interface roughness scattering, while impurity and e-e scattering have secondary effects. Alloy scattering mainly gives rise to parasitic effects which get stronger above the threshold current, however it has no direct influence on the gain spectra for the present device. We observe a slight discrepancy ($0.4\,\mu$m) between the position of our gain maximum and the measured lasing wavelength. This might be partially due to the uncertainty of the parameters used in our simulations or the effective mass approach which is not as accurate as a full $\mathbf{k}\cdot\mathbf{p}$ analysis.

5.1.3 Carrier-light coupling

We have also performed coupled carrier-field simulations, allowing us to calculate the output power. The results are compared to experiment, as shown in Fig. 5.1.3. Simulations have been performed by fixing the lasing frequency to $8.04\,\mu$m, as experimentally measured [56]. The waveguide and mirror loss is $15.6\,\mathrm{cm}^{-1}$ and $3.2\,\mathrm{cm}^{-1}$, respectively, and the confinement factor is $65\,\%$; for the refractive index, we use the value 3.22. As shown in Fig. 5.1.3, we get good agreement for the output power as a function of the applied bias. The discrepancies at higher biases can be explained by the uncertainties of the exact device parameters as well the onset of the negative differential region. Above $60\,\mathrm{kV/cm}$, we observe relatively

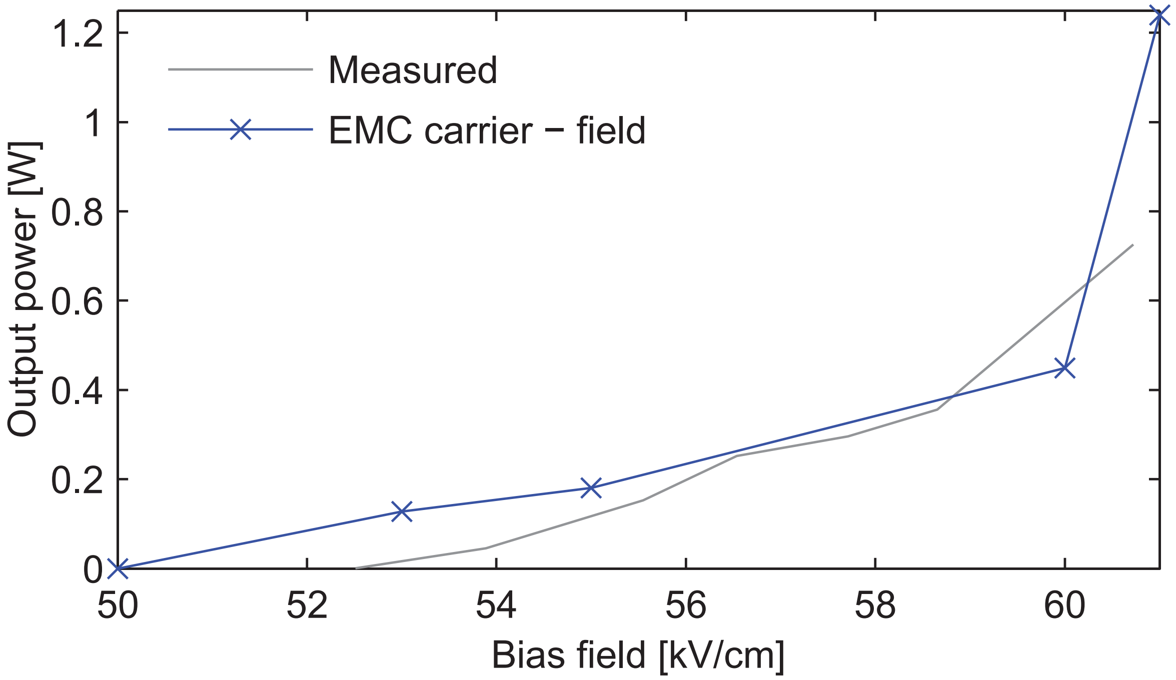

Figure 5.1.3: Output power calculated from the EMC method and compared to experiment. Simulations were performed by fixing the lasing frequency to 8.04 μm. We observe a good agreement for the output power at various bias points.

high output powers in the simulation, as shown in Fig. 5.1.3. However, such high bias values are already close to the onset of the negative differential resistance regime (see inset of Fig. 5.1.1), which is electrically unstable in experiment.

In Fig. 5.1.4, we show the influence of photon-induced scattering on the current density. Here we clearly observe an increase of the current above threshold, since photon-induced scattering events contribute significantly to the total current in the device. The high current density value above 60 kV/cm for carrier-light coupling included is a consequence of the high output powers obtained in the simulation (see Fig. 5.1.3), and are not relevant for the comparison with the experiment as discussed above.

5.2 High wall-plug efficiency QCL operating at 5 μm

Recently QCLs with wall-plug efficiencies (WPEs) of around 50% were reported for the first time [6, 7]. In such structures, light emission and absorption are not only relevant with respect to the generated optical power, but also strongly affect the carrier transport in the devices. In fact, for the low temperatures where these high efficiencies are reached, the photon-induced processes dominate over the other scattering mechanisms. Thus, to adequately model the operation of these lasers, the optical cavity field has to be considered in the simulation. While this is routinely done in one-dimensional simulations [85, 86, 87, 88], the cavity field is usually neglected in fully three-dimensional (3-D) approaches like the ensemble Monte-Carlo (EMC) [30], non-equilibrium Green's functions (NEGF) [17, 19] or 3-D density matrix [89, 90]

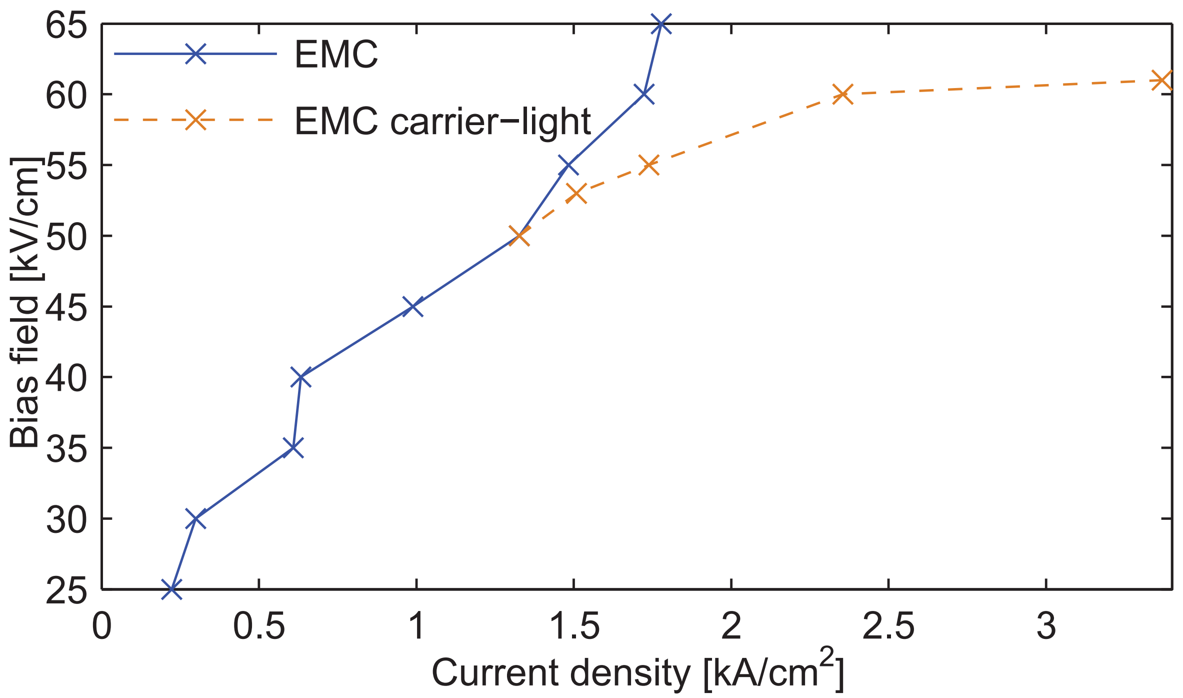

Figure 5.1.4: Current-voltage characteristics with (dashed line) and without (solid line) electron-photon scattering events included.

method. However, such 3-D simulations, where the in-plane carrier dynamics is explicitly considered, do not only yield level occupations, but also the kinetic carrier distributions within these levels. Here, we employ the EMC method, which has been intensely used to investigate the carrier transport in both MIR [30, 32, 64, 91, 92, 93] and THz [94, 25, 31, 24, 95, 22] QCLs. EMC uses self-consistent coupled simulations of the carrier transport and the optical cavity field [33]. The EMC method is a semiclassical approach, i.e., quantum correlations are neglected in contrast to NEGF as discussed in Chapter 3.

The goal of this section is to analyze the carrier transport and lasing operation in MIR QCLs [7], with a particular focus on the influence of photon-induced scattering. Specifically, we show that the inclusion of light emission and absorption in the simulation is crucial to obtain a realistic description of such devices. Furthermore, our analysis provides insight into the carrier dynamics on a microscopic level, for example the kinetic electron distributions in the upper and lower laser level which are hardly accessible to experimental observation.

5.2.1 Effects included in the simulation

All the relevant mechanisms like electron (e)-longitudinal optical (LO) and acoustic phonon, e-interface roughness, e-impurity and e-e scattering are routinely considered in our simulation tool [12, 11]. Moreover, various effects relevant for MIR QCLs based on the InGaAs/InAlAs material system have been added. We have included random alloy scattering [96], with a scattering potential of 0.3 eV reported for high indium content InGaAs [97]. Furthermore, we account for InAs- and GaAs-like phonons, using their composition dependent values for the phonon energy [84]. The scattering rates are weighted by the concentration of the individual materials (InAs and GaAs). The influence of the AlAs-like branch is believed to be negligible in QCL structures [98]. Here, the bulk phonon approximation is adopted, which was shown to be a valid approach for the simulation of such QCL structures [92].

The (parallel and perpendicular) effective masses have been implemented considering strain [99] and non-parabolicity. Our implementation of non-parabolicity is based on the approach developed by Ekenberg. Non-parabolicity parameters were determined from the material bandgap [37], using temperature dependent values [80]. In the InGaAs material system, the parallel non-parabolicity is enhanced by a factor of 1.7 as compared to the perpendicular value [100]. The perpendicular effective mass affects the subband energies and wavefunctions, as considered in our Schrödinger-Poisson solver [27]. The parallel effective mass is accounted for by assigning a different value to each subband, affecting the scattering rates in the EMC solver. Here we focus on simulations at a lattice temperature of 40 K where the investigated structure operates with a record wall-plug efficiency of above 50% [7]. At such low temperatures, the kinetic electron energies are still moderate, whereas for room temperature operation, a more complex implementation of non-parabolicity might be required, e.g., based on $\mathbf{k}\cdot\mathbf{p}$ theory [64, 91, 92]. Furthermore, at low temperatures, the electron leakage into indirect valleys, not considered in our simulations, is very small [64, 91].

The interface roughness is typically described by a mean height Δ and a correlation length Λ. In contrast to the well-known bulk material parameters, this quantity is hardly accessible to experimental measurement and depends critically on the growth conditions. Thus, there is an uncertainty regarding the values of Δ and Λ [101, 12]. However, experimental data indicate that $\Delta\Lambda \approx 1\,\mathrm{nm}^2$ for the InGaAs/InAlAs structures [81, 82], reducing the uncertainty to a single parameter value. We choose $\Delta = 0.06\,\mathrm{nm}$, which yields the best agreement with the experimental results and which was also used in the previous section for the QCL emitting at $8\,\mu m$. This value is somewhat lower than previously used values for strain-free lattice-matched structures [81, 102]. However, we note that vertical correlations, which are not considered in our simulations, can reduce the effect of interface roughness for strained (e.g., strain-balanced) quantum cascade lasers [81], as considered here.

Lasing is implemented based on a recently published approach, treating the photon dynamics in terms of classical intensity evolution equations and accounting for photon-induced scattering in the EMC solver [33, 103]. In this way we can self-consistently describe the coupled carrier-light dynamics due to absorption as well as stimulated and spontaneous emission. For the investigated design operating at 5 μm [7], the mirror loss, which amounts to $6.4\,\mathrm{cm}^{-1}$ for a 2 mm long structure, dominates the waveguide loss, which is about $0.5\,\mathrm{cm}^{-1}$ for such cavities [55]. The confinement factor was chosen to be 0.8 as found for a similar design [55]. For our simulation, we use 1200 longitudinal modes in the frequency range between 50 and 80 THz, corresponding to a Fabry-Perot mode spacing of 25 GHz.

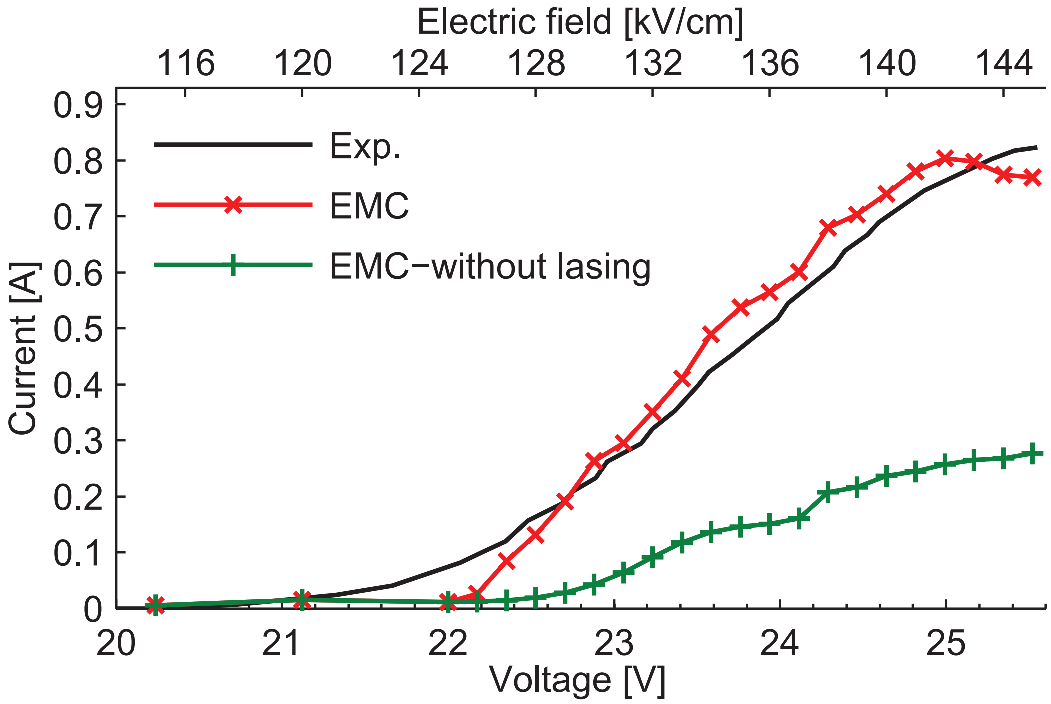

Figure 5.2.1: Current-voltage characteristics. The EMC simulation results with (X marks) and without (crosses) lasing included are compared to available experimental data [7] (solid curve). The electric current is governed by stimulated photon emission and absorption processes, as has to be expected for a WPE as high as 50%.

5.2.2 Wall-plug efficiency, output power, IV curves: comparison to experiment

Results are presented for a recently fabricated high efficiency QCL operating at 5 μm. The simulations were performed at a lattice temperature of 40 K, where the record WPE of 53% was observed [7].

In Fig. 5.2.1, we compare the current-voltage characteristics provided by EMC simulations to experiment. The simulations were performed at biases ranging from 115 kV/cm to 145 kV/cm. For comparison to experiment, these were converted to the voltage points in Fig. 5.2.1, by considering 80 stages with a thickness of 22.1 nm each [7]. Above threshold, good agreement is found if lasing is included, while the current due to non-radiative processes (EMC without lasing) is lower by a factor of almost 3 than the experimentally measured current. This shows that stimulated processes become more and more important for a correct description of the carrier transport as the WPE of QCLs is improved. On the other hand, the spontaneous photon emission rates in our simulation are far too low to affect the carrier transport, which is in agreement with theoretical considerations [104]. The onset of the negative differential resistance (NDR) regime agrees well, occurring at 25.1 V for the EMC with lasing included and 25.6 V in the experiment. For low fields where the energy levels are not aligned, the simulation underestimates the experimentally observed current. Here, the scattering-induced transport is not efficient, and the remaining current can likely be attributed to coherent low-field transport which is not included in the

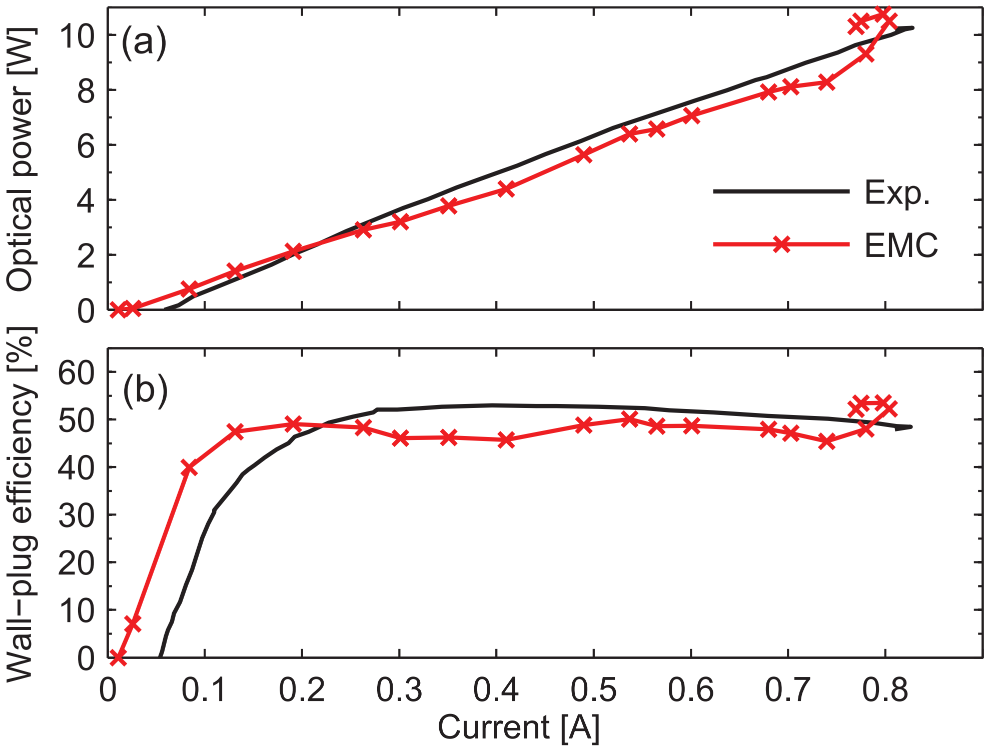

Figure 5.2.2: (a) Current-optical power and (b) current-WPE characteristics. The EMC simulation results with lasing included (X marks) are compared to available experimental data[7] (solid curve).

EMC simulation [14] as discussed in Chapter 3. For design optimization with respect to the WPE, the parasitic channels should be suppressed and the stimulated emission into the lasing modes maximized. Such a task can only be performed with an approach taking into account the optical cavity field.

In Fig. 5.2.2 (a) and (b) we compare the simulated and experimental current-output power and current-WPE characteristics. In the EMC simulation, the bias dependent WPE η_{WPE} is computed as $\eta_{\mathrm{WPE}} = P_{\mathrm{opt}}/P_{\mathrm{el}}$. Here, P_{opt} is the simulated optical power emitted through both facets as in the experiment [7], and the electric power P_{el} is the product of the applied voltage and the simulated electric current. The simulated and experimental current-output power characteristics in Fig. 5.2.2 (a) show excellent qualitative and quantitative agreement. The maximum emitted optical power is about 10 W, which is in both cases obtained around the onset of NDR, where the current reaches its maximum value of 0.8 A. For higher biases, i.e., in the NDR regime, the simulated optical power and electric current get reduced again. The simulated threshold current is lower than the experimental value since we believe that transport is coherent in the given region. Also the simulated and experimental current-WPE characteristics shown in Fig. 5.2.2 (b) agree well. Particularly, the maximum simulated WPE of 49% below the onset of NDR compares very well to the experimental value of 53%. The simulated high WPE value of 53.5% around the onset of NDR is not observed in the experiment, which we attribute to the fact that the operation in the NDR region is unstable due to domain formation [105, 106].

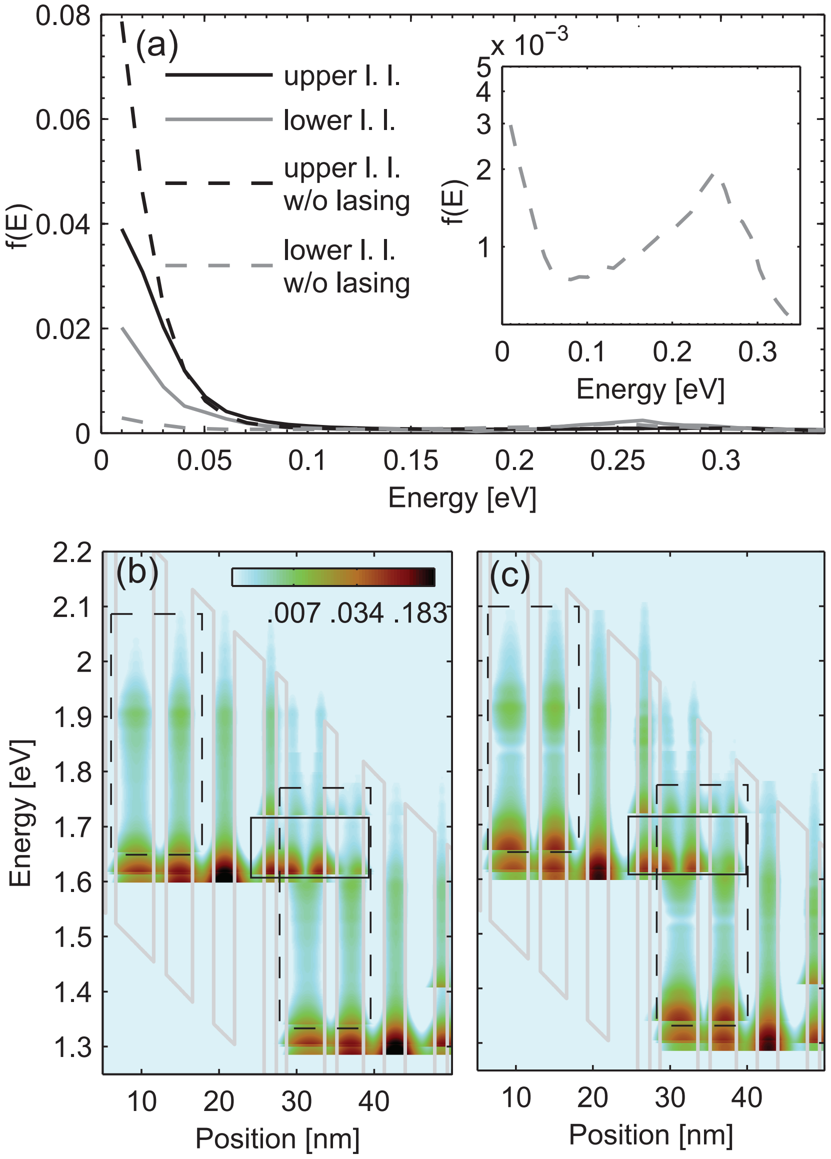

Figure 5.2.3: (a) Simulated kinetic electron distribution $f(E)$ in the upper and lower laser level with and without lasing included. (b) Energy resolved electron density without lasing included; (c) energy resolved electron density with lasing included. The upper laser levels are marked by solid rectangles, and the lower laser level is marked by dashed rectangles.

5.2.3 Kinetic carrier distribution

Full k-space three-dimensional simulation approaches like EMC can yield information on the microscopic level, which is hardly accessible to experimental observation. In the following, we investigate the intrasubband kinetic carrier distributions. These can be characterized by corresponding electron temperatures only in the case of quasi-thermal equilibrium within the subbands, corresponding to a Maxwellian distribution for low doping. The kinetic electron distribution in the upper and lower laser level is shown in Fig. 5.2.3 (a). The bias is 25.1 V, where the simulated current and output power reach their maximum values. We note that for this bias, optical transitions from two upper levels contribute significantly to lasing. For simplicity, we restrict our discussion to one of these states, since the kinetic electron distribution function is found to be similar for the other level. The carrier distributions in the laser levels change significantly by taking lasing into account (solid curves), as compared to the case without lasing (dashed curves). The lasing action leads to a depletion of the upper laser levels and a filling of the lower laser level, corresponding to the effect of gain saturation. In the inset of Fig. 5.2.3 (a), the electron distribution in the lower laser level without lasing is shown on a logarithmic scale, i.e., a Maxwellian distribution would produce a straight line. The distribution is highly non-Maxwellian with an additional peak at around 250 meV, corresponding to the energy spacing between upper and lower laser level. This bump stems from nonradiative transitions from the upper laser level, mainly LO-phonon scattering as the dominant nonradiative mechanism. The energetic extension of the bump is partly due to the kinetic electron distribution in the upper laser level and the finite phonon energies of 29.5 meV and 32.2 meV for the two LO-phonon branches considered here. E-e scattering, which is the predominant intrasubband scattering mechanism, is unable to thermalize the intrasubband carrier distribution strongly enough to suppress the bump [30, 63]. The inclusion of lasing action leads not only to a filling of the lower laser level, but also to a more thermalized kinetic electron distribution, while the bump at around 250 meV still persists. A least square fit produces an electron temperature of $T_\mathrm{e} = 314\,\mathrm{K}$ (upper laser level) and $T_\mathrm{e} = 344\,\mathrm{K}$ (lower laser level) with lasing included. This is consistent with the observation that in strain compensated structures the electronic temperature is clearly above the lattice temperature [107, 87].

In Fig. 5.2.3 (b) and (c), the energy resolved electron density (normalized to its maximum value) is shown without and with lasing included, again for a bias of 25.1 V. For the two quantum wells located between 6 nm and 18 nm, the upper laser level is omitted, so that the high-energy bump discussed in the previous paragraph, here located at around 1.9 eV, is clearly visible. By comparing Fig. 5.2.3 (b) and (c), we can observe the changes in the energy resolved electron density for the laser levels without and with lasing included. The high-energy tails of the kinetic electron distributions remain basically unaffected. In particular, the additional high-energy peak for the lower laser level appears also if lasing is accounted for.

We have also successfully tested our approach for a different high efficiency QCL design [6] using the same material parameters, again finding good agreement with experiment.

5.3 Summary

We have closely compared current-voltage and output power results of a semiclassical EMC method to experimental measurements and found qualitative agreement for two different MIR QCL. We identify the importance of LO-phonon, interface roughness and alloy scattering for the carrier transport and gain of MIR QCLs. The qualitative agreement of our simulations to the experimental measurements suggests that self-consistent EMC methods are valuable for the optimization of InGaAs-based MIR QCLs close to the lattice match point of the InP substrate.

Based on a self-consistent EMC carrier transport simulation including the optical cavity field, we have analyzed the effect of photon emission and absorption on the carrier transport in a high WPE quantum cascade laser. In the regime where efficient lasing is obtained, we find that the inclusion of photon-induced scattering is crucial for the correct calculation of the device current. Furthermore, a comparison to experimental data yields very good agreement for the optical output power and WPE. An analysis of those quantities, as also needed for design optimization, is only possible with an approach which includes both the carrier transport and the optical cavity field. The EMC method also enables us to investigate microscopic quantities such as the intrasubband kinetic carrier distributions, hardly accessible to experiment. We observe strong deviations from an equilibrium distribution especially for the lower laser level, where a high-energy peak in the electron distribution is found, caused by parasitic transitions from the upper laser level. The upper and lower laser level carrier distributions are strongly affected by the lasing action and approach each other, corresponding to gain saturation. Our results show that the chosen method is well suited to model high efficiency MIR QCLs on a qualitative and quantitative level, and to analyze the laser operation on a microscopic level which is hardly accessible to experimental observations.

Chapter 6

Quantum corrections in EMC

In Chapter 3, we have compared semiclassical and fully quantum mechanical theories and found minor deviations. In the 'conventional' EMC method, Fermi's golden rule is used for evaluating the scattering rates, where we have no broadening of the initial and final energetic levels. Here, we would like to extend our EMC method to account to some degree for quantum mechanical effects. This is performed by applying a correction, so that we include the finite linewidth for the initial and final energies in the evaluation of scattering rates. A full quantum mechanical simulator also considers this effect, since there the energy levels have a finite and self-consistently calculated linewidth resulting from the scattering in the device. As a first step towards a full quantum mechanical treatment, we implement the broadening of the states, i.e., collisional-broadening in EMC, by replacing Fermi's golden rule by a more general expression. We will generalize only intersubband scattering, i.e., the case when the initial and final states are not the same ($n \neq m$) and we will apply the broadening to the energetic states. For the intrasubband scattering, Fermi's golden rule will be kept since it is believed that the effective intrasubband broadening is largely reduced due to quantum coherence effects [12]. The starting point for deriving the correction is the density-matrix theory for two-dimensional systems, with a general perturbation potential. After generalizing Fermi's golden rule, we also derive e-photon and e-LO phonon scattering in this chapter, which then will contain the effect of collisional broadening. The other scattering mechanisms can be derived in a similar manner. Furthermore we find that our quantum-corrected EMC approach, that now accounts for collisional broadening, reproduces currents in the coherent regime, where the semiclassical EMC method failed. The current in the incoherent regime remains practically unchanged, since transport there is mainly semiclassical, as it was shown in Chapter 3.

6.1 Sinusoidal time dependence of the potential

As done for Fermi's golden rule in Section 2.3 we derive a general scattering rule for the case of sinusoidal potentials (harmonic perturbation), but now using the density matrix formalism instead of time dependent perturbation theory, The starting point is the Liouville-von Neumann equation for the time evolution of the density matrix ρ,

$$i\hbar\frac{d}{dt}\rho = [H, \rho] = H\rho - \rho H. \tag{6.1.1}$$

Here, $\hat{H}$ is the total Hamiltonian operator, i.e., the sum of the unperturbed system Hamiltonian and the perturbation Hamiltonian. We define the Hamiltonian matrix in case of a time varying harmonic perturbation in terms of its matrix elements $\left\langle m|\hat{H}|n\right\rangle$. Here the unperturbed system Hamiltonian $\hat{H}_0$ yields elements $\left\langle m|\hat{H}|n\right\rangle = E_n\delta_{mn}$. For the perturbation we make the ansatz $Ve^{-i\omega t} + V^* e^{i\omega t}$ and we obtain

$$H = \begin{bmatrix} E_1 & V_{12}e^{-i\omega t} + V_{12}^* e^{i\omega t} & . & . \\ V_{21}e^{-i\omega t} + V_{21}^* e^{i\omega t} & E_2 & & \\ . & & & . \\ . & & & . \end{bmatrix}. \tag{6.1.2}$$

Here, the eigenstates of the unperturbed Hamiltonian form the diagonal elements, while the perturbation potentials are given by the off-diagonal terms. The diagonal perturbation elements were neglected, since we derive the scattering rule for the intersubband case, and we will keep the calculation of intrasubband scattering based on Fermi's golden rule. We note that in the case, when H represents the interaction of radiation with matter, V_{12} would be proportional to the applied field times the transition dipole of the system [108]. In the general case, however, V_{nm} can represent any applied harmonic perturbation of the system (for example phonon emission/absorption as well as photon emission/absorption). In analogy to Eq. (6.1.2), we define the density matrix for the system as

$$\rho = \begin{bmatrix} \rho_{11} & \rho_{12} & . & . \\ \rho_{21} & \rho_{22} & & \\ . & & . & \\ . & & & . \end{bmatrix}. \tag{6.1.3}$$

The diagonal elements correspond to the state occupations, while the off-diagonal terms represent their coherent interaction. Using Eq. (6.1.1), we get the evolution equation for the first diagonal density matrix element

$$\begin{aligned} i\hbar\dot{\rho}_{11} = {} & \left[\rho_{11}E_1 + \rho_{21}\left(V_{12}e^{-i\omega t} + V_{12}^* e^{i\omega t}\right) + \rho_{31}\left(V_{13}e^{-i\omega t} + V_{13}^* e^{i\omega t}\right) + ...\right] - \\ & \left[\rho_{11}E_1 + \rho_{12}\left(V_{21}e^{-i\omega t} + V_{21}^* e^{i\omega t}\right) + \rho_{13}\left(V_{31}e^{-i\omega t} + V_{31}^* e^{i\omega t}\right) + ...\right] = \\ & = \sum_b \left[\rho_{b1}\left(V_{1b}e^{-i\omega t} + V_{1b}^* e^{i\omega t}\right) - \rho_{1b}\left(V_{b1}e^{-i\omega t} + V_{b1}^* e^{i\omega t}\right)\right] \end{aligned} \tag{6.1.4}$$

and for the first off-diagonal element

$$\begin{aligned} i\hbar\dot{\rho}_{12} = \left[\rho_{12}E_1 + \rho_{22}\left(V_{12}e^{-i\omega t} + V_{12}^{*}e^{i\omega t}\right) + \rho_{32}\left(V_{13}e^{-i\omega t} + V_{13}^{*}e^{i\omega t}\right) + ...\right] - \\ \left[\rho_{11}\left(V_{12}e^{-i\omega t} + V_{12}^{*}e^{i\omega t}\right) + \rho_{12}E_2 + \rho_{13}\left(V_{32}e^{-i\omega t} + V_{32}^{*}e^{i\omega t}\right) + ...\right] = \\ = (E_1 - E_2)\rho_{12} + \sum_b \left[\rho_{b2}\left(V_{1b}e^{-i\omega t} + V_{1b}^{*}e^{i\omega t}\right) - \rho_{1b}\left(V_{b2}e^{-i\omega t} + V_{b2}^{*}e^{i\omega t}\right)\right]. \end{aligned} \tag{6.1.5}$$

We can generalize the above equations for the time evolution of an arbitrary diagonal element

$$i\hbar\dot{\rho}_{nn} = \sum_m \left[\rho_{mn}\left(V_{nm}e^{-i\omega t} + V_{nm}^{*}e^{i\omega t}\right) - \rho_{nm}\left(V_{mn}e^{-i\omega t} + V_{mn}^{*}e^{i\omega t}\right)\right] \tag{6.1.6}$$

and off-diagonal element

$$i\hbar\dot{\rho}_{nm} = (E_n - E_m)\rho_{nm} + \sum_b \left[\rho_{bm}\left(V_{nb}e^{-i\omega t} + V_{nb}^{*}e^{i\omega t}\right) - \rho_{nb}\left(V_{bm}e^{-i\omega t} + V_{bm}^{*}e^{i\omega t}\right)\right]. \tag{6.1.7}$$

The form of the above equations is still too complex to get an analytical expression for the scattering rate from the initial state n to the final state m, i.e. $\dot{\rho}_{mm}$. We proceed by applying the substitution

$$\rho_{nm} \leftrightarrow \rho_{nm}e^{-i\mathrm{sign}(n-m)\omega t}, \tag{6.1.8}$$

to transform the system into the rotating-frame. This is useful for later performing the so-called rotating-wave approximation [108]. Furthermore we assume that transitions involve only two levels, i.e., we neglect non-diagonal transitions [109, 18]. Using the above approximation, ρ_{nm} depends only on the matrix elements involving levels n and m (the initial and final state). The sum can be dropped and the resulting equations are

$$\begin{aligned} i\hbar\dot{\rho}_{nn} = \rho_{mn}\left\{V_{nm}e^{-i[1+\mathrm{sign}(m-n)]\omega t} + V_{nm}^{*}e^{i[1-\mathrm{sign}(m-n)]\omega t}\right\} - \\ \rho_{nm}\left\{V_{mn}e^{-i[\mathrm{sign}(n-m)+1]\omega t} + V_{mn}^{*}e^{i[1-\mathrm{sign}(n-m)]\omega t}\right\} - i\gamma_{nn}\rho_{nn} + i\Gamma_n, \end{aligned} \tag{6.1.9}$$

for the diagonal and

$$\begin{aligned} i\hbar\dot{\rho}_{nm} = \left[E_n - E_m - \mathrm{sign}(n-m)\hbar\omega\right]\rho_{nm} + \\ (\rho_{mm} - \rho_{nn})\left\{V_{nm}e^{-i[1-\mathrm{sign}(n-m)]\omega t} + V_{nm}^{*}e^{i[1+\mathrm{sign}(n-m)]\omega t}\right\} - i\gamma_{nm}\rho_{nm} \end{aligned} \tag{6.1.10}$$

for the off-diagonal density matrix elements, where Γ_n contains the level filling due to the levels outside of the considered two-level system. Here we have added the damping terms γ_{nm}, which we will calculate self-consistently from the out-scattering rates. Due to the dephasing γ_{mn}, the off-diagonal terms reach steady-state at some point corresponding to $\dot{\rho}_{nm} = 0$. In this case we can rewrite the off-diagonal evolution Eq. (6.1.10) as

$$\begin{gathered}0 = \left[E_n - E_m - \mathrm{sign}(n-m)\hbar\omega\right]\rho_{nm} + \\ (\rho_{mm} - \rho_{nn})\left\{V_{nm}e^{-i[1-\mathrm{sign}(n-m)]\omega t} + V_{nm}^{*}e^{i[1+\mathrm{sign}(n-m)]\omega t}\right\} - i\gamma_{nm}\rho_{nm},\end{gathered} \tag{6.1.11}$$

from which the off-diagonal elements can be calculated in equilibrium as

$$\rho_{nm} = (\rho_{nn} - \rho_{mm})\frac{V_{nm}e^{-i[1-\mathrm{sign}(n-m)]\omega t} + V_{nm}^{*}e^{i[1+\mathrm{sign}(n-m)]\omega t}}{(E_n - E_m - \mathrm{sign}(n-m)\hbar\omega) - i\gamma_{nm}}. \tag{6.1.12}$$

The above formulation of the quantum coherence terms in steady-state contains emission ($e^{i\omega t}$) and absorption ($e^{-i\omega t}$). Substituting Eq. (6.1.12) into Eq. (6.1.9) we find the time-evolution for the diagonal density matrix element n, i.e., the occupation

$$\begin{aligned}i\hbar\dot{\rho}_{nn} = (\rho_{nn} - \rho_{mm})\frac{-2i\gamma_{nm}}{\Delta^2 + \gamma_{nm}^2}&\left[V_{mn}e^{-i[1+\mathrm{sign}(n-m)]\omega t} + V_{mn}^{*}e^{i[1-\mathrm{sign}(n-m)]\omega t}\right]\cdot \\ \cdot\left[V_{nm}e^{-i[1-\mathrm{sign}(n-m)]\omega t} + V_{nm}^{*}e^{i[1+\mathrm{sign}(n-m)]\omega t}\right] &- i\gamma_{nn}\rho_{nn} + i\Gamma_n,\end{aligned} \tag{6.1.13}$$

where $\Delta = E_n - E_m - \mathrm{sign}(n-m)\hbar\omega$ is the detuning of the system. We write the expression for the case of $n - m > 0$ (meaning $E_n > E_m$) and apply the rotating wave approximation (RWA). The RWA assumes that the dynamics of the occupations are described by a slowly varying time-dependent behavior, thus terms proportional to $e^{-2i\omega t}$ average out, i.e., they are neglected. Hence Eq. (6.1.13) is simplified to

$$i\hbar\dot{\rho}_{nn} = (\rho_{nn} - \rho_{mm})\frac{-2i\gamma_{nm}}{(E_n - E_m - \hbar\omega)^2 + \gamma_{nm}^2}V_{nm}^2 - i\gamma_{nn}\rho_{nn} + i\Gamma_n. \tag{6.1.14}$$

The terms proportional to γ_{nn} and Γ_n are evaluated separately in the EMC simulation. Furthermore, we assume that the considered electron is in state n with probability 1. In this case the scattering rate from state n to m is

$$W_{nm}^{em,abs} = \frac{2}{\hbar}V_{nm}^2\frac{\gamma_{nm}}{\left[E_n(\mathbf{k}) - E_m(\mathbf{k}') \mp \hbar\omega\right]^2 + \gamma_{nm}^2}. \tag{6.1.15}$$

Here we have also added the case of the absorption (+ sign for the frequency), which can be derived analogously, except that we assume $E_n < E_m$ and $n < m$. Furthermore, we assumed $W_{nm}^{em} = \dot{\rho}_{mm} = -\dot{\rho}_{nn}$, where n is the initial state and m is the final state of the electron. The above result generalizes Fermi's golden rule, however it is very similar to it. If we consider $\gamma_{mn} \to 0$, i.e, replace the Lorentzian function in Eq. (6.1.15) by a δ-function multiplied by π, we get back Fermi's golden rule for a harmonic perturbation, i.e., Eq. (2.3.10). The broadening term is given by $2\gamma_{nm} = \gamma_{nn} + \gamma_{mm}$, where γ_{nn} is the total out-scattering rate from state n multiplied by the reduced Planck constant. The value of the out-scattering rates can be calculated after the first run of our EMC method which is performed without level broadening of the states.

6.2 Time-constant potential

For deriving other scattering mechanisms that have a static (time-independent) perturbation potential, $\hat{V}$ we need to extend Fermi's golden rule also for this case. The derivation is performed similarly as in the previous section. We start by defining the Hamiltonian for our system

$$H = \begin{bmatrix} E_1 & V_{12} & . & . \\ V_{21} & E_2 & & \\ . & & . & \\ . & & & . \end{bmatrix}. \tag{6.2.1}$$

where the matrix contains the perturbation potentials V_{nm} between the different levels. The density matrix is defined by Eq. (6.1.3) and we use the Liouville equation (6.1.1) for deriving the evolution equation of the density matrix for static perturbations. For the first diagonal element we get the expression

$$i\hbar\dot{\rho}_{11} = \rho_{11}E_1 + \sum_b (\rho_{b1}V_{1b} - \rho_{1b}V_{b1}) \tag{6.2.2}$$

while the first off-diagonal element is

$$i\hbar\dot{\rho}_{12} = (E_1 - E_2)\rho_{12} + \sum_b (\rho_{b2}V_{1b} - \rho_{1b}V_{b2})\,. \tag{6.2.3}$$

We now add the damping terms and write the above equations generally as

$$i\hbar\dot{\rho}_{nn} = \sum_m (\rho_{mn}V_{nm} - \rho_{nm}V_{mn}) - i\gamma_{nn}\rho_{nn} + i\Gamma_n \tag{6.2.4}$$

and

$$i\hbar\dot{\rho}_{nm} = (E_n - E_m)\rho_{nm} + \sum_b (\rho_{bm}V_{nb} - \rho_{nb}V_{bm}) - i\gamma_{nm}\rho_{nm}. \tag{6.2.5}$$

We assume that the off-diagonal terms reach the steady state at some point, thus $\dot{\rho}_{nm} = 0$, and consider scattering between two levels, thus ρ_{nm} depends only on levels n and m. In this case we can calculate the value of the non-diagonal terms

$$\rho_{nm} = \frac{(\rho_{nn} - \rho_{mm})V_{nm}}{E_n - E_m - i\gamma_{nm}}. \tag{6.2.6}$$

The diagonal terms will give the scattering rate and are written as a function of the non-diagonal terms. They involve only scattering between two levels, thus the sum can be dropped and the diagonal element is

$$
\begin{aligned}
i\hbar\dot{\rho}_{nn} &= \rho_{mn}V_{nm} - \rho_{nm}V_{mn} - i\gamma_{nn}\rho_{nn} + i\Gamma_n = \\
&= -(\rho_{nn} - \rho_{mm})V_{nm}V_{mn}\frac{2i\gamma_{mn}}{(E_m - E_n)^2 + \gamma_{mn}^2} - i\gamma_{nn}\rho_{nn} + i\Gamma_n
\end{aligned} \tag{6.2.7}
$$

The terms proportional to γ_{nn} and Γ_n are evaluated separately in the EMC simulation. Assuming that the electron is in state n with probability 1, the above expression changes to

$$
\dot{\rho}_{nn} = -\frac{2}{\hbar}V_{nm}V_{mn}(\rho_{nn} - \rho_{mm})\frac{\gamma_{mn}}{(E_m - E_n)^2 + \gamma_{mn}^2}, \tag{6.2.8}
$$

and the scattering rate from state n to state m is

$$
W_{nm} = \frac{2}{\hbar}V_{nm}^2\frac{\gamma_{nm}}{[E_n(\mathbf{k}) - E_m(\mathbf{k}')]^2 + \gamma_{nm}^2}. \tag{6.2.9}
$$

We note here that by setting $\omega = 0$ in Eq. (6.1.15) we also get the above expression, i.e., a transition rule for static perturbations. The above equation can be applied for the calculation of scattering rates for impurities, interface roughness, acoustic phonons, etc. We also note that the RWA applied for harmonic perturbations in the previous section is not needed here.

In summary, the scattering rates for static and harmonic perturbations are formally obtained from Fermi's golden rule by replacing the delta function with a Lorentzian function defined as $\gamma_{nm}/\left[\pi\left[E_n(\mathbf{k}) - E_m(\mathbf{k}')\right]^2 + \pi\gamma_{nm}^2\right]$. This observation is useful for changing the EMC code to account for collisional broadening of the various scattering mechanisms.

6.3 Scattering with photons

Fermi's golden rule is not sufficient to model the gain saturation and scattering with photons self consistently. The present version of the EMC code already contains the collisional broadening of electron-photon scattering due to this reason [33]. We now derive the scattering with photons based on the results in Section 6.1. The form factor for photon emission and absorption is the transition dipole of the system,

$$
d_{nm} = e_0 \int \psi_m^*(z) z \psi_n(z) dz. \tag{6.3.1}
$$

The perturbation potential can be written in the form

$$
V_{nm} = \frac{1}{2}\mathbf{E}_l\mathbf{d}_{nm}, \tag{6.3.2}
$$

where E_l is the electric field amplitude of the lth mode. The choice of the above perturbation potential was made to fulfill $V_{nm}e^{i\omega t} + V_{nm}^*e^{-i\omega t} = E_l d_{nm}\cos(\omega t)$ in case of real electric field amplitudes and transition dipoles. We proceed by using Eq. (6.1.14) to calculate the rate of scattering with photons,

$$\dot{\rho}_{nn} = (\rho_{mm} - \rho_{nn}) \frac{\mathbf{E}_l^2 \mathbf{d}_{nm}^2}{2\hbar} \frac{\gamma_{nm}}{(E_n - E_m - \hbar\omega)^2 + \gamma_{nm}^2}. \tag{6.3.3}$$

The transition rate from an initial state n to a final state m is given by $\dot{\rho}_{mm}$ similarly to Section 2.3, where the coefficient $\partial_t |a_m(t)|^2$ gave the transition rate $W_{n\mathbf{k}m\mathbf{k}'} = \frac{\partial}{\partial t} \left| a_m^{(1)}(t) \right|^2$. Writing the above equation in terms of $W_{n\mathbf{k}m\mathbf{k}'} = \dot{\rho}_{mm} = -\dot{\rho}_{nn}$ and taking into account the different resonator modes with frequency ω_l, we get [33]

$$W_{n\mathbf{k}m\mathbf{k}'}^{phot} = (f_{n\mathbf{k}} - f_{m\mathbf{k}'}) \frac{Z_0 d_{nm}^2}{n_0 \hbar} \sum_l I_l \frac{\gamma_{nm}}{[E_n(\mathbf{k}) - E_m(\mathbf{k}') - \hbar\omega_l]^2 + \gamma_{nm}^2}.$$

Here n_0 is the refractive index of the active region, Z_0 is the vacuum impedance and I_l is the optical intensity of the lth mode. The occupation probabilities ρ_{mm} and ρ_{nn} in Eq. 6.3.3 were replaced by the distribution functions $f_{m\mathbf{k}'}$ and $f_{n\mathbf{k}}$ and the squared electric field E_l^2 was replaced with the optical intensity of the mode I_l. The scattering rate used in EMC needs to be summed over the final wavevector, $\mathbf{k}'$. Since momentum is conserved, i.e., $\mathbf{k} = \mathbf{k}'$, the sum has a single term. Furthermore, we assume again, that the considered electron is in the initial state, i.e., $f_{n\mathbf{k}} = 1$. For the case when the in-plane scattering is parabolic, we then obtain

$$W_{n\mathbf{k}m\mathbf{k}'}^{phot} = (1 - f_{m\mathbf{k}'}) \frac{Z_0 d_{nm}^2}{n_0 \hbar} \sum_l I_l \frac{\gamma_{nm}}{[E_n(\mathbf{k}) - E_m(\mathbf{k}') - \hbar\omega_l]^2 + \gamma_{nm}^2}. \tag{6.3.4}$$

In the case of non-parabolic scattering, the $E_n(\mathbf{k}) - E_m(\mathbf{k}') - \hbar\omega_l$ expression, was calculated in Section 2.2.3 to only depend on $\mathbf{k}$, thus the sum over the final wavevector $\mathbf{k}'$ can also be performed for the non-parabolic case, and we get the same expression as Eq. (6.3.4), however $E_n(\mathbf{k}) - E_m(\mathbf{k}') - \hbar\omega_l$ changes to $(E_n - E_m)\left[1 - \frac{\hbar^2|\mathbf{k}|^2}{2m^*}(2\alpha + \beta)\right] - \hbar\omega$.We also observe that the electron-photon scattering rate does not contain the electron effective mass in the parallel direction, $m_{||}$.

6.4 Broadening for LO-phonons

The matrix element for electron-phonon interaction was determined in Section 2.3.4. We proceed by using Eq. (6.1.15) instead of Fermi's golden rule, with the square matrix element of LO-phonon scattering from Eq. (2.3.38). Furthermore, we use the notations in Section 2.3.4. The scattering rate from $n\mathbf{k}$ to $m\mathbf{k}'$ is then

$$W_{n\mathbf{k}m\mathbf{k}'}^{phon} = \frac{e^2 \omega_{LO}}{2\pi A \varepsilon_0} \left(N_{Ph} + \frac{1}{2} \pm \frac{1}{2} \right) \left(\frac{1}{\varepsilon_{r,\infty}} - \frac{1}{\varepsilon_{r,0}} \right) J(|\mathbf{k} - \mathbf{k}'|) \frac{\gamma_{if}}{[E_n(\mathbf{k}) - E_m(\mathbf{k}') \pm \hbar\omega_{LO}]^2 + \gamma_{if}^2}. \tag{6.4.1}$$

We need to integrate the above rate over the final wavevector $\mathbf{k}'$. In the EMC code that contains collisional broadening of the initial and final states, we use for parabolic bands

$$W_{n\mathbf{k}m}^{phon} = \frac{e_0^2\omega_{LO}}{2\pi A\varepsilon_0}\left(N_{Ph} + \frac{1}{2} \pm \frac{1}{2}\right)\left(\frac{1}{\varepsilon_{r,\infty}} - \frac{1}{\varepsilon_{r,0}}\right)\int\int P\mathrm{d}\theta k'\mathrm{d}k', \tag{6.4.2}$$

where

$$P = J(\left|\mathbf{k}-\mathbf{k}'\right|)\frac{\gamma_{if}}{\left[E_n(\mathbf{k}) - E_m(\mathbf{k}') \pm \hbar\omega_{LO}\right]^2 + \gamma_{if}^2}. \tag{6.4.3}$$

$P/\int\int P\mathrm{d}\theta k'\mathrm{d}k'$ gives the probability distribution for the final state energy, thus energy conservation is not necessarily fulfilled. Instead, it must be fulfilled statistically, i.e., the energy of the scattered electrons should have its mean value at $E_n(\mathbf{k}) - E_m(\mathbf{k}') \pm \hbar\omega_0$. The complexity of the EMC code does not increase significantly, if we include the above corrected scattering rates. The calculation time of the integrals of P are comparable to the time needed to tabulate the electron-electron form factors. Furthermore, the so-called theta-integral in Eq. (6.4.2) is performed by using the substitution

$$\left|\mathbf{k}-\mathbf{k}'\right| = \sqrt{k^2 + (k')^2 - 2kk'\cos\theta}. \tag{6.4.4}$$

The rest of the scattering mechanisms can be implemented in an analogous manner as shown for the LO-phonons, without further difficulties. The numerical implementation includes a tabulation of P for the initial and final states and wavevectors. Furthermore the scattering rates are tabulated as before, and the choice of the final wavevector after scattering is based on the probability distribution function $P = P_{n\mathbf{k}m\mathbf{k}'}$.

6.5 Effects of quantum corrections on the transport properties of the EMC method

We have included the broadening of the energetic states in EMC by using Eq. (6.4.2) for LO-phonon scattering, derived in Section 6.3. Furthermore, we have used Eq. (6.2.9) for the derivation of quantum-corrected e-interface roughness, e-impurity and e-acoustic phonon scattering. The derivation was performed by using the same steps as in Section 6.4. We have included the quantum corrected rates in EMC, while we have kept the e-e scattering rate semiclassical.

In Fig. 6.5.1, we show the current-voltage characteristics for the 2.75 THz QCL, discussed in Section 3.2. The artificial current spikes which arise for level anticrossing below 2 meVwere avoided by choosing the bias point adequately. We observe a better agreement of the quantum-corrected EMC results with experiment, especially for low biases. As it has been discussed in Chapter 3, NEGF could reproduce the experimental currents in the coherent regime while the semiclassical EMC method failed. This is not the case for the quantum corrected EMC, which now correctly models the current for the low

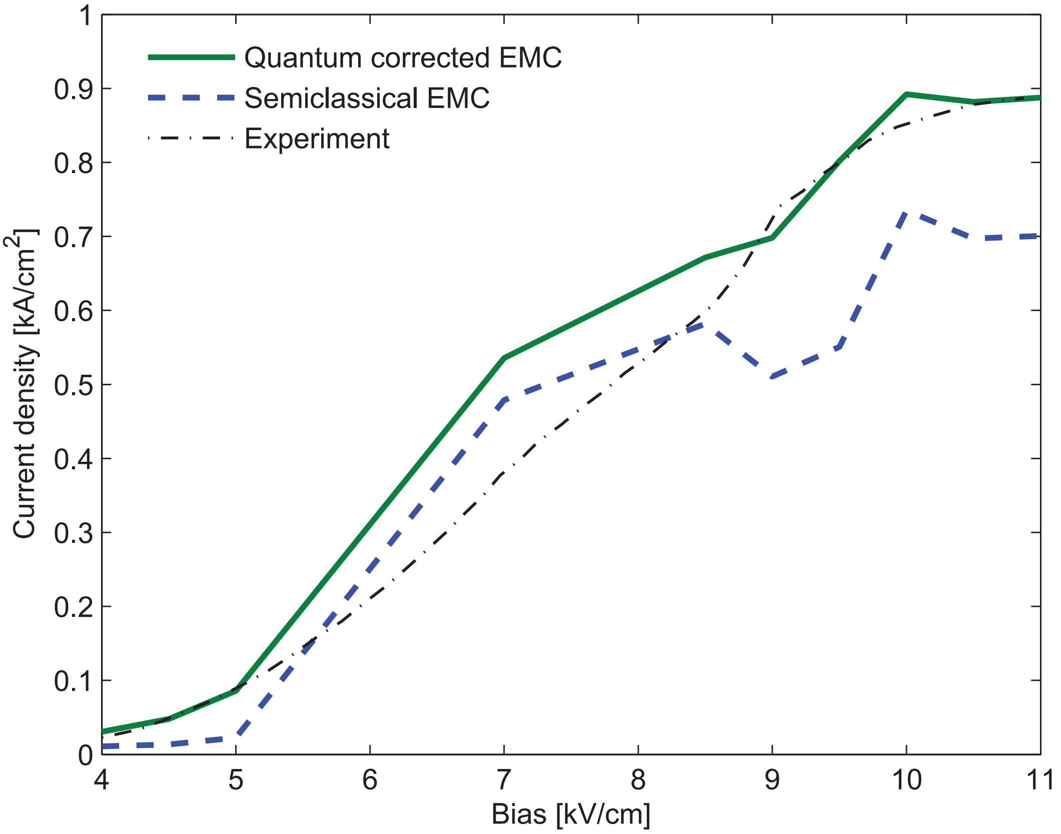

Figure 6.5.1: Effects of collisional broadening on the QCL discussed in Section 3.2. We observe an increase in the coherent regime of the EMC current when we include the broadening, which facilitates the scattering with phonons especially for lower biases. Furthermore, the relative increase of the current in the lasing regime is small.

biases, i.e., in the coherent regime. This can be confirmed by comparing the semiclassical and quantum corrected curves to experiment in the bias range of 4-5 kV/cm in Fig. 6.5.1. Furthermore, there is also a good agreement to experiment in the incoherent regime, where the relative increase of the current for the case of quantum corrections is small.

The present results provide an outlook for the inclusion of quantum corrections in EMC methods. Based on the framework of this chapter, further effects such as quantum coherence could be investigated, which we believe can reduce the artificial current spikes of the semiclassical EMC approach. The Lorentzian function introduced for level broadening can also contain additional effects besides broadening due to the calculated scattering rates in EMC. For example, states that are highly unbound have lifetimes comparable to the inverse scattering rates, as discussed in Section 2.1.3 and their broadening can also be included in our approach. The broadening of the higher lying states could be included for a more accurate modeling of transport in the continuum states, which has proven to lack a consistent description within a Monte-Carlo framework.

6.6 Summary

We have implemented quantum corrections for the energetic level broadening in our EMC method. Based on a consistent derivation of a Lorentzian rule from the density matrix formalism we have replaced Fermi's golden rule and derived the electron-photon and electron-phonon scattering rates.

All the scattering mechanisms, except e-e scattering, were corrected for the broadening of the energetic states and self-consistently included in EMC. We observe corrected current-voltage curves, which now agree to experiment in the coherent regime, in contrast to Sections 3.2 and 3.3. In the incoherent regime, we have observed a small relative change of the currents as compared to the semiclassical result, which proves the largely semiclassical nature of transport in this regime.

Appendix

The theory of our ensemble Monte-Carlo method is based on Fermi's golden rule, which will be derived using time-dependent perturbation analysis presented in this appendix. We start from a set of known basis functions, which are in our case solutions of the time-independent Hamiltonian H_0. The time-dependent part of the Hamiltonian is represented by $H_{int}(t)$ and considered as a perturbation that is added to time-independent part:

$$H = H_0 + H_{int}(t) \tag{6.6.1}$$

The wavefunctions are quasi-bound in the growth direction, while they have plane-wave solutions in the in-plane direction. We will define these by

$$\Psi_m(x,y,z) = < x,y,z||m >= \frac{1}{\sqrt{L_x L_y}} \psi_m(z) e^{i\mathbf{k'x}}. \tag{6.6.2}$$

The solution $\psi_m(z)$ for the unperturbed case, was discussed in Section 2.1, and can be written using Eq. (6.6.2) in the form

$$|\psi\rangle = c_1|1> + c_2|2> + c_3|3> + ..., \tag{6.6.3}$$

where $|m>$ are time-independent. The time dependence is contained in the constants $c_1, c_2 ...$, for small perturbations, that only slightly change the potential profile of the heterostructure. Probability is conserved by

$$\langle\psi|\,|\psi\rangle = c_1^* c_1 + c_2^* c_2 + ... = 1, \tag{6.6.4}$$

in case of a dissipationless system. These coefficients are written in the Schrödinger picture, thus they change in time and the basis functions remain constant. The solution of the perturbed case has the form

$$\psi(t) = \sum_m c_m(t)|m>, \tag{6.6.5}$$

and the new time-dependent Schrödinger equation is

$$[H_0 + H_{int}(t)] \sum_n c_n(t)|n> = i\hbar \sum_n \dot{c}_n(t)|n> . \tag{6.6.6}$$

Multiplying by the conjugate basis function $< m|$, we get for the coefficients in the Schrödinger picture

$$i\hbar\dot{c}_m(t) = E_m c_m(t) + \sum_n c_n(t) < m|H_{int}(t)|n > . \tag{6.6.7}$$

If we make the substitution

$$a_m(t) = c_m(t)e^{i\frac{E_m}{\hbar}t}, \tag{6.6.8}$$

we change the basis from the Schrödinger picture to the interaction picture, and rewrite Eq. (6.6.7) using Eq. (6.6.8)

$$\dot{a}_m(t) = -\frac{i}{\hbar}\sum_n a_n(t)e^{i\frac{E_m}{\hbar}t - i\frac{E_n}{\hbar}t} < m|H_{int}(t)|n > . \tag{6.6.9}$$

This is a key result in deriving Fermi's golden rule.

Nomenclature

Acronyms

BTC	bound to continuum
EMC	ensemble Monte-Carlo
FWHM	full width at half maximum
IR	interface roughness
lhs.	left hand side
LDOS	local density of states
LO-phonon	longitudinal optical phonon
MBE	molecular beam epitaxy
MIR	mid-infrared
MOCVD	metal-organic chemical vapor deposition
NDR	negative differential resistance
NEGF	non-equilibrium Green's functions
QCL	quantum cascade laser
rhs.	right hand side
RP	resonant phonon
RPA	random phase approximation
RWA	rotating wave approximation
SP	Schrödinger-Poisson
THz	terahertz
TMM	transfer matrix method
TO-phonon	transverse optical phonon
WPE	wall-plug efficiency

Greek symbols

α	factor of non-parabolicity
γ_{nm}	broadening of the transition from state n to state m
Γ_m^{sp}	imaginary part of the eigensolution m of the Schrödinger equation for a biased multi-quantum well structure
Γ_n	level broadening due to transitions outside the two level system
$\Gamma_{n\mathbf{k}m}$	scattering rate $W_{n\mathbf{k}m}$, defined on an interval, for the random choice of scattering type and final state
Δ	detuning in the density matrix theory, or the mean height of the interface penetrations in context of interface roughness
$\Delta(\mathbf{r})$	roughness of the material interface as a function of the in-plane position $\mathbf{r}$
Δ_{so}	difference between splitoff hole and light hole bands
$\Delta n(d)$	population inversion in function of diagonality d
Δn_{rel}	relative change of population inversion
$\Delta f(d)$	spectral linewidth of the QCL as a function of diagonality d
Δf_{rel}	relative change of the FWHM spectral linewidth
Δ_z	discretization step
ε	static dielectric constant
$\varepsilon(\omega)$	frequency dependent dielectric constant
ε_b	dielectric constant in barrier
ε_w	dielectric constant in well
ε_m	uniform dielectric constant
$\varepsilon_{r,0}$	static dielectric constant
$\varepsilon_{r,\infty}$	high frequency dielectric constant
η_{WPE}	wall-plug efficiency, i.e., ratio of optical and electric power
ι	infinitely small value in the vicinity of z_j
κ_z	$i\kappa_z$ is the wavevector component in the z direction for energies smaller than the conduction band profile at the jth grid point
Λ	correlation length
Π_{ab}	polarizability tensor
ρ	density matrix
σ	electrical conductivity
ψ	wavefunction
$\psi^+(z_j)$	$\lim\limits_{z\to z_j, z>z_j} \psi(z)$
$\psi^-(z_j)$	$\lim\limits_{z\to z_j, z<z_j} \psi(z)$

ψ_m	wavefunction in the confined direction, corresponding to the state m
$\Psi_n(x,y,z)$	3D wavefunction of the system
ω_{LO}	LO-phonon frequency
ω_{mn}	frequency, corresponding to the energetic difference between states $E_m(\mathbf{k}')$ and $E_n(\mathbf{k})$
$\omega_{\mathbf{Q}}$	frequency of the vibration, corresponding to the 3D phonon wavevector $\mathbf{Q}$
ω_{TO}	transverse optical phonon frequency
Ω_0	volume of the Wiegner-Seitz cell, given by $a^3/4$

Latin symbols

a	lattice constant
$a_m(t)$	coefficient describing the time-evolution of state m in the interaction picture
A	cross section area $A = L_x L_y$
$\mathbf{A}_0^q$	vector potential for the mode q
A_{eff}	area defined by the number of simulated electrons in EMC (when the sheet density is known)
$\mathbf{B}$	magnetic field
C_j	coefficient of the wavefunctions defined in the TMM
C_N	wavefunction coefficient, at the end of the simulated region (see Transfer matrix method)
$\tilde{C}_N$	transformed TMM coefficient at the end of the simulation interval
d_{nm}	transition dipole
$\mathbf{D}$	electric displacement current
$\mathbf{D}^0$	amplitude of the displacement current
D_j	coefficient of the wavefunctions defined in the TMM
$\tilde{D}_N$	transformed TMM coefficient at the end of the simulation interval
e_0	electron charge
e_{eff}	effective charge, produced by the ion-pair, in case of LO-phonon scattering
E	energy
$\mathbf{E}$	electric field (only in bold, otherwise energy)
$E(\mathbf{K})$	3D kinetic energy of the system
E_g	bandgap
E_l	$\lvert\mathbf{E}_l\rvert$

$\mathbf{E}_l$	electric field amplitude for the lth mode
$\mathbf{E}_{latt}$	electric field due to phonons (lattice vibrations)
$\mathbf{E}_{latt}^0$	amplitude of the electric field
E_m	energy level for the mth state
$E_m(\mathbf{k})$	sum of the kinetic and confinement energy for the state m
$E_m^{\vert\vert}(\mathbf{k})$	kinetic energy of the mth state
E_m^r	real part of the eigensolution m of the Schrödinger equation for a biased multi-quantum well structure
E_m^{ti}	energetic solution of the time-independent Schrödinger equation, for a biased multi-quantum well structure (complex energy)
E_{tot}	the sum of the energy exchange of the two electrons (should be 0 due to energy conservation)
E_{tot}^p	see E_{tot}, here the p denotes the parabolic case
$E_{tot}^{p,s}$	see E_{tot}^p, but with the substituted momentum given in Section 2.3.8.1
E_z	energy in the confined direction
E_z^{kin}	kinetic energy in the confined direction
$\mathbf{E}_L$	longitudinal electric field
$\mathbf{E}_T$	transverse electric field (0)
f	distribution function (general)
f_d^e	function that gives the number of simulated electrons, for a given state n and wavevector $\mathbf{k}$
f_m	distribution function of the mth state
f_{mn}^{imp}	impurity form factors
f_{mn}^o	oscillator strength between states n and m
$f_{n\mathbf{k}}$	distribution function for the state n at wavevector $\mathbf{k}$
f_{osc}	oscillator strength of the lasing transition
f_{osc}^{ver}	oscillator strength of the vertical transition QCL design
$\mathbf{F}$	force
$F_{nimj}(q)$	e-e form factor
h	minimization function, where its local minima give the energetic states
H	Hamiltonian
H_{int}	interaction Hamiltonian of the electron with a scattering process, defined as a (static or harmonic) perturbation on the electronic system
I_l	optical intensity of the lth mode
$\mathbf{k}$	wavevector ($\mathbf{k} = [k_x, k_y]$) in the in-plane direction

k_x	wavevector in the x direction
k_y	wavevector in th y direction
k_z	wavevector in the confined direction
$k_{z_{1,2}}$	solutions for the wavevector in the z-direction, based on the kinetic energy E_z^{kin}
k_{z_b}	wavevector in the confined direction for the barrier
k_{z_j}	wavevector in the confined direction at grid point j
k_{z_w}	wavevector in the confined direction for the well
$\mathbf{K}$	three dimensional momentum of the electron
L_x	cross section length in the x direction
L_y	cross section length in the y direction
m^*	effective mass
$m^*_+(z_j)$	$\lim\limits_{z\to z_j, z>z_j} m^*_z(z)$
$m^*_-(z_j)$	$\lim\limits_{z\to z_j, z<z_j} m^*_z(z)$
$m_{\|\|}$	in-plane effective mass
$m_{\|\|,m}$	in-plane effective mass for the state m
m_{nucl}	reduced effective mass, in the case of an oscillating ion-pair
$m^*_z(z)$	effective mass in the confinement direction
m_{z_j}	effective mass in the confined direction, at the grid point j
M_{nimj}	matrix element in case of e-e scattering
$M(Q)$	amplitude of the LO-phonon perturbation potential
n_0	refractive index
n_{2D}	sheet doping density
n^m	volume density of the population in state m
n_c	maximum number of simulation electrons in EMC, for a given state n and wavevector $\mathbf{k}$
n_{cells}	number of ion-pairs per unit volume
n_s	predefined number of states that the SP solver finds
N_A	number of type A disorder sites
N_B	number of type B disorder sites
N_{Ph}	number of LO-phonons
N_s	number of simulated electrons in EMC
$N(z)$	volume doping of the structure
p_a	probability for antiparallel spin collisions
p_p	probability for parallel spin collisions
$\hat{\mathbf{p}}_{nm}$	momentum operator
$\mathbf{P}_{ion}$	polarization induced by the oscillating dipole $\mathbf{u}$

$\mathbf{P}_{ion}^{0}$	amplitude of the polarization
P_V	dissipated power per unit volume
q	$q = \|\mathbf{k} - \mathbf{k}'\|$, wavenumber corresponding to momentum exchange ($q = \|\mathbf{k} - \mathbf{k}' + \mathbf{k}_0 - \mathbf{k}_0'\|$ in case of e-e scattering)
q_0	charge
q_z	LO-phonon wavevector in the confinement direction
$\mathbf{Q}$	3D wavevector of the phonon
$\mathbf{R}$	position of the electron
$\mathbf{R}_A$	lattice vector of the disorder site A
t	time
T_m	lifetime of state m
T_L	lattice temperature
$\mathbf{u}$	lattice displacement vector
$u_1(\mathbf{r})$	potential profile, in case of an alloy material
$u_2(\mathbf{r})$	alloy perturbation potential in terms of atomic positions
$\mathbf{u}_T$	transverse part of the lattice displacement vector
$\mathbf{u}_L$	longitudinal part of the lattice displacement vector
$\mathbf{U}_0$	amplitude of the lattice displacement (vibration)
U_A	potential of material type AC
$\mathbf{v}_e$	electron velocity
$\hat{V}$	perturbation operator
V_0	conduction band offset between two materials or within an alloy
V_c	volume of the crystal
V_j	potential at the grid point j
$V_{mnji}^{ee,s}$	screened e-e scattering matrix element
V_{mn}^{int}	interface roughness matrix element
V_{mn}^{imp}	impurity matrix element for the sates n and m
V_{nm}	perturbation potential of the transition between state n and m
V_{nm}^{a}	alloy perturbation potential matrix element
V_{nimj}^{ee}	matrix element of the e-e perturbation potential
V_P	Poisson potential produced by the electrons in the device
$\hat{V}_{pert}$	perturbation potential energy operator
V_{pert}^{ee}	e-e scattering perturbation potential
V_{pert}^{imp}	impurity perturbation potential
V_{mn}^{LOPh}	LO-phonon matrix element between initial state n and final state m
$V(z)$	conduction band profile (including band bending)

$V(E_m(\mathbf{k}), E_n(\mathbf{k}'))$	
z_{imp}	position of the impurity
z_j	jth position on the discretized spatial grid, where we solve the Schrödinger equation
Z	impedance in the active region
Z_0	vacuum impedance

List of Figures

2.1.1 Approximation of potential profile by step-functions. 20

2.1.2 Conduction band profile, classification of states 21

2.1.3 (a) h, (b) $\partial_{E_z} h$ and (c) lifetime as a function of the energy E_z for the case of a quantum well with 30 Å barrier. 25

2.1.4 Lifetime as a function of barrier width and example states. 26

2.5.1 The schematic diagram of the Monte-Carlo algorithm 53

2.5.2 Scattering rate tabulation, for choosing the final state and scattering type. 55

2.5.3 (a) Resonant phonon depopulation and (b) bound to continuum quantum cascade lasers. . 58

2.6.1 (a) Conduction band profile and squared wavefunctions, obtained for thermally occupied subbands (dashed lines) and self-self consistent simulations (solid lines).The conduction band profile without space charge effects included is also displayed as a reference (dotted line). (b) Simulated spectral gain versus frequency for the three cases of accounting space charge effects, shown above. 59

2.6.2 Simulated gain spectra vs frequency, obtained by fully taking into account (solid curves) and ignoring the exchange effect (dotted curves), and by ignoring parallel (dashed curves) spin collisions. As a reference, the result obtained without e-e scattering is also shown (dash-dotted curves). The simulation results are shown for a lattice temperature of (a) 10 K and (b) 90 K. 61

2.6.3 (a) Subband occupations and (b) subband temperatures extracted from our EMC simulations, by fully taking into account (x-marks, solid curves) and ignoring the exchange effect (plus signs, dotted curves), and by ignoring parallel spin collisions (circles, dashed curves). The lines are guide to the eye. 62

2.6.4 Electron dwell times, simulated by our EMC method, by fully taking into account (x-marks, solid curves) and ignoring the exchange effect (plus signs, dotted curves), and by ignoring parallel spin collisions (circles, dashed curves). The lines are guide to the eye. . 63

2.6.5 Coulomb matrix elements, as obtained with different types of screening models for the structure shown in Fig. 2.6.1(a). (a) V_{1111}; (b) V_{1212}; (c) V_{1122}. 64

2.6.6 Spectral gain as a function of frequency, obtained by our EMC method. The three cases shown account for screening in the RPA (solid curves), in the modified single subband model for all matrix elements (dashed curves) or in the modified single subband model for the intrasubband elements only (dotted curves), i.e., treating intersubband elements as unscreened. (a) $T_\mathrm{L} = 10\,\mathrm{K}$; (b) $T_\mathrm{L} = 90\,\mathrm{K}$. 64

2.6.7 (a) Relative subband occupations and (b) subband temperatures, as obtained by our EMC method where for the screening we have used the RPA (x-marks, solid curves) and the modified single subband model for all matrix elements (circles, dashed curves) or for the intrasubband elements only (plus signs, dotted curves). The lines are guide to the eye. . . 65

2.6.8 Electron dwell times, extracted from our EMC simulations which were obtained by taking into account screening in the RPA (x-marks, solid curves), and using the modified single subband model for all matrix elements (circles, dashed curves) or for the intrasubband elements only (plus signs, dotted curves). The lines are guide to the eye. 65

3.1.1 Conduction band profile and absolute square of the wavefunctions for the investigated Stark ladder [69], biased at 10 kV/cm. It consists of 40 Å $\mathrm{Al}_{0.1}\mathrm{Ga}_{0.9}\mathrm{As}$ barriers and 240 Å wells. The doping in the well is $10^{10}\,\mathrm{cm}^{-2}$. 71

3.1.2 Calculated IV-characteristics of the $\mathrm{GaAs/Al}_{0.1}\mathrm{Ga}_{0.9}\mathrm{As}$ Stark ladders operating in the THz regime. The wells are 240 Å. Barrier widths are 20 Åin (a) and 40 Å in (b) respectively. Results of the EMC method are depicted by the solid line and agree in a large bias range with NEGF calculations (dash-dotted). 72

3.1.3 Theoretically predicted absorption for the Stark ladder with 40 Å barriers at 10 kV/cm, designed to operate at a frequency of 4.9 THz. Results of the EMC method (solid) nicely agree with results of the NEGF method (dash-dotted). 73

3.2.1 Energy levels and squared wavefunctions of the QCL at the peak-gain bias of 54.16 mV per period given by the EMC method. 74

3.2.2 (a) Comparison of the simulated currents to experimental results. (b) Different cases of transport, which are shown to illustrate the contribution of the varying scattering and transport mechanisms. 75

3.2.3 (a) EMC and (b) NEGF local density of states of the simulated QCL at the peak-gain bias of 54.16 mV per period. We observe similar linewidth and the missing level #4 in case of NEGF. 76

3.2.4 The optical gain in EMC (solid) and NEGF (dashed) at a bias of 54.16 mV per period. We get quantitative agreement. The slight asymmetry in EMC is explained in the text. . 76

3.3.1 Conduction band profile and wavefunctions squared for the investigated QCL. The wavefunctions serve as input for the semiclassical EMC simulation. The modeled THz QCL (biased at 13.4 kV/cm) [25], consists of $Al_{0.15}Ga_{0.85}As$ barriers and GaAs wells with layer thicknesses (given in Å): (38) 64 (24) 78 (54) 94 (24) $\underline{148}$, where the values in the brackets represent the barriers. The underlined well contains a uniform sheet doping of 2.8 $\times 10^{10}\,\mathrm{cm}^{-2}$. 77

3.3.2 Calculated and experimental current-voltage characteristics of the THz-QCL in Ref. [25]. The ballistic NEGF calculation (dotted) ignores any incoherent scattering and yields much smaller current densities than results of NEGF calculations including all relevant scattering mechanisms (dash-dotted). Results of the EMC method (solid) agree quantitatively with NEGF calculations and experimental data (dashed) for bias fields above 10 kV/cm. . . . 78

3.3.3 Spectral gain profile for the 3.4 THz QCL calculated by EMC and NEGF. 78

4.2.1 Occupation of the upper and lower laser level (solid lines), injection level (dashed lines) and ground level (dotted lines) for the a) 2.3, b) 3.2 and c) 4.1 THz structure. Furthermore, the temperature dependence of the d) injection efficiency into the upper laser level, e) parasitic injection efficiency into the lower laser level, and f) gain for the 2.3, 3.2 and 4.1 THz structure is shown. The inset contains a close-up of the gain in the technically relevant temperature range of 150-200 K, clearly showing the superior performance of the 3.2 THz QCL in this temperature range. 83

4.3.1 Conduction band diagram for the 3.2 THz QCL with (a) 0% diagonality and (b) 70% diagonality. Upper and lower laser levels are marked by red and black bold solid lines. . . 85

4.3.2 Dependence of the peak gain on the active region lattice temperature for different operating frequencies and diagonalities. The shown results are for optimum bias, which only weakly depends on temperature and has for each structure been determined at 150 K as to yield maximum gain. 86

4.3.3 Δn and Δf for different degrees of diagonality for the (a) 2.3 THz QCL and (b) 4.1 THz QCL at lattice temperatures of 150 and 200 K, respectively. The bias is chosen as to maximize the peak gain. 87

4.3.4 Temperature dependence for (a) 30% diagonality and (b) 50% diagonality of the relative inversion Δn_{rel} and relative inverse linewidth $\Delta f_{\mathrm{rel}}^{-1}$. The peak gain improvement is $\propto \Delta n_{\mathrm{rel}} \Delta f_{\mathrm{rel}}^{-1}$. 88

4.4.1 Peak gain of the simulated 2.3 THz and of the 4.1 THz QCLs with different diagonalities. The top figures were calculated with 2.4 Å interface roughness mean height, while the bottom plots correspond to our published results also shown in Fig. 4.3.2 (mean height of 1.2 Å and correlation length of 100). 89

5.1.1 EMC simulation results for the current-voltage characteristics. We observe a large effect of interface roughness and also an influence of alloy scattering on the total current, while e-e scattering and impurity scattering can be practically neglected. A comparison to experiment is shown in the inset, where we find qualitative agreement between EMC and the experimental result. 93

5.1.2 Influence of the different scattering mechanisms on the spectral gain profile. The result of the full EMC simulation is indicated by the bold solid line. The narrow solid, dashed, dotted and dash-dotted lines corresponds to the cases where we switch off alloy, interface roughness, impurity and e-e scattering, respectively. We see that interface roughness scattering leads to a significant reduction of the gain. 94

5.1.3 Output power calculated from the EMC method and compared to experiment. Simulations were performed by fixing the lasing frequency to 8.04 μm. We observe a good agreement for the output power at various bias points. 95

5.1.4 Current-voltage characteristics with (dashed line) and without (solid line) electron-photon scattering events included. 96

5.2.1 Current-voltage characteristics. The EMC simulation results with (X marks) and without (crosses) lasing included are compared to available experimental data [7] (solid curve). The electric current is governed by stimulated photon emission and absorption processes, as has to be expected for a WPE as high as 50%. 98

5.2.2 (a) Current-optical power and (b) current-WPE characteristics. The EMC simulation results with lasing included (X marks) are compared to available experimental data[7] (solid curve). 99

5.2.3 (a) Simulated kinetic electron distribution $f(E)$ in the upper and lower laser level with and without lasing included. (b) Energy resolved electron density without lasing included; (c) energy resolved electron density with lasing included. The upper laser levels are marked by solid rectangles, and the lower laser level is marked by dashed rectangles. 100

6.5.1 Effects of collisional broadening on the QCL discussed in Section 3.2. We observe an increase in the coherent regime of the EMC current when we include the broadening, which facilitates the scattering with phonons especially for lower biases. Furthermore, the relative increase of the current in the lasing regime is small. 111

List of Tables

2.1 Scattering rate indices in the code 53

2.2 Scattering mechanisms and approximations used in the thesis. 66

4.1 Overview of the designed THz QCLs. All layer thicknesses are given in angstrom, and bold numbers indicate barriers. The underlined wells are doped with a sheet density of $2.7{\times}10^{10}\,\mathrm{cm}^{-2}$ in their 55 Å-wide middle region. 82

Bibliography

[1] J. Faist, F. Capasso, D. L. Sivco, C. Sirtori, A. L. Hutchinson, and A. Y. Cho, “Quantum cascade laser,” *Science*, vol. 264, no. 5158, pp. 553–556, 1994.

[2] P. Werle, F. Slemr, K. Maurer, R. Kormann, R. Mucke, and B. Janker, “Near- and mid-infrared laser-optical sensors for gas analysis,” *Optics and Lasers in Engineering*, vol. 37, pp. 101–114, Feb. 2002.

[3] J. Faist, F. Capasso, C. Sirtori, D. L. Sivco, J. N. Baillargeon, A. L. Hutchinson, S. Chu, and A. Y. Cho, “High power mid-infrared ($\lambda \sim 5$ μm) quantum cascade lasers operating above room temperature,” *Applied Physics Letters*, vol. 68, pp. 3680–3682, Jun. 1996.

[4] M. Beck, D. Hofstetter, T. Aellen, J. Faist, U. Oesterle, M. Ilegems, E. Gini, and H. Melchior, “Continuous wave operation of a mid-infrared semiconductor laser at room temperature,” *Science*, vol. 295, pp. 301–305, Jan. 2002.

[5] A. Lyakh, C. Pflügl, L. Diehl, Q. J. Wang, F. Capasso, X. J. Wang, J. Y. Fan, T. Tanbun-Ek, R. Maulini, A. Tsekoun, R. Go, and C. Kumar N. Patel, “1.6 W high wall plug efficiency, continuous-wave room temperature quantum cascade laser emitting at 4.6 μm,” *Applied Physics Letters*, vol. 92, no. 11, p. 111110, Mar. 2008.

[6] P. Q. Liu, A. J. Hoffman, M. D. Escarra, K. J. Franz, J. B. Khurgin, Y. Dikmelik, X. Wang, J. Fan, and C. F. Gmachl, “Highly power-efficient quantum cascade lasers,” *Nature Photonics*, vol. 4, pp. 95–98, Feb. 2010.

[7] Y. Bai, S. Slivken, S. Kuboya, S. R. Darvish, and M. Razeghi, “Quantum cascade lasers that emit more light than heat,” *Nature Photonics*, vol. 4, pp. 99–102, Feb. 2010.

[8] R. Köhler, A. Tredicucci, F. Beltram, H. E. Beere, E. H. Linfield, A. G. Davies, D. A. Ritchie, R. C. Iotti, and F. Rossi, “Terahertz semiconductor-heterostructure laser,” *Nature*, vol. 417, pp. 156–159, May 2002.

[9] M. Tonouchi, “Cutting-edge terahertz technology,” *Nature Photonics*, vol. 1, pp. 97–105, Feb. 2007.

[10] L. Schrottke, M. Giehler, M. Wienold, R. Hey, and H. T. Grahn, "Compact model for the efficient simulation of the optical gain and transport properties in thz quantum-cascade lasers," *Semiconductor Science and Technology*, vol. 25, no. 4, p. 045025, 2010.

[11] C. Jirauschek, A. Matyas, and P. Lugli, "Modeling bound-to-continuum terahertz quantum cascade lasers: The role of Coulomb interactions," *Journal of Applied Physics*, vol. 107, no. 1, p. 013104, Jan. 2010.

[12] C. Jirauschek and P. Lugli, "Monte-Carlo-based spectral gain analysis for terahertz quantum cascade lasers," *Journal of Applied Physics*, vol. 105, no. 12, p. 123102, 2009.

[13] J. T. Lü and J. C. Cao, "Monte Carlo simulation of hot phonon effects in resonant-phonon-assisted terahertz quantum-cascade lasers," *Applied Physics Letters*, vol. 88, no. 6, p. 061119, Feb. 2006.

[14] A. Mátyás, T. Kubis, P. Lugli, and C. Jirauschek, "Comparison between semiclassical and full quantum transport analysis of THz quantum cascade lasers," *Physica E Low-Dimensional Systems and Nanostructures*, vol. 42, pp. 2628–2631, Sep. 2010.

[15] A. Mátyás, T. Kubis, P. Lugli, and C. Jirauschek, "Carrier transport in THz quantum cascade lasers: Are Green's functions necessary?" *Journal of Physics Conference Series*, vol. 193, no. 1, p. 012026, Nov. 2009.

[16] A. Wacker, "Gain in quantum cascade lasers and superlattices: A quantum transport theory," *Physical Review B*, vol. 66, no. 8, p. 085326, Aug. 2002.

[17] F. Banit, S.-C. Lee, A. Knorr, and A. Wacker, "Self-consistent theory of the gain linewidth for quantum-cascade lasers," *Applied Physics Letters*, vol. 86, no. 4, p. 041108, Jan. 2005.

[18] S.-C. Lee, F. Banit, M. Woerner, and A. Wacker, "Quantum mechanical wavepacket transport in quantum cascade laser structures," *Physical Review B*, vol. 73, no. 24, p. 245320, Jun. 2006.

[19] T. Kubis, C. Yeh, P. Vogl, A. Benz, G. Fasching, and C. Deutsch, "Theory of nonequilibrium quantum transport and energy dissipation in terahertz quantum cascade lasers," *Physical Review B*, vol. 79, no. 19, p. 195323, May 2009.

[20] C. Deutsch, A. Benz, H. Detz, P. Klang, M. Nobile, A. M. Andrews, W. Schrenk, T. Kubis, P. Vogl, G. Strasser, and K. Unterrainer, "Terahertz quantum cascade lasers based on type II InGaAs/GaAsSb/InP," *Applied Physics Letters*, vol. 97, no. 26, p. 261110, Dec. 2010.

[21] R. Terazzi and J. Faist, "A density matrix model of transport and radiation in quantum cascade lasers," *New Journal of Physics*, vol. 12, no. 3, p. 033045, 2010.

[22] A. Mátyás, M. A. Belkin, P. Lugli, and C. Jirauschek, “Temperature performance analysis of terahertz quantum cascade lasers: Vertical versus diagonal designs,” *Applied Physics Letters*, vol. 96, no. 20, p. 201110, May 2010.

[23] A. Mátyás, P. Lugli, and C. Jirauschek, “Photon-induced carrier transport in high efficiency mid-infrared quantum cascade lasers,” *Journal of Applied Physics*, vol. 110, no. 1, p. 013108, Jul. 2011.

[24] C. Jirauschek, G. Scarpa, P. Lugli, M. S. Vitiello, and G. Scamarcio, “Comparative analysis of resonant phonon THz quantum cascade lasers,” *Journal of Applied Physics*, vol. 101, no. 8, p. 086109, Apr. 2007.

[25] H. Callebaut, S. Kumar, B. S. Williams, Q. Hu, and J. L. Reno, “Analysis of transport properties of tetrahertz quantum cascade lasers,” *Applied Physics Letters*, vol. 83, p. 207, Jul. 2003.

[26] C. Jirauschek and P. Lugli, “Limiting factors for high temperature operation of THz quantum cascade lasers,” *Physica Status Solidi C Current Topics*, vol. 5, pp. 221–224, Jan. 2008.

[27] C. Jirauschek, “Accuracy of transfer matrix approaches for solving the effective mass schrödinger equation,” *IEEE Journal of Quantum Electronics*, vol. 45, pp. 1059–1067, 2009.

[28] R. C. Iotti and F. Rossi, “Nature of Charge Transport in Quantum-Cascade Lasers,” *Physical Review Letters*, vol. 87, no. 14, p. 146603, Oct. 2001.

[29] H. Callebaut, S. Kumar, B. S. Williams, Q. Hu, and J. L. Reno, “Importance of electron-impurity scattering for electron transport in terahertz quantum-cascade lasers,” *Applied Physics Letters*, vol. 84, p. 645, Feb. 2004.

[30] R. C. Iotti and F. Rossi, “Carrier thermalization versus phonon-assisted relaxation in quantum-cascade lasers: A Monte Carlo approach,” *Applied Physics Letters*, vol. 78, p. 2902, May 2001.

[31] O. Bonno, J.-L. Thobel, and F. Dessenne, “Modeling of electron-electron scattering in Monte Carlo simulation of quantum cascade lasers,” *Journal of Applied Physics*, vol. 97, no. 4, p. 043702, Feb. 2005.

[32] F. Compagnone, A. di Carlo, and P. Lugli, “Monte Carlo simulation of electron dynamics in superlattice quantum cascade lasers,” *Applied Physics Letters*, vol. 80, p. 920, Feb. 2002.

[33] C. Jirauschek, “Monte Carlo study of carrier-light coupling in terahertz quantum cascade lasers,” *Applied Physics Letters*, vol. 96, no. 1, p. 011103, Jan. 2010.

[34] U. Ekenberg, “Nonparabolicity effects in a quantum well: Sublevel shift, parallel mass, and landau levels,” *Phys. Rev. B*, vol. 40, no. 11, pp. 7714–7726, Oct. 1989.

[35] G. Hendorfer, M. Seto, H. Ruckser, W. Jantsch, M. Helm, G. Brunthaler, W. Jost, H. Obloh, K. Köhler, and D. J. As, "Enhancement of the in-plane effective mass of electrons in modulation-doped in_xga_{1-x}as quantum wells due to confinement effects," *Phys. Rev. B*, vol. 48, no. 4, pp. 2328–2334, Jul. 1993.

[36] C. Sirtori, F. Capasso, J. Faist, and S. Scandolo, "Nonparabolicity and a sum rule associated with bound-to-bound and bound-to-continuum intersubband transitions in quantum wells," *Phys. Rev. B*, vol. 50, no. 12, pp. 8663–8674, Sep. 1994.

[37] D. F. Nelson, R. C. Miller, and D. A. Kleinman, "Band nonparabolicity effects in semiconductor quantum wells," *Physical Review B*, vol. 35, pp. 7770–7773, May 1987.

[38] A. Mátyás, S. Katz, S. Söntges, A. Vizbaras, P. Lugli, M.-C. Amann, and C. Jirauschek, "Coupled carrier-field monte-carlo analysis of mid-ir quantum cascade lasers," *Computational Electronics (IWCE), 2010 14th International Workshop on*, no. 12, pp. 1–4, Oct. 2010.

[39] T. Ando, A. B. Fowler, and F. Stern, "Electronic properties of two-dimensional systems," *Reviews of Modern Physics*, vol. 54, pp. 437–672, Apr. 1982.

[40] H. Sakaki, T. Noda, K. Hirakawa, M. Tanaka, and T. Matsusue, "Interface roughness scattering in GaAs/AlAs quantum wells," *Applied Physics Letters*, vol. 51, pp. 1934–1936, Dec. 1987.

[41] A. E. Asch and G. L. Hall, "Quantum Theory of the Residual Electrical Resistivity of Disordered Alloys," *Physical Review*, vol. 132, pp. 1047–1057, Nov. 1963.

[42] G. Bastard, *Wave mechanics applied to semiconductor heterostructures.* Les Editions de Physique, JOUVE, Paris, 1998.

[43] J. W. Harrison and J. R. Hauser, "Alloy scattering in ternary III-V compounds," *Physical Review B*, vol. 13, pp. 5347–5350, Jun. 1976.

[44] S. M. Goodnick and P. Lugli, "Effect of electron-electron scattering on nonequilibrium transport in quantum-well systems," *Physical Review B*, vol. 37, pp. 2578–2588, Feb. 1988.

[45] M. Moško, A. Mošková, and V. Cambel, "Carrier-carrier scattering in photoexcited intrinsic GaAs quantum wells and its effect on femtosecond plasma thermalization," *Physical Review B*, vol. 51, pp. 16 860–16 866, Jun. 1995.

[46] S. M. Goodnick and P. Lugli, "Effect of electron-electron scattering on nonequilibrium transport in quantum-well systems," *Phys. Rev. B*, vol. 37, no. 5, pp. 2578–2588, Feb. 1988.

[47] O. Bonno and J.-L. Thobel, "Monte Carlo modeling of carrier-carrier scattering in semiconductors with nonparabolic bands," *Journal of Applied Physics*, vol. 104, no. 5, p. 053719, Sep. 2008.

[48] S.-C. Lee and I. Galbraith, “Intersubband and intrasubband electronic scattering rates in semiconductor quantum wells,” *Physical Review B*, vol. 59, pp. 15 796–15 805, Jun. 1999.

[49] M. Mosko and A. Moskova, “Exchange carrier-carrier scattering of spin-polarized two-dimensional electron-hole plasma: Monte Carlo study,” *Semiconductor Science Technology*, vol. 9, pp. 478–481, May 1994.

[50] J. T. Lü and J. C. Cao, “Coulomb scattering in the Monte Carlo simulation of terahertz quantum-cascade lasers,” *Applied Physics Letters*, vol. 89, no. 21, p. 211115, Nov. 2006.

[51] M. Born and E. Wolf, *Electromagnetic theory of propagation, interference and diffraction of light.* Cambridge University Press, Cambridge, 1999.

[52] B. S. Williams, “Terahertz quantum cascade lasers,” Ph.D dissertation, Deptartment of Electrical Engineering and Computer Science, Massachusetts Institute of Technology, Cambridge, MA, 2003.

[53] R. Bräuer and O. Bryngdahl, “Design of antireflection gratings with approximate and rigorous methods,” *Optics Express*, vol. 33, pp. 7875–7882, Dec. 1994.

[54] B. S. Williams, S. Kumar, H. Callebaut, Q. Hu, and J. L. Reno, “3.4 THz quantum cascade laser operating above liquid nitrogen temperature,” *Electronics Letters*, vol. 39, no. 12, pp. 915–916, Jun. 2003.

[55] M. Razeghi, “High-performance InP-based mid-IR quantum cascade lasers,” *IEEE Journal of Selected Topics in Quantum Electronics*, vol. 15, no. 3, pp. 941–951, May 2009.

[56] A. Vizbaras, S. Katz, G. Boehm, and M.-C. Amann, “Short-injector quantum cascade laser emitting at 8-mum wavelength with high slope efficiency,” *IEEE Photonics Technology Letters*, vol. 21, pp. 1384–1386, Oct. 2009.

[57] S. Katz, Walter Schottky Institute, Technische Universität München, Germany (personal correspondence).

[58] A. Csurgay and K. Simonyi, *Az információtechnika fizikai alapjai.* BME Mérnöktovábbképző Intézet, 1997.

[59] J. H. Davies, *The physics of low dimensional semiconductors.* Cambridge University Press, 1998.

[60] G. Scalari, L. Ajili, J. Faist, H. Beere, E. Linfield, D. Ritchie, and G. Davies, “Far-infrared ($\lambda\tilde{}$=87 μm) bound-to-continuum quantum-cascade lasers operating up to 90 K,” *Applied Physics Letters*, vol. 82, p. 3165, May 2003.

[61] A. Leuliet, A. Vasanelli, A. Wade, G. Fedorov, D. Smirnov, G. Bastard, and C. Sirtori, “Electron scattering spectroscopy by a high magnetic field in quantum cascade lasers,” *Physical Review B*, vol. 73, no. 8, p. 085311, Feb. 2006.

[62] R. Nelander and A. Wacker, “Temperature dependence of the gain profile for terahertz quantum cascade lasers,” *Applied Physics Letters*, vol. 92, no. 8, p. 081102, Feb. 2008.

[63] C. Jirauschek and P. Lugli, “Limiting factors for high temperature operation of THz quantum cascade lasers,” *Physica Status Solidi C*, vol. 5, no. 1, pp. 221–224, 2008.

[64] X. Gao, D. Botez, and I. Knezevic, “X-valley leakage in GaAs-based midinfrared quantum cascade lasers: A Monte Carlo study,” *Journal of Applied Physics*, vol. 101, no. 6, p. 063101, Mar. 2007.

[65] M. A. Belkin, J. A. Fan, S. Hormoz, F. Capasso, S. P. Khanna, M. Lachab, A. G. Davies, and E. H. Linfield, “Terahertz quantum cascade lasers with copper metal-metal waveguides operating up to 178 K,” *Optics Express*, vol. 16, p. 3242, 2008.

[66] S. Kumar, Q. Hu, and J. L. Reno, “186 K operation of terahertz quantum-cascade lasers based on a diagonal design,” *Applied Physics Letters*, vol. 94, no. 13, p. 131105, Mar. 2009.

[67] T. Kubis and P. Vogl, “Self-consistent quantum transport theory: Applications and assessment of approximate models,” *Journal of Computational Electronics*, vol. 6, no. 1, pp. 183–186, Dec. 2006.

[68] T. Kubis, C. Yeh, and P. Vogl, “Quantum theory of transport and optical gain in quantum cascade lasers,” *Physica Status Solidi C*, vol. 5, no. 1, pp. 233–235, Oct. 2007.

[69] P. Harrison and R. A. Soref, “Population-inversion and gain estimates for a semiconductor TASER,” *IEEE Journal of Quantum Electronics*, vol. 37, pp. 153–158, 2001.

[70] A. Benz, G. Fasching, A. M. Andrews, M. Martl, K. Unterrainer, T. Roch, W. Schrenk, S. Golka, and G. Strasser, “Influence of doping on the performance of terahertz quantum-cascade lasers,” *Applied Physics Letters*, vol. 90, no. 10, p. 101107, Mar. 2007.

[71] B. S. Williams, H. Callebaut, S. Kumar, Q. Hu, and J. L. Reno, “3.4-THz quantum cascade laser based on longitudinal-optical-phonon scattering for depopulation,” *Applied Physics Letters*, vol. 82, p. 1015, Feb. 2003.

[72] S. Kumar, B. S. Williams, S. Kohen, Q. Hu, and J. L. Reno, “Continuous-wave operation of terahertz quantum-cascade lasers above liquid-nitrogen temperature,” *Applied Physics Letters*, vol. 84, p. 2494, Apr. 2004.

[73] T. Kubis, C. Yeh, and P. Vogl, “Non-equilibrium quantum transport theory: Current and gain in quantum cascade lasers,” *Journal of Computational Electronics*, vol. 7, pp. 432–435, Dec. 2007.

[74] B. S. Williams, S. Kumar, Q. Hu, and J. L. Reno, “Operation of terahertz quantum-cascade lasers at 164 K in pulsed mode and at 117 K in continuous-wave mode,” *Optics Express*, vol. 13, p. 3331, May 2005.

[75] H. Luo, S. R. Laframboise, Z. R. Wasilewski, G. C. Aers, H. C. Liu, and J. C. Cao, "Terahertz quantum-cascade lasers based on a three-well active module," *Applied Physics Letters*, vol. 90, no. 4, p. 041112, Jan. 2007.

[76] M. A. Belkin, Q. J. Wang, C. Pflügl, A. Belyanin, P. S. Khanna, A. G. Davies, E. H. Linfield, and F. Capasso, "High-temperature operation of terahertz quantum cascade laser sources," *IEEE Journal of Selected Topics in Quantum Electronics*, vol. 15, no. 3, pp. 952–967, 2009.

[77] D. E. Aspnes, R. Bhat, S. M. Kelso, and R. A. Logan, "Optical properties of Al(x)Ga(1-x)As," *Journal of Applied Physics*, vol. 60, pp. 754–767, Jul. 1986.

[78] B. S. Williams, "Terahertz quantum-cascade lasers," *Nature Photonics*, vol. 1, pp. 517–525, Sep. 2007.

[79] S. Katz, A. Vizbaras, G. Boehm, and M.-C. Amann, "High-performance injectorless quantum cascade lasers emitting below 6 μm," *Applied Physics Letters*, vol. 94, no. 15, p. 151106, Apr. 2009.

[80] I. Vurgaftman, J. R. Meyer, and L. R. Ram-Mohan, "Band parameters for III-V compound semiconductors and their alloys," *Journal of Applied Physics*, vol. 89, pp. 5815–5875, Jun. 2001.

[81] S. Tsujino, A. Borak, E. Müller, M. Scheinert, C. V. Falub, H. Sigg, D. Grützmacher, M. Giovannini, and J. Faist, "Interface-roughness-induced broadening of intersubband electroluminescence in p-SiGe and n-GaInAs/AlInAs quantum-cascade structures," *Applied Physics Letters*, vol. 86, no. 6, p. 062113, Feb. 2005.

[82] A. Wittmann, Y. Bonetti, J. Faist, E. Gini, and M. Giovannini, "Intersubband linewidths in quantum cascade laser designs," *Applied Physics Letters*, vol. 93, no. 14, p. 141103, Oct. 2008.

[83] J. R. Watling, A. B. Walker, J. J. Harris, and J. M. Roberts, "Monte Carlo simulation of electron transport in delta-doped lattice-matched and strained-balanced InGaAs/InAlAs quantum wells," *Semiconductor Science Technology*, vol. 14, pp. 12–22, Jan. 1999.

[84] A. M. Alcalde and G. Weber, "Electron-phonon relaxation rates in InGaAs-InP and HgCdTe-CdTe quantum wells," *Journal of Applied Physics*, vol. 85, pp. 7276–7281, May 1999.

[85] C. Y. Wang, L. Diehl, A. Gordon, C. Jirauschek, F. X. Kärtner, A. Belyanin, D. Bour, S. Corzine, G. Höfler, M. Troccoli, J. Faist, and F. Capasso, "Coherent instabilities in a semiconductor laser with fast gain recovery," *Physical Review A*, vol. 75, no. 3, p. 031802, Mar. 2007.

[86] L. Schrottke, M. Giehler, M. Wienold, R. Hey, and H. T. Grahn, "Compact model for the efficient simulation of the optical gain and transport properties in THz quantum-cascade lasers," *Semiconductor Science and Technology*, vol. 25, no. 4, p. 045025, Apr. 2010.

[87] R. Terazzi and J. Faist, “A density matrix model of transport and radiation in quantum cascade lasers,” *New Journal of Physics*, vol. 12, no. 3, p. 033045, Mar. 2010.

[88] G. Beji, Z. Ikonić, C. A. Evans, D. Indjin, and P. Harrison, “Coherent transport description of the dual-wavelength ambipolar terahertz quantum cascade laser,” *Journal of Applied Physics*, vol. 109, no. 1, p. 013111, Jan. 2011.

[89] C. Weber, F. Banit, S. Butscher, A. Knorr, and A. Wacker, “Theory of the ultrafast nonlinear response of terahertz quantum cascade laser structures,” *Applied Physics Letters*, vol. 89, no. 9, p. 091112, Aug. 2006.

[90] R. C. Iotti and F. Rossi, “Nature of charge transport in quantum-cascade lasers,” *Physical Review Letters*, vol. 87, no. 14, p. 146603, Sep. 2001.

[91] X. Gao, M. D’Souza, D. Botez, and I. Knezevic, “Design and simulation of deep-well GaAs-based quantum cascade lasers for 6.7 μm room-temperature operation,” *Journal of Applied Physics*, vol. 102, no. 11, p. 113107, Dec. 2007.

[92] X. Gao, D. Botez, and I. Knezevic, “Phonon confinement and electron transport in GaAs-based quantum cascade structures,” *Journal of Applied Physics*, vol. 103, no. 7, p. 073101, Apr. 2008.

[93] P. Borowik, J.-L. Thobel, and L. Adamowicz, “Monte Carlo based microscopic description of electron transport in GaAs/$\mathrm{Al_{0.45}Ga_{0.55}As}$ quantum-cascade laser structure,” *Journal of Applied Physics*, vol. 108, no. 7, p. 073106, Oct. 2010.

[94] R. Köhler, R. C. Iotti, A. Tredicucci, and F. Rossi, “Design and simulation of terahertz quantum cascade lasers,” *Applied Physics Letters*, vol. 79, pp. 3920–3922, Dec. 2001.

[95] H. Li, J. C. Cao, Y. J. Han, X. G. Guo, Z. Y. Tan, J. T. Lü, H. Luo, S. R. Laframboise, and H. C. Liu, “A study of terahertz quantum cascade lasers: Experiment versus simulation,” *Journal of Applied Physics*, vol. 104, no. 4, p. 043101, Aug. 2008.

[96] T. Unuma, M. Yoshita, T. Noda, H. Sakaki, and H. Akiyama, “Intersubband absorption linewidth in GaAs quantum wells due to scattering by interface roughness, phonons, alloy disorder, and impurities,” *Journal of Applied Physics*, vol. 93, pp. 1586–1597, Feb. 2003.

[97] P. Ramvall, N. Carlsson, P. Omling, L. Samuelson, W. Seifert, Q. Wang, K. Ishibashi, and Y. Aoyagi, “Quantum transport in high mobility modulation doped Ga0.25In0.75As/InP quantum wells,” *Journal of Applied Physics*, vol. 84, pp. 2112–2122, Aug. 1998.

[98] O. Drachenko, J. Galibert, J. Léotin, J. W. Tomm, M. P. Semtsiv, M. Ziegler, S. Dressler, U. Müller, and W. T. Masselink, “Electron-optical-phonon interaction in the $\mathrm{In_{0.73}Ga_{0.27}As}$-AlAs intersubband laser,” *Applied Physics Letters*, vol. 87, no. 7, p. 072104, Aug. 2005.

[99] M. Sugawara, N. Okazaki, T. Fujii, and S. Yamazaki, “Conduction-band and valence-band structures in strained $In_{1-x}Ga_xAs/InP$ quantum wells on (001) InP substrates,” *Physical Review B*, vol. 48, pp. 8102–8118, Sep. 1993.

[100] G. Hendorfer, M. Seto, H. Ruckser, W. Jantsch, M. Helm, G. Brunthaler, W. Jost, H. Obloh, K. Köhler, and D. J. As, “Enhancement of the in-plane effective mass of electrons in modulation-doped $In_xGa_{1-x}As$ quantum wells due to confinement effects,” *Physical Review B*, vol. 48, pp. 2328–2334, Jul. 1993.

[101] T. Kubis, C. Yeh, and P. Vogl, “Quantum theory of transport and optical gain in quantum cascade lasers,” *Physica Status Solidi C*, vol. 5, pp. 232–235, Jan. 2008.

[102] A. Vasanelli, A. Leuliet, C. Sirtori, A. Wade, G. Fedorov, D. Smirnov, G. Bastard, B. Vinter, M. Giovannini, and J. Faist, “Role of elastic scattering mechanisms in GaInAs/AlInAs quantum cascade lasers,” *Applied Physics Letters*, vol. 89, no. 17, p. 172120, Oct. 2006.

[103] C. Jirauschek, “Monte Carlo study of intrinsic linewidths in terahertz quantum cascade lasers,” *Optics Express*, vol. 18, no. 25, p. 25922, 2010.

[104] M. Yamanishi, T. Edamura, K. Fujita, N. Akikusa, and H. Kan, “Theory of the intrinsic linewidth of quantum-cascade lasers: Hidden reason for the narrow linewidth and line-broadening by thermal photons,” *IEEE Journal of Quantum Electronics*, vol. 44, pp. 12–29, Jan. 2008.

[105] A. Wacker, “Extraction-controlled quantum cascade lasers,” *Applied Physics Letters*, vol. 97, no. 8, p. 081105, Aug. 2010.

[106] M. Wienold, L. Schrottke, M. Giehler, R. Hey, and H. T. Grahn, “Nonlinear transport in quantum-cascade lasers: The role of electric-field domain formation for the laser characteristics,” *Journal of Applied Physics*, vol. 109, no. 7, p. 073112, Apr. 2011.

[107] M. S. Vitiello, T. Gresch, A. Lops, V. Spagnolo, G. Scamarcio, N. Hoyler, M. Giovannini, and J. Faist, “Influence of InAs, AlAs δ layers on the optical, electronic, and thermal characteristics of strain-compensated GaInAs/AlInAs quantum-cascade lasers,” *Applied Physics Letters*, vol. 91, no. 16, p. 161111, Oct. 2007.

[108] L. Allen and J. H. Eberly, *Optical resonance and two level atoms.* Wiley, New York, 1975.

[109] C. Weber, A. Wacker, and A. Knorr, “Density-matrix theory of the optical dynamics and transport in quantum cascade structures: The role of coherence,” *Physical Review B*, vol. 79, no. 16, p. 165322, 2009.

Publications

Journal papers

S. Fathololoumi, E. Dupont, C. W. I. Chan, Z. R. Wasilewski, S. R. Laframboise, D. Ban, A. Mátyás, C. Jirauschek, Q. Hu and H. C. Liu, *Terahertz quantum cascade lasers operating up to ∼200 K with optimized oscillator strength and improved injection tunneling*, Optics Express, (submitted).

A. Mátyás, P. Lugli, and C. Jirauschek, *Photon-induced carrier transport in high efficiency midinfrared quantum cascade lasers*, Journal of Applied Physics 110, 013108 (2011).

A. Mátyás, C. Jirauschek, F. Peretti, P. Lugli, and G. Csaba, *Linear circuit models for on-chip quantum electrodynamics*, IEEE Transactions on Microwave Theory and Techniques 59, 65-71 (2011).

A. Mátyás, M. A. Belkin, P. Lugli, and C. Jirauschek, *Temperature performance analysis of terahertz quantum cascade lasers: vertical versus diagonal designs*, Applied Physics Letters 96, 201110 (2010).

A. Mátyás, T. Kubis, P. Lugli, and C. Jirauschek, *Comparison between semiclassical and full quantum transport analysis of THz quantum cascade lasers*, Physica E 42, 2628–2631 (2010).

C. Jirauschek, A. Mátyás, and P. Lugli, *Modeling bound-to-continuum terahertz quantum cascade lasers: The role of Coulomb interactions*, Journal of Applied Physics 107, 013104 (2010).

G. Csaba, A. Mátyás, F. Peretti, and P. Lugli, *Circuit modelling of coupling between nanosystems and microwave coplanar waveguides*, International Journal of Circuit Theory and Applications 35, 315 – 324, (2007)

Conference proceedings

A. Mátyás, S. Katz, S. Söntges, A. Vizbaras, P. Lugli, M. C. Amann, and C. Jirauschek, *Coupled carrier-field Monte-Carlo analysis of mid-IR quantum cascade lasers*, IEEE Computational Electronics (IWCE), 14th International Workshop on, (2010).

C. Jirauschek and A. Mátyás, *Self-Consistent Analysis of Lasing Action in THz Quantum Cascade Lasers*, Nonlinear Photonics, OSA Technical Digest (CD) (Optical Society of America, 2010), paper NWB5

A. Mátyás, T. Kubis, P. Lugli, and C. Jirauschek, *Carrier transport in THz quantum cascade lasers: Are*

Green's functions necessary?, Journal of Physics: Conference Series 193, 012026 (2009).

C. Jirauschek, A. Mátyás, and P. Lugli, *Importance of Coulomb interactions in bound-to-continuum THz quantum cascade lasers*, Journal of Physics: Conference Series 193, 012062 (2009).

Talks and posters

A. Mátyás, P. Lugli, and C. Jirauschek, *Contribution of gain saturation to the current of high-power mid-infrared quantum cascade laser*, The 11th International Conference on Intersubband Transitions in Quantum Wells, Talk, 11-16 September 2011.

C. Jirauschek and A. Mátyás, *Intrinsic linewidth analysis for terahertz quantum cascade lasers*, The 11th International Conference on Intersubband Transitions in Quantum Wells, Talk, 11-16 September 2011.

A. Mátyás, P. Lugli, and C. Jirauschek, *Modeling of high-efficiency mid-infrared quantum cascade lasers*, Electron Dynamics In Semiconductors, Optoelectronics and Nanostructures (EDISON 17), Talk, 8-12 August 2011.

A. Mátyás, S. Katz, S. Söntges, A. Vizbaras, P. Lugli, M. C. Amann, and C. Jirauschek, *Coupled carrier-field Monte-Carlo analysis of mid-IR quantum cascade lasers*, 14*th* International Workshop on Computational Electronics (IWCE), Talk, Pisa, Italy, 26-19 October 2010.

C. Jirauschek and A. Mátyás, *Self-consistent analysis of lasing action in THz quantum cascade lasers*, OSA Advanced Photonics Congress – Nonlinear Photonics (NP 2010), Talk NWB5, Karlsruhe, Germany, June 21–24 2010.

A. Mátyás, C. Jirauschek, P. Lugli, and T. Kubis, *Carrier transport in THz quantum cascade lasers: Are Green's functions necessary?*, Electron Dynamics In Semiconductors, Optoelectronics and Nanostructures (EDISON 16), Talk Mo-D3, Montpellier, France, August 24–28 2009.

C. Jirauschek, A. Mátyás, and P. Lugli, *Importance of Coulomb interactions in bound-to-continuum THz quantum cascade lasers*, Electron Dynamics In Semiconductors, Optoelectronics and Nanostructures (EDISON 16), Poster Th-P30, Montpellier, France, August 24–28 2009.

A. Mátyás, C. Jirauschek, P. Lugli, and T. Kubis, *Comparison between semiclassical and quantum carrier transport,* International Conference on Modulated Semiconductor Structures (MSS-14), Poster Tu-mP36, Kobe, Japan, July 19–24 2009

Acknowledgment

First of all, I would like to thank my supervisor Dr. Christian Jirauschek, for his patience and for introducing me to the field of optoelectronics, carrier transport, and Monte-Carlo modeling of quantum cascade devices. It was only due to his professional guidance, friendly nature and his enthusiasm in research that I could complete my PhD work in a respectable way. I would also like to thank him for choosing me to work on the interesting topic of quantum cascade lasers and carrier transport. I consider his theoretical knowledge in the modeling of QCL devices tremendous. During PhD there were very few questions, related to my work that he could not answer, providing me enormous motivation and hints to pursue research in the correct direction.

I would also like to thank Prof. György Csaba for giving me useful advices in research and in life during his stay in Munich. He pointed me to the open possibility of modeling quantum cascade lasers as part of the Emmy Noether research group of my supervisor. I thank Prof. Csaba also for the fruitful discussions during my PhD about research topics, which are not part of this thesis, for example the interaction of microwave resonators and nanodevices. György Csaba was in Munich, during the first part of my PhD, and he is now a professor at the University of Notre Dame, Notre Dame, Indiana.

I am also grateful to my collaborators. First of all, Mikhail Belkin for sharing his knowledge on state of the art THz QCLs and their temperature performance. I consider the collaboration with Prof. Belkin a valuable personal experience from the design and experimental perspective. I also thank Dr. Tillmann Kubis for providing me with his NEGF simulation tool and for helping me in the understanding and classification of theoretical transport models. Furthermore, I thank Dr. Simeon Katz for his experimental feedback on InGaAs-based mid-infrared QCLs.

I have performed my PhD work as a part of the Emmy Noether research group, which was hosted by the Institute for Nanoelectronics at the TU-Munich. First of all I gratefully acknowledge the help from Prof. Paolo Lugli on improving the structure and quality of my publications and in pointing me to the relevant conferences of my topic. I am grateful to all the members of the Nanoelectronics chair for providing me with friendly support and a pleasant atmosphere. I thank all my colleagues, especially Simone Locci, Mario Arcari, Federico Peretti, Gunther Jegert and Xueming Ju for the fun that we had at work, organized events, retreats, conferences and outside work. I also greet my office-mates, Dan and Bogdan Popescu and Sebastian Todor, and all the people from the theory department. Simone Locci,

Sebastian Todor and Alaa Abdellah deserve special thanks for proof-reading the thesis.

Finally, I want to thank my brother, Mátyás Beniamin for his support and cheers from the beginning, and my parents Mátyás Mária and Mátyás Beniamin, for helping me towards the decision of starting a PhD at the TU-Munich. I also feel thankful for the loving support of Küsmődi Csilla, which also motivated me a lot during my PhD.

Curriculum Vitae

Alpár István Mátyás

Persönliche Daten

Geburtsdatum:	18.12.1983	
Geburtsort:	Aiud (Strassburg am Mieresch) Rumänien	
Adresse:	*privat:*	*beruflich:*
	Blütenstr. 20, App. 40	Lehrstuhl für Nanoelektronik
	80799 München	Technische Universität München
	+49 1577 5354470	Arcistr. 21
	+40 745 580222	Tel. +49 89 28925331,
		alparmat@mytum.de,
		alparmat@gmail.com
Familienstand:	ledig	
Staatsangehörigkeit:	Ungarn, Rumänien	
Eltern:	Beniamin Mátyás, Mária Mátyás, geb. Kvacskay	

Schulischer Werdegang

1990-2002:	Colegiul National „Bethlen Gabor“ Aiud, Rumänien (Gesamtschule Gymnasialer Zweig)
06/2002:	Bacalaureat (Abitur), Durchschnittsnote 9.25 von 10

Studium

09/2002-06/2007:	Master of Sciences in Electronic and Computer Engineering an der Universität Pázmány Péter (Budapest)
06/2003:	Szigorlat (1. Zwischenprüfung) (Note, 4 von 5)
01/2005:	Szigorlat (2. Zwischenprüfung) (Note, 5 von 5)
01/2007:	Szigorlat (3. Zwischenprüfung) (Note, 4 von 5)
06/2007:	Államvizsga (Diplomprüfung) (Note 5 von 5)

Promotion

seit 07/2007:	Wissenschaftlicher Angestellter am Lehrstuhl für Nanoelektronik, Technische Universität München

Praktika und hilfswissenschaftliche Tätigkeiten

03/2006 – 08/2006:	Erasmusstudent an der TU München
02/2007 – 06/2007:	Gaststudent an der TU München

Auszeichnungen und Stipendien

2002 – 2007:	Stipendium von Pázmány Péter Katolikus Egyetem, Informaciós Technológiai Kar (Stipendium für sehr gute Studienleistungen)
2005 – 2007:	Tóth Isaszegi Irén (Pázmány Alapítvány) ösztondíj (Universitäts-Stipendium für den jeweils besten Studenten einer Fakultät)